



UNIVERSITY OF  
BIRMINGHAM

# Microwave Power Detectors

---

A thesis submitted to the University of Birmingham for the  
degree of MSc by Research

Shiva Eghbal Behbahani

**School of Electronic, Electrical and Systems Engineering**

**University of Birmingham**

**June 2015**

UNIVERSITY OF  
BIRMINGHAM

**University of Birmingham Research Archive**

**e-theses repository**

This unpublished thesis/dissertation is copyright of the author and/or third parties. The intellectual property rights of the author or third parties in respect of this work are as defined by The Copyright Designs and Patents Act 1988 or as modified by any successor legislation.

Any use made of information contained in this thesis/dissertation must be in accordance with that legislation and must be properly acknowledged. Further distribution or reproduction in any format is prohibited without the permission of the copyright holder.

## **Abstract**

The basic quantities of current and voltage are difficult to measure directly at microwave frequencies; therefore power becomes a crucial parameter. Design, operation and purchase of any RF or microwave equipment and measurement of microwave signals are enhanced by knowledge of the power [1]. So it is important to have accurate power-measuring standards at all frequencies. There are many potential applications being developed at millimetre-wave and sub millimetre wave frequencies. The need for a power measurement unit and associated standards at these high frequencies is the motivation for this research project.

This thesis looks at the design of a waveguide bolometer that is suitable for a power detector. The bolometric method measures microwave power by converting it into heat. It measures power by using a resistance changing heat sensitive element and usually a bridge circuit to read out accurate resistance change, due to the absorbed power. In order to investigate the theory, the heat sensing element is initially modelled here as an inductive metal post located at a specific position in a rectangular waveguide. The parameters are determined by using analytical equations and transmission line theory. Full wave electromagnetic simulation software is used to design a structure accurately based on the theory. The results are compared with those derived from calculations. A thin film heat sensing element in a rectangular waveguide is also considered and a sensor element is designed. The results of simulation for the thin film design validate the theory and show good power absorption at the centre frequency of operation. The ultimate aim is to have a bolometer operating at the higher frequency bands in WR3 and WR6 waveguides, made using micro machining technology; however, in this thesis they are modelled at X-band (8.2-12.4 GHz).

## **Acknowledgements**

I wish to express my sincere thanks to my supervisor Professor Mike J. Lancaster for his continuous support, academic advice and his patient teaching during my MSc by Research project at the University of Birmingham. Without his support and assistance I wouldn't have been able to carry out this project. I would like to thank my academic advisor Dr Paul Smith for his constructive comments on my reports.

I would like to thank my colleagues and friends at the Electronic, Electrical and Systems Engineering School and at the Emerging Device Technology group for their friendship and help throughout this time, especially Mr Yasin Kabiri Isfahani, Dr Xiaobang Shang and Mr Farzad Hayati.

I appreciate the financial support from the University of Birmingham by giving me the Electronic, Electrical and Systems Engineering School scholarship.

Many thanks also to Janet's Proofreading Service for copy editing this thesis for conventions of language, spelling and grammar.

Last but definitely not least, I would like to deeply thank my parents and sister for their understanding, encouragement and unconditional support throughout my work at the University of Birmingham.

## **List of Abbreviations**

**RF-** Radio Frequency

**DC-** Direct Current

**TE-** Transverse Electric

**TM-** Transverse Magnetic

**TEM-** Transverse Electromagnetic

**VSWR-** Voltage Standing Wave Ratio

**RL-** Return Loss

**BW-** Bandwidth

**FBW-** Fractional Bandwidth

# Table of Contents

Abstract.....	1
Acknowledgements.....	2
List of Abbreviations .....	3
List of Figures.....	8
List of Tables .....	14
CHAPTER 1- INTRODUCTION.....	15
1-1 Introduction to power detection .....	15
1-2 Bolometric approach.....	17
1-2-1 Efficiency .....	19
1-2-2 Sensitivity.....	20
1-3 Objectives of the project .....	21
1-3-1 Description of the thesis' structure.....	23
CHAPTER 2- BOLOMETER POWER DETECTION .....	25
2-1 Principles of bolometers .....	25
2-1-1 Wheatstone bridge:.....	26
2-1-2 Bolometer element circuit .....	28
2-2 Bolometer literature review .....	30
CHAPTER 3 -THEORETICAL FOUNDATIONS .....	38
3-1 Transmission lines .....	38
3-1-1 Lossless line .....	39
3-2 Reflection coefficient .....	40

3-2-1 Standing waves.....	41
3-2-2 S-parameters.....	42
3-3 Input impedance .....	43
3-4 Skin depth.....	45
3-5 Waveguides .....	45
3-5-1 Modes.....	46
3-5-2 Rectangular waveguides.....	47
3-5-3 Cut-off frequency .....	49
3-6 X-band waveguide characteristics .....	51
3-7 Short circuit termination.....	52
3-8 Comparing X-band waveguide, WR6 and WR3 for TE <sub>10</sub> .....	54
CHAPTER 4- IMPLEMENTING A NON REFLECTIVE POST IN A WAVEGUIDE.....	56
4-1 Introduction .....	56
4-2 Matching.....	56
4-2-1 Waveguide with short circuit termination and inductive and resistive element.....	57
4-3 Resistance of a post in waveguide.....	67
4-3-1 Comparing <i>R<sub>Basic</sub></i> and <i>R<sub>High</sub></i> (Equations (4-18) and (4-24)).....	74
4-3-2 Comparing <i>R<sub>Basic</sub></i> and <i>R<sub>low</sub></i> (Equations (4-18) and (4-25)) .....	75
4-3-3 Resistance versus $r/\delta$ .....	77
4-4 Reactance of a post in waveguide.....	80
4-5 Impedance of the post in waveguide .....	84
CHAPTER 5- THIN FILM BOLOMETER.....	89

5-1 Thin film bolometer.....	89
5-1-1 First case.....	93
5-1-2 Second case .....	98
5-2 Platinum film bolometer.....	103
CHAPTER 6 – CONCLUSION AND FUTURE WORK .....	111
6-1 Limitations.....	112
6-2 Future work.....	112
References.....	114
APPENDIX 1.....	119
A1- Introduction.....	119
A2- CST Designs .....	121
A2-1 Basic OMT design without filtering .....	121
A2-2 Determination and Improvement .....	126
A2-3 Isolation .....	128
A3- Filter design .....	129
A3-1 Quality Factor .....	131
A3-2 Coupling coefficient .....	132
A3-3 Direct coupled cavity filter response .....	134
A4- Filter based Orthomode Transducer .....	136
A4-1 Initial Response .....	138
A4-2 Optimisation .....	140
A-4-3 Isolation.....	147

A-4-4 Conclusion..... 148

## List of Figures

Figure 2-1 Wheatstone bridge- taken from [26] .....	26
Figure 2-2 Wheatstone bridge circuit used with thermistor mount- taken from [26] .....	27
Figure 2-3 Side view and front view of metal film with width $D$ and distance $L$ from the waveguide short circuit - taken from [29] .....	28
Figure 2-4 Equivalent circuit of the thin film in short circuited waveguide taken from [33] .....	29
Figure 2-5 Equivalent circuit of bolometer element consisting of thin film, electrode and substrate- taken from [32]. .....	31
Figure 2-6 Frequency characterization of 35 GHz thin film bolometer unit- taken from [32]. .....	32
Figure 2-8 Matched thin film bolometer- taken from [21]. .....	33
Figure 2-7 Thin-film bolometer inside a waveguide and its electrical equivalent circuit-taken from [21]. .....	33
Figure 2-9 Bolometer reflection coefficient in its working frequency band- taken from [21]. .....	35
Figure 2-10 Barretter mount structure- taken from [25] .....	36
Figure 2-11 VSWR versus operation frequency for the designed barretter mount- taken from [25] ...	36
Figure 3-1 transmission line model with voltage generator $V_g$ , characteristic impedance $Z_0$ and load impedance $Z_L$ .....	40
Figure 3-2 transmission line model with characteristic impedance $Z_0$ and load impedance $Z_L$ . .....	43
Figure 3-3 Electric field patterns for TE <sub>10</sub> ,TE <sub>20</sub> and TE <sub>30</sub> - taken from [39] .....	47
Figure 3-4 Electric field and magnetic field for mode TE <sub>10</sub> - taken from [44].....	48
Figure 3-6 Side view of rectangular waveguide with short circuit termination.....	52
Figure 3-5 Rectangular waveguide .....	52
Table 3-1 characteristics of different waveguides .....	55
Figure 4-1 Waveguide with obstacle .....	57
Figure 4-2 Equivalent circuit of a waveguide with short circuit termination and resistive, reactive element.....	58
Figure 4-3 Side view of waveguide with short circuit termination and resistive, inductive element. ...	59

Figure 4-4 Reflection coefficient of resistive and inductive element vs length to back short, $\lambda g = 40$ mm.....	61
Figure 4-5 Length to short circuit termination versus R, using Equations (4-12); $Z_0 = 444.08 \Omega$ , $\beta = 158.04$ and $\lambda g = 40$ mm.....	63
Figure 4-6 Length to short circuit termination versus reactance, using Equations (4-14); $Z_0 = 444.08 \Omega$ and $\lambda g = 40$ mm.....	64
Figure 4-7 S11 versus frequency for different R and X.....	65
Figure 4-8 Resistance versus corresponding S11 bandwidth at -20 dB.....	66
Figure 4-9 Cross-section of the post with skin depth $\delta$ and radius $r$ .....	68
Figure 4-10- Figure of $I/I_0$ versus penetration depth $r$ at $f = 10$ GHz.....	69
Figure 4-11 Resistance Equation (4-18) versus radius of the post.....	70
Figure 4-12 Resistance of post versus post radius, Equation (4-24), $f = 10$ GHz and $\sigma = 9.52 \times 10^6 \text{ Sm}^{-1}$ .....	72
Figure 4-13 Resistance versus post radius- Equation (4-25), $f = 10$ GHz and $\sigma = 9.52 \times 10^6 \text{ Sm}^{-1}$ .....	73
Figure 4-14 comparing different resistance equations, graph of resistance versus platinum ( $\sigma = 9.52 \times 10^6 \text{ Sm}^{-1}$ ) post radius at $f = 10$ GHz, Equation (4-18),(4-21),(4-24),(4-25). .....	73
Figure 4-15 Resistance versus frequency for a platinum post with radius = $20 \mu\text{m}$ , Equations (4-18),(4-21), (4-24) and (4-25).....	76
Figure 4-16 Resistance equations divided by Equation (4-17) versus $r\delta$ .....	79
Figure 4-17 Post reactance Equation (4-32) versus post radius, X band waveguide; $a = 22.86$ mm, $b = 10.16$ mm, $\lambda g = 40$ mm and $Z_0 = 444.08 \Omega$ .....	81
Figure 4-18 Normalized reactance equations versus radius of the post at $f = 10$ GHz, X band waveguide; $a = 22.86$ mm, $b = 10.16$ mm, $\lambda g = 40$ mm and $Z_0 = 444.08 \Omega$ .....	83
Figure 4-19 The WR90 waveguide structure with inductive post – designed in CST microwave Studio by student.....	84

Figure 4-20 graph of S11 versus frequency for X band waveguide; $a = 22.86$ mm, $b = 10.16$ mm, $\lambda g = 40$ mm and $Z_0 = 444.08 \Omega$ with post with $r = 0.581$ mm and $\sigma = 33.41$ S/m located at $l = 7.4$ mm to the termination produced by CST Microwave Studio .....	86
Figure 4-21 optimized S11 versus frequency for X band waveguide; $a = 22.86$ mm, $b = 10.16$ mm, $\lambda g = 40$ mm and $Z_0 = 444.08 \Omega$ with a post with a radius $r = 0.581$ mm and $\sigma = 33.41$ S/m located at $l = 8$ mm to the termination .....	87
Figure 4-22 Power flow in X band waveguide; $a = 22.86$ mm, $b = 10.16$ mm, $\lambda g = 40$ mm and $Z_0 = 444.08 \Omega$ with a post with radius $r = 0.581$ mm and $\sigma = 33.41$ S/m located at $l = 8$ mm to the termination. ....	88
Figure 5-1 (a) The rectangular waveguide with thin film located at distance $l$ to termination, (b) The thin film structure consisting of the thinner metal film on thicker glass substrate. ....	90
Table 5-1 Parameters of design for thin nichrome film on glass substrate to operate at $f = 8.55$ GHz in X-band waveguide .....	95
Figure 5-2 VSWR versus frequency for X band waveguide with nichrome film on the glass substrate- design parameters are given in Table (5-1).....	95
Figure 5-3 The WR90 waveguide structure with inductive thin film – Designed in CST MICROWAVE STUDIO.....	96
Figure 5-4 S11 versus frequency for X band waveguide with nichrome film on the glass substrate- design parameters are given in Table (5-1).....	96
Figure 5-5 VSWR versus frequency for X band waveguide with nichrome film on the glass substrate- design parameters are given in Table (5-1).....	97
Figure 5-6 VSWR versus frequency taken from [29] .....	98
Table 5-2 Parameters of design for thin nichrome film on glass substrate to operate at $f = 9.26$ GHz in X-band waveguide .....	99
Figure 5-7 VSWR versus frequency for X band waveguide with nichrome film on the glass substrate- design parameters are given in Table (5-2).....	100

Figure 5-8 S11 versus frequency for X band waveguide with nichrome film on the glass substrate- design parameters are given in Table (5-2).....	101
Figure 5-9 VSWR versus frequency for X band waveguide with nichrome film on the glass substrate- design parameters are given in Table (5-2).....	102
Figure 5-1 VSWR versus frequency taken from [29].....	102
Figure 5-11 Reflection coefficient of resistive and inductive element versus length to back- short, $R = 444.08 \Omega$ , $X = 0.61 \Omega$ , $\lambda g = 40 \text{ mm}$ .....	104
Figure 5-12 Normalized reactance Equation (5-12) versus film width.....	105
Table 5-3 Parameters of design for thin platinum film on glass substrate to operate at $f = 10 \text{ GHz}$ in X- band waveguide .....	106
Figure 5-13 VSWR versus frequency for X band waveguide with platinum film on the glass substrate- design parameters are given in Table (5-3).....	106
Figure 5-14 S11 versus frequency for X band waveguide with platinum film on the glass substrate- design parameters are given in Table (5-3).....	107
Figure 5-15 Optimized S11 versus frequency for X band waveguide with platinum film on the glass substrate- initial design parameters are given in Table (5-3).....	108
Figure 5-16 VSWR versus frequency of the optimized response, Figure (5-15), for X band waveguide with platinum film on the glass substrate.....	109
Figure A1 Simple OMT-taken from [56].....	120
Table A1 Parameters and their values for the OMT design.....	122
Figure A2 OMT design structure indicating mode $TE_{10}$ at port one. The structure is designed in CST software.....	123
Figure A3 $S_{31}$ graph of the designed OMT for mode $TE_{10}$ - Generated in CST software by the student .....	124
Figure A4 $S_{21}$ graph of the designed OMT for mode $TE_{10}$ - Generated in CST software by the student .....	124
Figure A5 $S_{21}$ graph of the designed OMT for mode $TE_{01}$ - Generated in CST software by the student .....	125

Figure A6 $S_{31}$ graph of the designed OMT for mode $TE_{01}$ - Generated in CST software by the student .....	126
Figure A7 Improved $S_{21}$ response to mode $TE_{01}$ in the second OMT design- generated by student in CST software .....	127
Figure A8 isolation between waveguide arms in the OMT design- generated in CST software by student.....	128
Figure A9 The block diagram of the third order resonator filter to be designed- drawn by the student .....	129
Figure A10 Structure of third order direct coupled cavity filter- Designed by student in CST.....	130
Figure A11 Initial response of designed filter including $S_{11}$ and $S_{21}$ graphs-generated by student using CST .....	134
Table A5 Parameters and their values for the 3 <sup>rd</sup> order filter design. ....	135
Figure A12 Optimized response of designed filter, including $S_{11}$ and $S_{21}$ graphs- generated by student in CST .....	135
Figure A13 Structure of filter based OMT- Designed by student in CST .....	136
Figure A14 Initial response of port 3 of filter based OMT to mode $TE_{10}$ , including $S_{11}$ and $S_{31}$ - generated by student in CST .....	138
Figure A15 Initial response of port 2 of filter based OMT to mode $TE_{01}$ , including $S_{11}$ and $S_{21}$ graphs- generated by student in CST .....	139
Table A6 Parameters and their values found for the optimized design. ....	141
Figure A16 $S_{11}$ graph for mode 1 which is $TE_{10}$ mode. ....	142
Figure A17 $S_{11}$ graph for mode 2 which is $TE_{01}$ mode.....	143
Figure A18 $S_{21}$ graph for mode 2 of square waveguide ( $TE_{01}$ ) which is the only mode of waveguide with port 2.....	144
Figure A19 $S_{22}$ graph for waveguide with port 2.....	145
Figure A20 $S_{31}$ graph for mode 1 of square waveguide ( $TE_{10}$ ) which is the only mode of waveguide with port 3.....	146
Figure A21 $S_{33}$ graph for waveguide with port 3.....	147

Figure A22  $S_{32}$  response which shows high port isolation between two waveguide arms of filter based OMT- generated by student in CST ..... 148

## List of Tables

Table 5-1 Parameters of design for thin nichrome film on glass substrate to operate at $f = 8.55$ GHz in X-band waveguide .....	95
Table 5-2 Parameters of design for thin nichrome film on glass substrate to operate at $f = 9.26$ GHz in X-band waveguide .....	99
Table 5-3 Parameters of design for thin platinum film on glass substrate to operate at $f = 10$ GHz in X-band waveguide .....	106
Table A5 Parameters and their values for the 3 <sup>rd</sup> order filter design. ....	135
Table A6 Parameters and their values found for the optimized design. ....	141

# CHAPTER 1- INTRODUCTION

## 1-1 Introduction to power detection

At microwave frequencies, above a few tens of GHz the basic quantities of current and voltage are difficult to measure directly; therefore power has become a crucial parameter in this region of the radio-frequency spectrum. Design, operation and purchase of any RF or microwave equipment is enhanced by measurements and knowledge of power [1].

In microwave applications there is always transmission and reception of signals [2]; therefore the signal power level is important, since the components within the microwave equipment are designed to receive a specific amount of power and pass it to the subsequent component. Lack of knowledge about power affects these components and consequently the overall performance of devices and systems. Power can also affect the price of a microwave device. For instance, a transmitter with more output power is generally more complex and therefore it will be more expensive [3].

Many of the measurements in microwave circuits are carried out at powers up to several watts; therefore it is important to have accurate power-measuring standards at all frequencies in the millimetre and sub-millimetre wave range [4]. Some work has already been carried out with this aim in view; for example, the vibration wattmeter by Cullen and French [5], but a simple method suitable for general use is still an important requirement [6]. Developments in semiconductor technology and thin film techniques have greatly affected the evolution of commercial power detectors [7].

The power measurement device should be designed in a way that can be connected to the device under test directly. It should remain matched to the transmission line at all the frequencies of operation. Ideally the power meter is matched without use of any impedance transformers or other adjustments [2]. Power sensors can have problems such as poor sensitivity, slow response time, poor impedance match and calibration. Usually all of these problems are worse as the frequency increases. Currently there are some convincing commercial sensors available for frequencies up to 110 GHz, but for higher frequencies there are no fully satisfactory measurement options [4].

This thesis is concerned with waveguide power detectors. Various methods for waveguide power measurement were developed in the 1930s; they have changed a little over the years and are still in common use today. The choice of the power sensing method depends on the type of signal to be measured and the particular application [8]. There are a variety of power meters in existence of different forms and complexities [9]. Some of the existing instruments for microwave power measurement are calorimeters, diode detectors, thermocouples and bolometers [3]. Each of these instruments is suitable to measure a specific range of signal levels; for instance water calorimeters and bolometers can be used for measuring high powers and low powers respectively [10]. Calorimeters and bolometers are methods that have high accuracy but are complicated and thus complex for general use [2]. Therefore, the instrument's limitations and the pros and cons of each instrument, compared to its alternatives, should also be taken into consideration when choosing the right instrument for a specific purpose.

There are many areas where millimetre and submillimetre wave technology is applied; this includes astronomy, medical diagnosis, satellite communications and imaging. All these areas require valid knowledge of power in order to be able to function and progress and they could benefit from an accurate linear power meter [11] [12].

## **1-2 Bolometric approach**

A suitable approach in measuring microwave power is to use methods that are based on converting microwave power into heat. Such power measurement methods are bolometric and calorimetric; they are also the most common and convenient ways for determining microwave power [13] [2]. Bolometers are used to measure low and medium microwave power ranges [14]. In this work, the power level below  $10^{-2}$  watt will be referred to as low power; the range between  $10^{-2}$  and 10 watts will be called medium power and above 10 watts is high power [2].

A bolometer is a radiation power detector whose input is electromagnetic radiation. The radiated power is converted to heat when incident on the resistive bolometer element [15]. Resistance is temperature dependent and its value increases if it has positive temperature coefficient of resistance and decreases if it has negative temperature coefficient of resistance. The temperature coefficient of resistance depends on the material and is determined by how the resistivity of material changes with the changes in temperature [16]. By measuring the subsequent change of electrical resistance due to the change in temperature, the power can be deduced [15] [2]. Bolometer consists of three essential functions: (i) initially coupling the energy of the electromagnetic wave of appropriate frequency from the waveguide; (ii) a

sensitive resistance element (bolometer element) which can sense the power as it is absorbed [17] and (iii) a mechanism to read out the absorbed power. The incident RF or microwave power is dissipated in the bolometer element and causes the element to heat up [15]. This leads to a rise in the temperature and correspondingly changes the electrical resistance of the element.

The bolometer element can have a negative temperature coefficient of resistance or a positive temperature coefficient of resistance [10]. Different types of bolometer elements exist: barretter, thermistor, lamp and film bolometers. All are temperature sensors that absorb the incoming power and their resistance changes when heated [2] [7]. Different mechanisms can be used to read out the resistance change due to the absorbed power, such as bridge circuits.

One way is using a Wheatstone bridge to measure the resistance of the element. A Wheatstone bridge is an electrical circuit for measuring electrical resistances or small changes of resistance [18]. When the element warms up due to the microwave power dissipation, the bridge becomes unbalanced and this can be brought back to balance by reducing the direct current flowing through the element. The power represented by this change in direct current is used to determine the microwave power [19] [13]. Wheatstone bridge is explained in more detail in Chapter 2.

Bolometers are not new [7], Herschel found infrared radiation by using a bolometer in 1800 [20]. However more recently in the 1940s bolometers were developed for power

measurements at frequencies above 1 GHz [7]. Bolometers are generally only found in precision metrology laboratories and are not generally in use among RF engineers [9].

The validity of a power measurement device can be reliably checked by comparing the power readings of similar meters. For bolometers, power readings of different types such as thermistors and barretters can be compared to each other. An agreement between the readings shows the operation of both devices. Usually for low frequencies good agreement is achieved; whereas for the higher frequencies, errors are larger [2].

Brunetti [21] has written the law behind the behaviour of a bolometer with single relationship

$$R = R(P, T) = \text{constant} \quad (1-1)$$

Where  $R$  is the dynamic resistance of the sensitive element;  $P$  the total power dissipated in it and  $T$  its absolute temperature. This shows that for a bolometer the resistance value is dependent on the dissipated power and temperature and the law of operation. If  $R$  is kept constant a relationship between temperature and power is defined from which the rate of change of resistance with respect to power can be found [22]. For a bolometer to be reliable and meet the standards, its sensitivity, reflection coefficient and effective efficiency must be considered [21].

### **1-2-1 Efficiency**

According to Lane “The term efficiency is widely used to describe the performance of a bolometer.” [23]. Ideally the sensor in the power detector should absorb all the power that is incident upon it, but in reality it almost never happens because of impedance mismatch

between the sensor and transmission line where the power reflects back. Additionally, the power may be dissipated in other places such as the conductors, components or sidewalls of waveguide, rather than only in the sensing element. Only the power that is dissipated in the power sensor is metered. This effect relates to effective efficiency  $\eta_e$ . It can have values between 0 to 1 (100%), where one is the maximum and represents the ideal case.

The effective efficiency for a bolometer element can be determined by the low frequency power equivalent to the change in bias power to bring the resistance back to its initial value before the application of the RF power, over the net power that is absorbed by the sensing element. The value of  $\eta_e$  changes with the frequency, but not so much with the power levels [24]. As the frequency increases and the wavelength becomes shorter, the terms of performance such as effective efficiency, sensitivity and a wideband matching are more difficult to attain. In addition to the complexities of operating with small elements at higher frequencies, since the skin depth is also reduced as the frequency is increased therefore the losses in the waveguide walls increase [25].

### **1-2-2 Sensitivity**

Sensitivity measures the ability of a component to detect signals. To understand the specified sensitivity of a component the test conditions should be specified [26]. The sensitivity of the power sensing element depends on the material of the resistor and its structure, such as thickness or size and shape. For thin films, it is preferable to use material with a high resistance temperature coefficient and stability [25]. The sensitivity is determined by the

change in the resistance value over the change of power and according to Brunetti [21] it can be written as:

$$S = \alpha ZR \quad (1-2)$$

Where  $Z \left(\frac{\text{Kelvin}}{\text{Watt}}\right)$  is the thermal impedance of the bolometer's sensitive element referred to the environment;  $R$  is the ohmic resistance at  $T = 273$  K and  $\alpha \left(\frac{1}{\text{Kelvin}}\right)$  is the temperature coefficient of the same resistance. It is notable that in order to increase the bolometer's sensitivity these parameters should be altered accordingly and they are dependent on the material of the sensitive element [21].

### **1-3 Objectives of the project**

Different applications are currently hampered because of the lack of accurate, linear and repeatable measurement equipment at mm-wave frequencies, especially lacking are standards above about 75 GHz. The available alternative now is the sensitive diode power detectors which are non-linear and non-repeatable. The need for such a power measurement unit is the reason behind this research [27].

The proposed project is to design a linear, full waveguide bandwidth microwave power detector for millimetre waves. The power detector considered for this project is a linear bolometer with a resistance changing heat sensitive bolometer element. Although the ultimate aim is to achieve a mm-wave bolometer, here we will model it at X band (8.2-12.4 GHz). The advantages of this detector are its linearity and having a sufficiently large dynamic range that makes it an excellent power sensor. The challenges lie in the detailed microwave design and

the accurate measurements required for determining full characteristics [9] [27]. Two heat sensing elements will be modelled in this thesis: an inductive metal post and a thin resistive film. Initially an inductive metal post is considered as the bolometer element; to confirm the bolometer and transmission line theory in Chapters 2 and 3. The calculations are more easily made with the post structure, as it is simpler and has fewer parameters to be adjusted, compared with the thin film. Analytical equations are also available for the post. Once the theory is confirmed with the post, the work moves on to the thin resistive film.

In Chapter 3 the necessary parameters for matching the proposed configurations are determined by using the analytical equations. Afterwards, the MICROWAVE STUDIO module of the 3D electromagnetics simulation software, CST STUDIO [28] is used to design a structure using these parameters which are determined based on the theory. Then this design is simulated and the results are generated and compared with the results derived from the calculations. The aim is to find that both sets of results are matched to verify the theory.

The objective is to develop linear, traceable power sensors for WR90, but then the proven theory can be used to design power detectors in smaller waveguides WR3 and WR6 at the higher frequency bands. These waveguide power detectors can be made using micro machining technology [27].

### **1-3-1 Description of the thesis' structure**

In Chapter 2, an extensive background survey has been carried out around the principles of power detectors and methods of power detection, in order to understand the concepts of power detection and the available methods. The principles of a bolometer's performance are studied and understood. Some literature about the progress of research into the design and use of bolometers since their foundation has been reviewed, along with literature about different types of bolometer. In Chapter 3, the fundamental concepts and parameters of transmission line theory are studied, followed by investigating transmission line impedance matching relevant to the bolometer design.

Initially the focus is to design a bolometer with a metal post being used as the sensitive element. Chapter 4 discusses the analytical equations and calculations to derive fitting parameters for the post configuration that provides the matched circuit. To do so knowledge from the literature is used. Based on the derived parameters, the model for the waveguide bolometer with the post is simulated and the results are compared.

In Chapter 5, the proven method is used to investigate the situation, but the sensitive element is replaced with thin film. Afterwards the mathematical calculations are made for the thin metal film. Then the model is simulated for a bolometer with thin film with the calculated dimensions. The waveguide with the power-sensing element is the main deliverable factor for this project. Finally some possible ways for further improvements are suggested for future work.

In Appendix 1, an orthomode transducer is discussed; which can be seen as a completely different project to the power sensor. It is included as an appendix as there was work done during the MSc by research in this area.

## CHAPTER 2- BOLOMETER POWER DETECTION

This chapter explains in more detail about the principles of the structure and use of bolometers. Also it looks into some different work that has been carried out in this field to advance power detection using resistive thin film technology.

### 2-1 Principles of bolometers

A suitable approach in measuring microwave power is to use methods that are based on converting wave power into heat. Such power measurement methods are used in bolometers and calorimeters [1]. Bolometers are used to measure low and medium microwave power [1] [14]. A bolometer is a radiation power detector whose output is an electrical signal dependent on microwave power [15]. It mainly consists of a sensitive resistance element (bolometer element) which can sense the power. Usually, the electromagnetic wave of appropriate frequency is radiated into the waveguide and is incident on the bolometer element [6] [17]. The incident power is dissipated in this element and causes the element to heat up; this leads to a change in the temperature, which correspondingly changes the electrical resistance of this element. This element can be either a thermistor or barretter. Traditionally these terms refer to a thermistor being a bead of semiconductor material mounted between two fine wires, it usually has a negative temperature coefficient of resistance and the barretter being a wire or thin film of material, deposited on glass sheet and it usually has a positive temperature coefficient of resistance [10]. The change in the resistance of the element in the bolometer is used for power measurement through different approaches such as Wheatstone bridge.

### 2-1-1 Wheatstone bridge:

The Wheatstone bridge has been in use since 1843 and is shown in Figure (2-1). It is the base for many measurement instruments and most of the RF bridges are based on this circuit. The Wheatstone bridge has a total of four resistors; three of those have a known value and they are used to measure the value of the fourth. It usually works from DC up to low RF frequencies and it can be modified to be used for higher frequencies. The condition at which the voltage drop of  $R_1/R_2$  is equal to  $R_3/R_4$  leading to  $V=0$  and the voltmeter shows zero (balanced) is called the null condition [26].

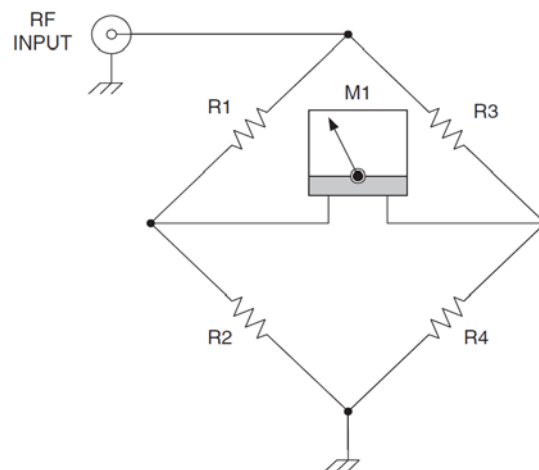


Figure 2-1 Wheatstone bridge- taken from [26]

When the power is dissipated in the resistive element of a bolometer it is converted to heat and changes the temperature. The aim is to have a sensor that can convert the heat to a DC voltage signal that can be measured using the Wheatstone bridge.

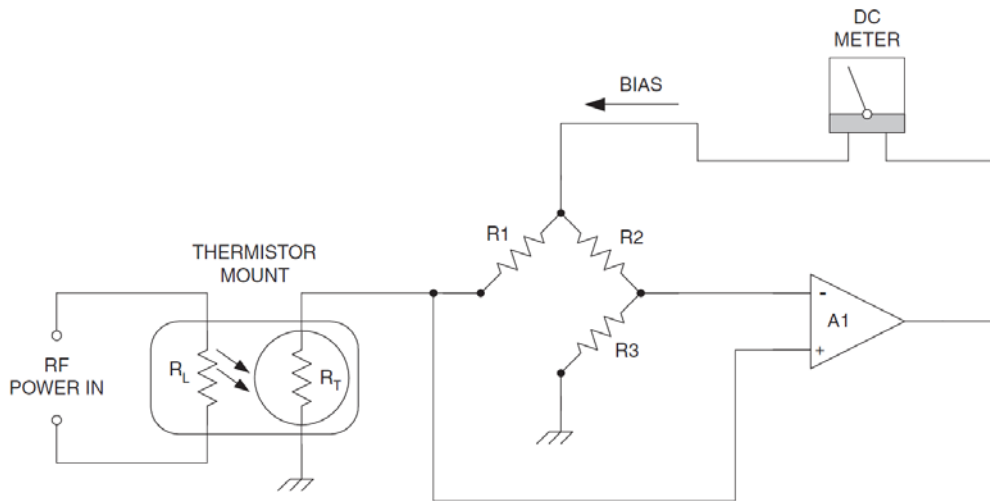


Figure 2-2 Wheatstone bridge circuit used with thermistor mount- taken from [26]

The bolometric power measurement is taken using the self-balancing bridge as shown in Figure (2-2). It uses a differential amplifier that produces output voltage proportional to the difference in the input voltages. When the bridge is balanced the output is zero, since there is no difference in the inputs. The bias voltage of the bridge is from the output of the amplifier. Changes in the resistance of the thermistor, results in changes in the voltage and unbalances the bridge; therefore the output of differential amplifier will be different to zero.

In Figure (2-2) the thermistor mount consists of a dummy load ( $R_L$ ) and a thermistor ( $R_T$ ). A DC current flowing in a thermistor causes self-heating. The resistance of the thermistor is adjusted when no power is applied to  $R_L$ . The resistance of the thermistor can be determined using the measured voltage on the output of differential amplifier and the bias current known from DC meter.

To rebalance the bridge the bias current needs to be changed by the appropriate amount and direction so that the resistance changes back to its value prior to application of power. From

the change in the bias current to keep the value of thermistor's resistance the same as before, the power that was dissipated and caused the change in thermistor's resistance value is determined. The null condition here is created when  $R_1/R_T = R_2/R_3$  [26].

### 2-1-2 Bolometer element circuit

Different types of bolometers exist but the metal bolometer is linear. A linear bolometer's electrical resistance is a linear function of the temperature [15]. A common design method, such as in the paper by Lane and Evans in 1961 [29], is a bolometer element mount followed by a short circuit termination and the whole is matched to the line, so most of the incident power will be absorbed in the bolometer element [8]. The element is located symmetrically in the cross-section of the waveguide where the electric field is transverse. This is shown in Figure (2-3), for this film to act as a non-reflecting termination and the power absorber, it should be followed by a short circuited waveguide at distance [29].

$$l = \frac{(2n - 1)\lambda_g}{4} \quad (2-1)$$

where  $\lambda_g$  is the guided wavelength and  $n=1, 2, 3$ , etc. [6] [30].

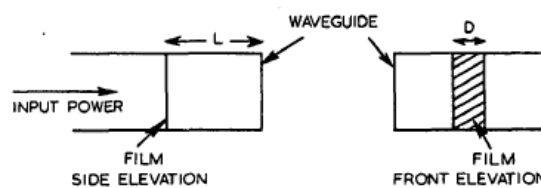


Figure 2-3 Side view and front view of metal film with width D and distance L from the waveguide short circuit

- taken from [29]

To have a non-reflecting termination the input impedance must become real and equal to the characteristic impedance of the waveguide [29]. The impedance of the sensitive element is made up of a resistive part  $R_M$  and a reactive part  $X_F$ . The resistive part of the element  $R_M$  is real and has to be equal to the characteristic impedance of the waveguide which is also real. The inductive reactance  $X_F$  can be cancelled with suitable short circuit termination reactance  $X_{Short\ circuit}$ , which can be obtained by choosing the correct distance to the short circuit placed behind the element [31] [32], as shown in Figure (2-4). The short circuit end of the waveguide is equivalent to a reactance in parallel to the equivalent lumped circuit of the bolometer element, Equation (2-3). Therefore, the input impedance of this circuit can be written as Equation (2-2) [29].

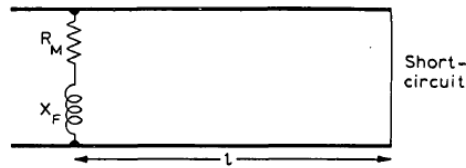


Figure 2-4 Equivalent circuit of the thin film in short circuited waveguide taken from [33]

$$Z = \frac{(R_M + jX_F)jX_{Short\ circuit}}{R_M + jX_F + jX_{Short\ circuit}} \quad (2-2)$$

$$jX_{Short\ circuit} = jZ_0 \tan(\gamma l) \quad (2-3)$$

Here  $\gamma$  is the propagation constant;  $Z_0$  is the characteristic impedance of the transmission line and  $l$  is the distance between the film and the short circuit wall;  $R_M$  is the resistance of the film;  $X_F$  is the reactance of the film; and  $X_{Short\ circuit}$  is the reactance representing the line terminated with the short circuit. Different types of bolometer mounts, such as thin film or thin wire, have been developed in order to match these elements to the guide [32]. Both a thin

metal film and a thin wire extending across a rectangular waveguide between two broad walls of the guide are obstacles that act as a shunt inductance [19]. The size of the element is important in determining the impedance of the element; which is then used in calculating the input impedance and affects the circuit being matched [30].

## **2-2 Bolometer literature review**

In 1967 Sakurai and Nemoto published a paper [32] on a thin film bolometer unit. They were investigating a design of a bolometer unit working at  $f = 35$  GHz. As mentioned in the paper, the main problems in constructing a bolometer with good performance at millimetre and sub-millimetre wavelengths lie with making the element and the mount.

To obtain a bolometer with good properties, it is desirable to have the size of the element negligible compared with the applied wavelength, for example platinum wire. However, it is also difficult to make millimetre wave bolometers that can handle high microwave power because of their small size. Thus to overcome the problem of size and therefore a decrease in efficiency, thin metal film was studied [32].

To match a dissipative material, whose size is smaller than the applied wavelength, to a waveguide, a resonance type matching method was used. This method requires at least two parameters of resistance, capacitance and inductance of the element or the mount to be independently set [32]. A thin metallic film acts as the inductive reactance when it is placed in the waveguide.

The thin film element equivalent circuit consists of a capacitance ( $C'$ ) in parallel with an inductance ( $L'$ ) and resistance in series, as shown in Figure (2-5). There is also another inductance ( $L''$ ) in series with these parameters that is the equivalent circuit of the electrode. The substrate is modelled by a capacitor ( $C$ ) which is in parallel with all these elements as shown in Figure (2-5a).

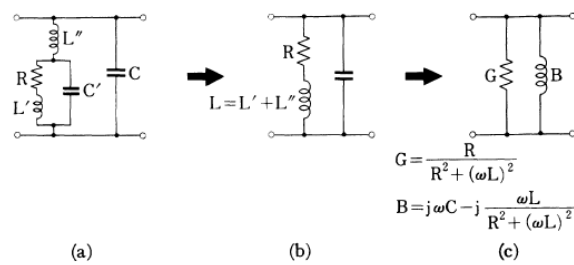


Figure 2-5 Equivalent circuit of bolometer element consisting of thin film, electrode and substrate-taken from [32].

The thin film capacitance ( $C'$ ) element is much smaller than the resistance ( $R$ ), so it is neglected and the circuit is simplified to the summation of inductances in series with film resistance, as well as the capacitance of substrate in parallel, as shown in Figure (2-5b). This can be further simplified to the equivalent circuit shown in Figure (2-5c). To achieve a matched condition, these parameters are adjusted by choosing the right shape for the element and a suitable distance behind the element for the short circuit.

In [32], the bolometer element was made of thin nickel film deposited on a thin mica substrate with electrodes made of gold; the mount only consisted of a short circuit and a flange. The dimensions of the film were about  $100 \text{ \AA}$  thickness, 1 mm in length and 0.6 mm

in width. The thickness of the mica substrate was 30  $\mu\text{m}$  and the gold electrode had a thickness of 2  $\mu\text{m}$ .

The results of this work are shown in Figure (2-6). The diagram is made up of three axes; the VSWR and the short circuit position, both versus frequency. There are two VSWR graphs; one shows that a good matched condition is accomplished at 33 GHz when the distance  $L_s$  to short circuit termination is fixed at 3.66 mm. The VSWR is less than 1.1 and over a bandwidth of 2 GHz.

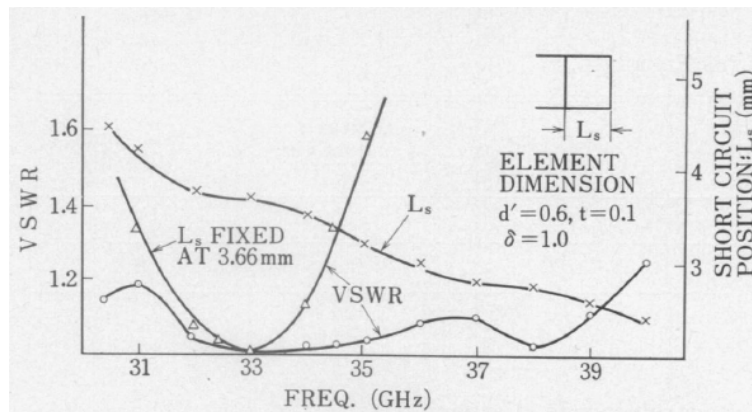


Figure 2-6 Frequency characterization of 35 GHz thin film bolometer unit- taken from [32].

The matching frequency can be changed by altering the position of the bolometer element in the waveguide. The graph labelled  $L_s$  shows the positions at which the short circuit should be located for each frequency to get the lowest VSWR. When the movable short circuit is adjusted properly at each frequency then the corresponding VSWR graph shows a good performance for the designed unit over the frequency range of 30 to 40 GHz [32].

If the size of the bead of a thermistor is small compared to the applied wavelength, it will have the same equivalent circuit as for the bolometer element described. Here the experiment is repeated for a small thermistor whose diameter is less than 0.1 mm, instead of thin film, and a perfect matched condition is also obtained. A thin film is used as the bolometer element here because of its excellent properties at short wavelength; such as high efficiency, low VSWR, wideband, good stability, high power handling capacity and simple and compact structure [32].

In the higher microwave region, other bolometers with good performance are also obtained by using thin-film technology. In 1992 L.Brunetti [21] designed a thin film bolometer that operates in the 26.5-40 GHz frequency range, by making a low-loss waveguide bolometer mount in WR-28. The mount is made of a precision waveguide section backed by a sliding end short and both are electroformed [21]. Placing a resistive thin film in the transverse cross section of the waveguide, terminated by a sliding short-circuited extension of guide of length  $l = (2n + 1)\lambda_g/4$  where  $n = 1,2,3,\text{etc.}$  produces an ideal reflection-less waveguide termination. Figures (2-7) and (2-8) show the section of rectangular waveguide with length  $a$  along the  $x$ -axis and widths  $b$  along the  $y$ -axis and the thin films located  $l = \lambda_g/4$  from the back-short where the electromagnetic waves are travelling along the  $z$ -axis.

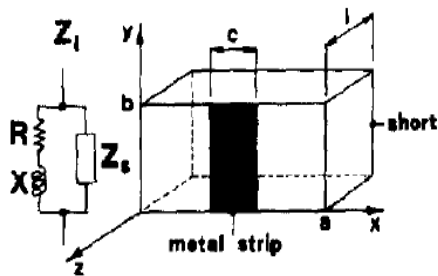


Figure 2-7 Thin-film bolometer inside a waveguide and its electrical equivalent circuit-taken from [21].

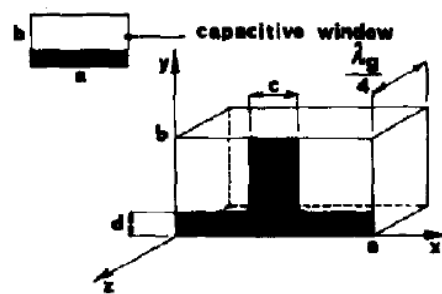


Figure 2-8 Matched thin film bolometer- taken from [21].

The thin-film is treated as lumped impedance with a uniform surface resistance and a series inductance which is parallel, connected to the impedance of the short circuit termination as shown in Figure (2-7). The element will be matched to the waveguide if the real part is equal to the wave impedance of the mode being transmitted and the imaginary terms being null. The imaginary part is made up of two parts where one is nulled as a consequence of choosing the proper distance of the element to the short end and the other part is nulled by adding a capacitive window of proper size, as shown in Figure (2-8), to have same value of susceptance as the remaining second part, but with a different sign to compensate the inductive part. According to [21] the total normalized admittance at the film position is

$$Y_{Total} = \left( \frac{r}{r^2 + x^2} \right) - j \left( \frac{x}{r^2 + x^2} \right) - j \cotg\left(\frac{2\pi l}{\lambda_g}\right) \quad (2-4)$$

Where,  $Y_{Total} = \frac{Z_0}{Z_{Total}}$ ,  $r = \frac{Z_0}{R}$ ,  $x = \frac{Z_0}{X}$  and  $l$  is distance to short circuit. To have the element matched to waveguide the real term has to be equal to one, the third term is nullified by having  $l = \frac{\lambda_g}{4}$  and the second term is removed by adding a capacitive window with susceptance equal to  $\frac{r^2+x^2}{x}$ , Figure (2-8).

The sensitive element of the bolometer in [21] is a 100 Å thick nickel film. This thickness is chosen so the film is much smaller than the minimum wavelength in the metal and to have a DC resistance of 200 Ω when the bolometer is DC biased. Nickel is chosen as the material because of its high temperature coefficient of resistance ( $\alpha$ ), to obtain a relatively high sensitivity; also it has good stability, which can be increased by modifying the physical

structure of the film. This type of bolometer is narrow band and it is named a resonant type bolometer. For  $R=200\ \Omega$  and DC power bias 82 mW, the sensitivity is almost  $0.6\ \Omega / \text{mW}$  which is not among the best values in the literature.

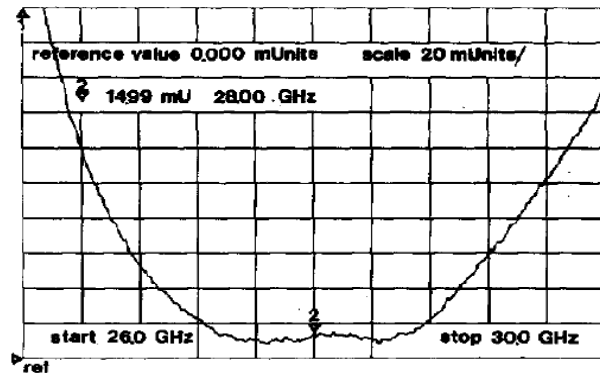


Figure 2-9 Bolometer reflection coefficient in its working frequency band- taken from [21].

The widths of capacitive and inductive films in Figure (2-8) are found in a way to match the bolometer at 28 GHz. Figure (2-9) shows that at the resonance frequency reflection coefficient is near 0.01 and if a maximum value of 0.1 is acceptable, then the matching bandwidth is about 3 GHz. The designed bolometer can be used as the thermal load of a micro calorimeter and also as a high-performance power meter with a power-handling capability of about 80 mW [21].

In 1985, T. Inoue and I. Yokoshima [25] designed a barretter mount at W-band (75-110 GHz) operating at  $f = 94\ \text{GHz}$  with effective efficiency of more than 90 %. A thin film resistor perpendicular to the waveguide axis, with a specific shape and resistance and located at a suitable length to the short circuit termination can be matched to the waveguide. A wideband characteristic was achieved by adding a capacitive window where the resistor is located. The resistor material had a large resistance temperature coefficient in order to be suitable to be used as the bolometer.

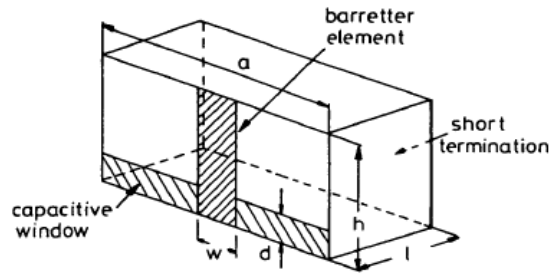


Figure 2-10 Barretter mount structure- taken from [25]

The basic structure of the barretter mount is shown in Figure (2-10). In order to widen the matching bandwidth, it was required to compensate the inductive reactance of the barretter element with a capacitive element and also by choosing the length to termination as  $l = \lambda_g/4$ .

The DC bias produces  $R = 200 \Omega$  with  $Z_0 = 484 \Omega$  at 94 GHz and the parameters are  $w/a=0.077$  and  $d/h = 0.513$ ;  $w = 0.2$  mm and  $d = 0.65$  mm.

The film is made of nickel and the substrate is a polyimide sheet with a thickness of  $12.5 \mu\text{m}$  and the waveguide mount is gold-plated to minimize the wall loss.

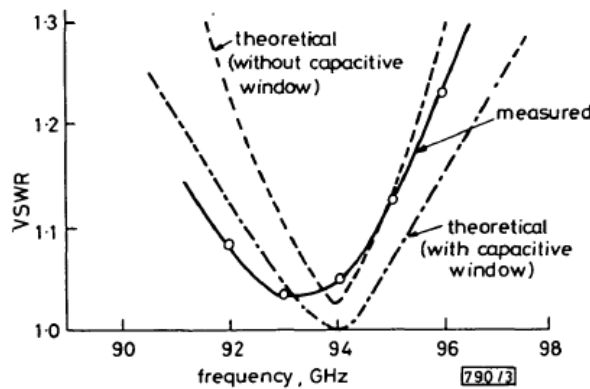


Figure 2-11 VSWR versus operation frequency for the designed barretter mount- taken from [25]

Figure (2-11) shows the VSWR of the designed barretter mount versus the frequency of operation. The resultant curves illustrate the graph of measurement of the barretter mount and

the theoretical graphs with and without the capacitive window. As can be seen the VSWR of the theoretical curve with the capacitive window has the minimum value and it is almost exactly equal to one at  $f = 94$  GHz. The bandwidth of the bolometer, for a VSWR smaller than 1.2, is about 5 GHz.

The effective efficiency of the mount was measured using a micro-calorimeter for W-band with uncertainty of about 0.6%. Averaging three measurements, the effective efficiency was calculated to be  $99.86 \pm 0.06\%$ , which is much higher than most of the bolometers previously working in this frequency band. A sensitivity of  $2.9 \text{ } \Omega/\text{mW}$  is obtained for this barretter mount. The accuracy of this power measurement is comparable with longer wavelength power measurements [25].

## CHAPTER 3 -THEORETICAL FOUNDATIONS

This chapter briefly explains the transmission line theories and waveguide propagation equations that are used for the calculations of this project in order to design the power detector.

### 3-1 Transmission lines

Transmission lines guide the propagation of energy from one point to another. The wave equations have travelling wave solutions for waves propagating in a  $+z$  direction and  $-z$  direction as given below [34]:

$$V(z) = V_0^+ e^{-\gamma z} + V_0^- e^{+\gamma z} \quad (3-1)$$

$$I(z) = I_0^+ e^{-\gamma z} + I_0^- e^{+\gamma z} \quad (3-2)$$

where  $V_0^+$  is the voltage amplitude of the voltage wave travelling in a  $+z$  direction and  $I_0^+$  is the current amplitude of the current wave in the same direction;  $V_0^-$  is the amplitude of the voltage wave travelling in a  $-z$  direction and  $I_0^-$  is current amplitude of the  $-z$  directed current. The term  $e^{-\gamma z}$  represents the wave travelling in a  $+z$  direction and  $e^{+\gamma z}$  represents the wave travelling in a  $-z$  direction;  $\gamma$  is the propagation constant given by [31]:

$$\gamma = \alpha + j\beta = \sqrt{(R + j\omega L)(G + j\omega C)} \quad (3-3)$$

Here  $G$  is the conductance per unit length of the transmission line;  $R$  is the resistance per unit length;  $C$  is the capacitance per unit length and  $L$  is the inductance per unit length of the

transmission line. The propagation constant is made of a real part that is the attenuation constant  $\alpha$  and an imaginary part which is phase constant  $\beta$  and it is a function of frequency. The amplitude of the wave travelling in a transmission line attenuates by  $e^{-\alpha z}$ .

A transmission line is characterized by two factors: the characteristic impedance  $Z_0$  and the propagation constant  $\gamma$ . The characteristic impedance is the ratio of the voltage amplitude to the current amplitude of the travelling wave [31].

$$Z_0 = \frac{V_0^+}{I_0^+} = -\frac{V_0^-}{I_0^-} = \frac{R + j\omega L}{\gamma} = \sqrt{\frac{R + j\omega L}{G + j\omega C}} \quad (3-4)$$

### 3-1-1 Lossless line

To simplify the analysis quite often a lossless transmission medium is considered. In this case the attenuation constant  $\alpha$  is zero. The conductance  $G$  and resistance  $R$  are therefore zero for the line and the propagation constant becomes imaginary.

$$\gamma = j\omega\sqrt{LC} = j\beta \quad (3-5)$$

The imaginary propagation constant leads to characteristic impedance of the line being a real number.

$$Z_0 = \sqrt{\frac{L}{C}} \quad (3-6)$$

### 3-2 Reflection coefficient

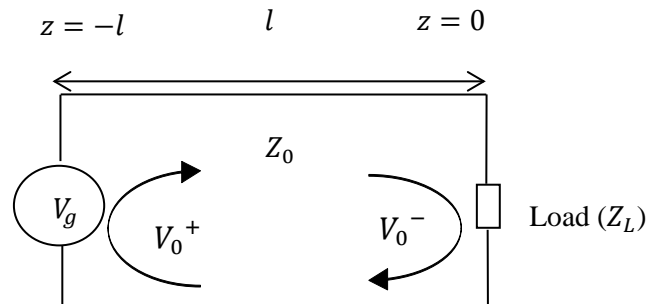


Figure 3-1 transmission line model with voltage generator  $V_g$ , characteristic impedance  $Z_0$  and load impedance  $Z_L$ .

Figure (3-1) shows the circuit of a transmission line connecting a generator to a load. The load is located at  $z = 0$  and the source is located at  $z = -l$ . The ratio of the amplitude of reflected voltage to the amplitude of incident voltage at the load is called the reflection coefficient and it is a dimensionless parameter, given by: [35]

$$\Gamma = \frac{V_0^-}{V_0^+} = \frac{Z_L - Z_0}{Z_L + Z_0} \quad (3-7)$$

where  $Z_L$  is the load impedance. The load impedance is generally a complex number and therefore may lead to a complex reflection coefficient. When the load is not matched with the line there is a reflected wave in the opposite direction of the incident wave. The reflection coefficient range is  $-1 \leq \Gamma \leq 1$ . A load is matched to the line when its impedance is equal to the characteristic impedance of the line. In this case there won't be any reflection from the load and the reflection coefficient will be zero [31]. The magnitude of  $\Gamma$  doesn't change at any point along the line; only the phase changes [36].

There are some special cases such as

- Short circuit, where

$$Z_L = 0 \text{ therefore } \Gamma = -1$$

- Open circuit, where

$$Z_L = \infty \text{ therefore } \Gamma = 1$$

- Matched condition where

$$Z_L = Z_0 \text{ therefore } \Gamma = 0$$

### 3-2-1 Standing waves

In a transmission line that is terminated with a load, with waves incident to the load and reflecting back, there are two waves that travel in the opposite directions and are present at the same time. Therefore they are added together and a standing wave is produced [31]. This is characterised by the VSWR (voltage standing wave ratio). It is a dimensionless value that is derived using the ratio of the maximum voltage to minimum voltage found from the result of the wave summation.

$$VSWR = \left| \frac{V_{max}}{V_{min}} \right| = \left| \frac{I_{max}}{I_{min}} \right| \quad (3-8)$$

Using the standing wave ratio is another way of finding the reflection coefficient.

$$|\Gamma| = \frac{VSWR - 1}{VSWR + 1} \quad (3-9)$$

VSWR is equal to 1 for the matched condition and it is  $\infty$  for the open circuit and short circuit transmission line.

### 3-2-2 S-parameters

It is important to see how much gain or loss there is when transmitting an information signal. S-parameters or scattering parameters describe the response of an  $N$ -port linear time invariant network to voltage, current and power inputs at each port. For a two port network the system can be treated like the transmission line above, which for any incident wave, part of it is transmitted and part of it is reflected back. The scattering matrix of an  $N$ -port network is  $n \times n$  matrix. For each term  $S_{ij}$  of the  $n \times n$  matrix:  $i$  refers to the signal exiting port  $i$  and  $j$  refers to the signal entering port  $j$ . The values can be found by the ratio of the reflected voltage signal and incident voltage signal. S-parameters are complex values but the gain and loss are usually determined by the magnitude in decibels (dB).

For  $i = j$ ,  $S_{ij}$  shows how much of the incident wave is reflected back and comes out of the same port as the incident signal. This is equal to the reflection coefficient at the input port [37] and it is the same as a return loss with a negative sign [38] [39].

$$RL(dB) = 10 \log \left( \frac{P_i}{P_r} \right) = 20 \log \left( \frac{1}{|\Gamma|} \right) = -20 \log(|S_{11}|) \quad (3-10)$$

A matched load has a return loss of  $\infty$  dB or no reflected power; whereas a total reflection has a return loss of 0 dB [35].

### 3-3 Input impedance

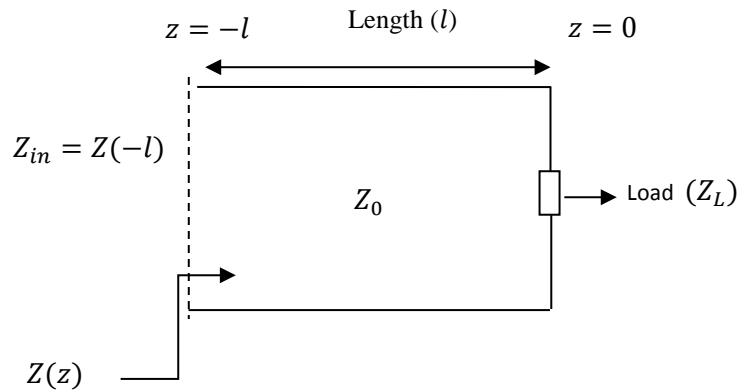


Figure 3-2 transmission line model with characteristic impedance  $Z_0$  and load impedance  $Z_L$ .

The impedance  $Z(z)$  of a transmission line shown in Figure (3-2) is the ratio of the total voltage (incident and reflected wave voltages) to the total current at any point  $z$  on the line. It is different from the characteristic impedance of the line  $Z_0$ , see Equation (3-4), which relates the ratio of the forward propagating voltage and forward current. Generally it is a complex number and consists of an input resistance  $R_{in}$  and an input reactance  $X_{in}$ .

$$Z(z) = R + jX \quad (3-11)$$

The input impedance at the input of the line is calculated as below [31]:

$$Z(z) = \frac{V(z)}{I(z)} \quad (3-12)$$

Using Equations (3-1) and (3-2), Equation (3-12) can be written as:

$$Z(z) = \frac{V_0^+ [e^{-\gamma z} + \Gamma e^{\gamma z}]}{V_0^+ [e^{-\gamma z} - \Gamma e^{\gamma z}]} Z_0 \quad (3-13)$$

Substituting Equation (3-7) for  $\Gamma$  and considering  $e^{\gamma z} = \cosh \gamma z + \sinh \gamma z$  and  $e^{-j\gamma z} = \cosh \gamma z - \sinh \gamma z$ , Equation (3-13) becomes:

$$Z(z) = Z_0 \left( \frac{Z_L + Z_0 \tanh(\gamma z)}{Z_0 + Z_L \tanh(\gamma z)} \right) \quad (3-14)$$

For lossless line where  $\alpha = 0$  the input impedance is:

$$Z_{in} = Z(-l) = Z_0 \left( \frac{Z_L + jZ_0 \tan \beta l}{Z_0 + jZ_L \tan \beta l} \right) \quad (3-15)$$

This expression is important for the design equations derived for a power detector in Chapter 4 and Chapter 5. To complete the definitions in this chapter, the well-known general equation of the wavelength of electromagnetic waves in lossless transmission line is:

$$\lambda = \frac{c}{f} = \frac{1}{f\sqrt{LC}} = \frac{1}{f\sqrt{\mu\varepsilon}} = \frac{2\pi}{\beta} \quad (3-16)$$

$$\beta = \omega\sqrt{LC} = \omega\sqrt{\mu\varepsilon} = \frac{2\pi}{\lambda} \quad (3-17)$$

Where  $\mu$  and  $\varepsilon$  are magnetic permeability and electrical permittivity of the medium, respectively.

Phase velocity is also derived below and speed of light in vacuum is  $c_0 = 3 \times 10^8$  m/s.

$$c = \frac{\omega}{\beta} = f\lambda = \frac{1}{\sqrt{LC}} = \frac{1}{\sqrt{\mu\varepsilon}} \quad (3-18)$$

### 3-4 Skin depth

The skin depth is the depth at which the amplitude of the propagating electromagnetic fields in the conductor decays to  $e^{-1}$  or about 37% of the initial amplitude. The skin depth  $\delta$  is given by [35].

$$\delta = \sqrt{\frac{2}{\mu\omega\sigma}} = \frac{1}{\sqrt{\pi f\mu\sigma}} \quad (3-19)$$

Equation (3-19) shows the skin depth is a function of frequency, permeability and electrical conductivity of the material. As any of these parameters increases the skin depth decreases, showing that the depth in which the wave can propagate in the conductor becomes smaller. The skin depth is a function of frequency, therefore for the case of DC, where  $f = 0$  Hz,  $\delta$  approaches infinity meaning that the depth in which the current will propagate in the conductor is limitless.

### 3-5 Waveguides

Waveguides can be considered as types of transmission lines. A waveguide is a hollow conducting pipe with a uniform cross section, which directs the propagation of an electromagnetic wave in a particular direction [40]. They can have different shapes of cross-sections such as rectangular, circular, square, and elliptical. Generally they are used for electromagnetic waves within the frequency range of 300MHz up to about 300GHz. Waveguides are more advantageous than coaxial cables or other transmission lines since they

have lower signal attenuation and the ability to transmit more power, at higher frequencies [31] [41].

There are different electromagnetic wave modes that can be transmitted in waveguides. Waveguides are either made of conductors filled in with air or dielectrics, which are called metal waveguides, or they are made of dielectrics only and are called dielectric waveguides. Dielectrics have permittivity and permeability of  $\epsilon$  and  $\mu$ , respectively and the dielectric usually used to fill the interior of metal waveguides is vacuum or air. The size of the dimensions of waveguide's cross sections is chosen in a way to be able to propagate the dominant mode in the chosen frequency band of operation [35] [42].

### **3-5-1 Modes**

Electromagnetic waves are analysed by wave equations, which are derived from the Maxwell equations. Different Eigen function solutions to the wave equation system are the modes. Based on different modes, different electric and magnetic field configurations are created. Modes occur due to the boundary condition restrictions. There are different modes in existence such as Transverse Electric (TE), Transverse Magnetic (TM), Transverse Electric and Magnetic (TEM) modes; but only two modes, TE and TM, can propagate in rectangular waveguides [35] [43].

A waveguide can support an infinite number of TE and TM modes, each of which has their own cut-off frequency; whereas TEM transmission lines have zero cut-off frequency [40].

### 3-5-2 Rectangular waveguides

A rectangular waveguide is a hollow metallic tube with a rectangular cross section. Only TE and TM modes can propagate in this waveguide. The Transverse Electric (TE) mode occurs when the only available electric field components are the transverse electric fields and there is no longitudinal electric field  $E_z = 0$  along the propagation direction ( $z$ -axis). The electric field pattern of the wave radiates perpendicular to the propagation direction and only the  $z$  component of the magnetic field is on the  $z$ -axis,  $H_z$ .

The Transverse Magnetic (TM) mode takes place when the magnetic field pattern of the wave is perpendicular to the propagation direction. There is no longitudinal magnetic field along that direction ( $z$ -axis) in this mode; only the electric field,  $E_z$  is in the  $z$  direction.

The subscript terms  $m$  and  $n$  of  $TE_{mn}$  and  $TM_{mn}$  modes show the number of oscillations along the  $x$  axis and  $y$  axis of the cross section of the waveguide, respectively [35] [43].

These modes have a cut-off frequency below which propagation is not possible [35].

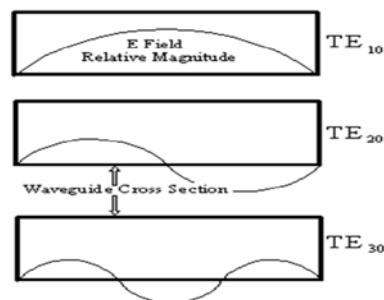


Figure 3-3 Electric field patterns for TE<sub>10</sub>, TE<sub>20</sub> and TE<sub>30</sub> - taken from [39]

Figure (3-3) [39] shows the cross section of three rectangular waveguides; here, in the  $TE_{10}$  mode there is one oscillation of electric fields; in  $TE_{20}$  mode there are two and in  $TE_{30}$  mode there are three oscillations.

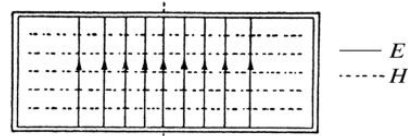


Figure 3-4 Electric field and magnetic field for mode  $TE_{10}$  - taken from [44]

Figure (3-4) [44] shows the electric field and magnetic field of the dominant  $TE_{10}$  mode over the cross-section of a rectangular waveguide. For  $TE_{10}$  mode,  $E_x, E_z, H_y = 0$  and only three field components are propagating in the waveguide [35].

$$E_y = \frac{-j\mu\omega a}{\pi} A_{10} \sin\left(\frac{\pi x}{a}\right) e^{-j\beta z} \quad (3-20)$$

$$H_x = \frac{j\beta a}{\pi} A_{10} \sin\left(\frac{\pi x}{a}\right) e^{-j\beta z} \quad (3-21)$$

$$H_z = A_{10} \cos\left(\frac{\pi x}{a}\right) e^{-j\beta z} \quad (3-22)$$

Where  $A_{10}$  is the amplitude constant for  $TE_{10}$  mode,  $\omega$  is the angular frequency,  $\beta$  is the phase constant,  $a$  is the width of the waveguide and  $\mu$  is permeability.

The transverse wave impedance, relating the transverse electric and magnetic fields, is:

$$Z_{TE} = \frac{E_x}{H_y} = \frac{-E_y}{H_x} = \frac{\omega\mu}{\beta} \quad (3-23)$$

### 3-5-3 Cut-off frequency

The cut-off frequency is a point in the frequency band of operation, at which the system starts to cut off the operation and attenuates the passing signal. Waveguides act like high pass filters; meaning that for the waves with the operation frequency range below the waveguide's cut-off frequency the wave will be attenuated by the waveguide; whereas waves with a frequency of operation above the cut-off frequency will be propagated in the guide with minimum attenuation [35] [45].

The cut-off frequency of rectangular waveguides is calculated as:

$$f_{c_{mn}} = \frac{k_c}{2\pi\sqrt{\mu\epsilon}} = \frac{1}{2\pi\sqrt{\mu\epsilon}} \sqrt{\left(\frac{m\pi}{a}\right)^2 + \left(\frac{n\pi}{b}\right)^2} \quad (3-24)$$

where:

$$\beta = \sqrt{k^2 - k_c^2} = \sqrt{k^2 - \left(\frac{m\pi}{a}\right)^2 - \left(\frac{n\pi}{b}\right)^2} \quad (3-25)$$

where  $m$  and  $n$  are the particular mode numbers and are the number of variations in the E-field pattern in the  $x$ -axis and  $y$ -axis, respectively. Parameters  $a$  and  $b$  are width and height of the rectangular waveguide cross-section;  $k$  is the wavenumber calculated by Equation (3-17).

In order to have a propagating mode, the following condition should be satisfied.

$$k > k_c = \sqrt{\left(\frac{m\pi}{a}\right)^2 + \left(\frac{n\pi}{b}\right)^2} \quad (3-26)$$

For the dominant mode  $TE_{10}$  where  $n=0$  the second term in Equation (3-24) is eliminated and the cut-off frequency equation results in:

$$f_{cut-off} = \frac{1}{2a\sqrt{\mu\epsilon}} \quad (3-27)$$

The mode with the smallest cut-off frequency is called dominant mode and the lowest cut-off happens for  $TE_{10}$  mode in rectangular waveguide.

Below the cut-off frequency of the mode, the propagation constant is real:  $\gamma = \alpha$  indicating attenuation. These modes are also called evanescence modes. On the other hand for lossless waveguide, for modes with an operation frequency larger than the cut-off frequency, the propagation constant is imaginary:  $\gamma = j\beta$  indicating propagation.

Considering the losses, usually from conducting walls, causes the propagation constant to have a real part above the cut-off frequency as well. The propagating field will then be attenuated along the guide, causing a power loss [34]. The calculations in this thesis assume no loss of this type.

The dimensions of the waveguide and operation frequency are usually chosen in such a way that only the dominant mode is used.

### 3-6 X-band waveguide characteristics

The X-band waveguide (WR90) is a rectangular waveguide that operates in the X-band frequency range from 8.2 GHz to 12.4 GHz and the dimensions of its rectangular cross section are  $a = 22.86$  mm and  $b = 10.16$  mm. The X-band waveguide is used in this project.

The cut-off frequency for the TE<sub>10</sub> mode from Equation (3-27) is [35]:

$$f_{cut-off} = \frac{c_0}{2 \times a} = 6.57 \text{ GHz}$$

The wavelength of the guided wave in the X-band waveguide at  $f = 10$  GHz is calculated from Equation (3-16) and using Equation (3-25) to calculate  $\beta$  of TE<sub>10</sub> mode in the rectangular waveguide:

$$\lambda_g = \frac{2\pi}{158.0461} = 39.75 \text{ mm}$$

The characteristic impedance of the X-band rectangular waveguide at a frequency of 10 GHz is [46]:

$$Z_0 = \frac{2b \cdot 377\lambda_g}{a \cdot \lambda} = 444.082 \text{ Ohms} \quad (3-28)$$

### 3-7 Short circuit termination

There are some special cases of load for a lossless line, which can be determined from Equation (3-15), given and discussed below:

- For a case of lossless short circuit load where  $Z_L = 0$  it is  $Z_{in} = jZ_0 \tan \beta l$
- For a case of lossless open circuit load where  $Z_L = \infty$  it is  $Z_{in} = -jZ_0 \cot \beta l$

For these cases the impedance is reactive and can be either capacitive or inductive and its value changes depending on the length of the line.

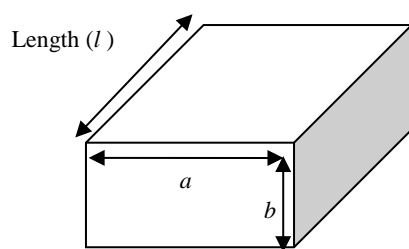


Figure 3-5 Rectangular waveguide

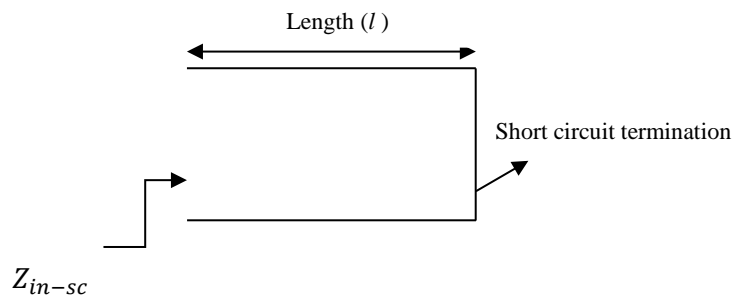


Figure 3-6 Side view of rectangular waveguide with short circuit termination

Figure (3-5) shows a rectangular waveguide and Figure (3-6) shows the same waveguide from the top, illustrating that there is an input port and the back of waveguide is short-circuited.

Assuming the waveguide behaves as a transmission line, at the short circuit termination the voltage is zero, the current is maximum and load impedance is zero  $Z_L = 0$ ; therefore

$\Gamma = -1$  using Equation (3-7). When the wave reaches a short circuit transmission line it will reflect back. The input impedance of a short-circuited line at distance  $l$  from the termination, using Equation (3-15), is calculated to be [47]:

$$Z_{in-sc} = Z_0 \left( \frac{0 + jZ_0 \tan \beta l}{Z_0 + 0} \right) = jZ_0 \tan \beta l = jX_{sc} \quad (3-29)$$

For the case of a short circuit line the input impedance is purely reactive and there is no resistance.

For a short circuit line when  $\tan \beta l > 0$  or when the length is between  $0 < l < \frac{\lambda}{4}$  and the value of  $Z_{in} > 0$ ; then line appears inductive, acting like an equivalent inductor  $L_{eq}$  whose impedance is equal to [31]:

$$Z_{in-sc} = jZ_0 \tan \beta l = j\omega L_{eq} \quad (3-30)$$

On the other hand, when  $\tan \beta l < 0$  or when  $\frac{\lambda}{4} < l < \frac{\lambda}{2}$  and the value of  $Z_{in} < 0$ ; then line appears capacitive, acting like an equivalent capacitor  $C_{eq}$  whose impedance is equal to [48]:

$$Z_{in-sc} = jZ_0 \tan \beta l = \frac{1}{j\omega C_{eq}} \quad (3-31)$$

It is the opposite for a open circuit line. A graph of the short-circuited waveguide input impedance  $Z_{in-sc}$  for an X-band waveguide for different lengths of waveguide is plotted in Figure (3-7), using the waveguide characteristics determined previously. The figure shows that the input impedance is changing as the trigonometric function  $\tan(\beta l)$ , so as the length to the back short changes the input impedance changes. The graph is repeated every  $l = \lambda_g/2$

where the impedance becomes zero, also at  $l = n\lambda_g/4$  the value of impedance approaches infinity. As the length changes the sign of input impedance also changes as discussed earlier. Between  $0 < l < \frac{\lambda}{4}$ , the value of reactance is positive or inductive and then as mentioned previously, when  $\frac{\lambda}{4} < l < \frac{\lambda}{2}$ , it becomes negative or capacitive.

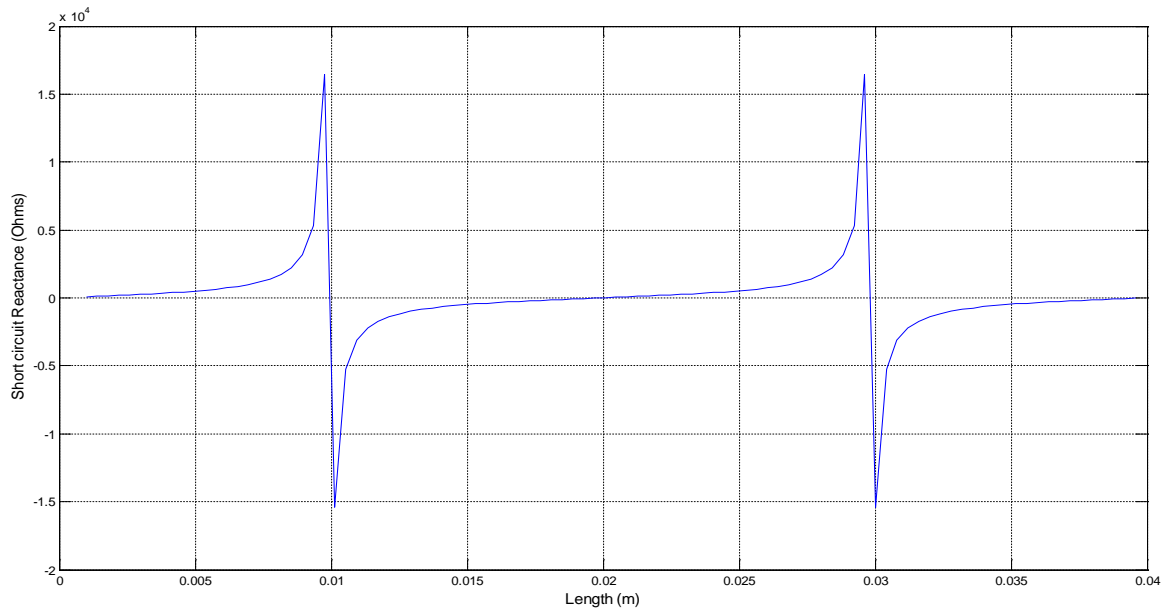


Figure 3-7 Graph of  $Z_{in}$  of waveguide with short circuit termination versus length in metres, Equation (3-29),

where  $\lambda_g = 39.75$  mm and  $Z_0 = 444.08$  Ohms

### 3-8 Comparing X-band waveguide, WR6 and WR3 for TE<sub>10</sub>

Information about the X-band waveguide and other waveguides mentioned in this thesis is provided in Table (3-1):

Table 3-1 characteristics of different waveguides

Frequency band	Frequency range (GHz)	Inside dimensions (mm)	Cut-off frequency (GHz)	Guided wavelength (mm)	$Z_0$ ( $\Omega$ )
X-band (WR90)	8.2 to 12.4	22.86 x 10.16	6.56	39.8	444.08
D-band (WR6)	110 to 170	1.651 x 0.8255	90.85	28	446.04
G-band (WR3)	220 to 325	0.8636 x 0.4318	173.69	12	462.37

This table illustrates the physical parameters and some important characteristics of WR90, WR6 and WR3. Here WR90 is considered for the design of the power sensors here, but the same approach can be used for WR6 and WR3 at a later stage. It is simple to use the values mentioned in this table to replace those parameters of WR90. For higher frequencies the dimensions of the waveguide and the guided wavelength become smaller still.

## **CHAPTER 4- IMPLEMENTING A NON REFLECTIVE POST IN A WAVEGUIDE**

### **4-1 Introduction**

This chapter discusses the theory of impedance matching when there is an obstacle in a short circuit terminated waveguide. The equivalent circuit of the structure is explained and the matching procedure is examined using the transmission line theory. The obstacle considered in this chapter is a metal post that is used as an integral part for the final power sensor structure. This structure is used as it is simpler to design and the equations for metal posts are available in the literature. Initially the aim is to prove the theory and later it can be used at different frequencies for the power sensor design.

### **4-2 Matching**

In this chapter a power detector is designed using the transmission line theory explained in the previous chapter. To simplify the project this power detector is designed with a metallic post in the centre of the X-band waveguide that is connected to the broad walls of the waveguide at both ends and at a distance  $l$  to the short circuit termination. This post is positioned in a way that has the behaviour of an inductor as well as being resistive and its impedance is considered in the overall input impedance of the waveguide.

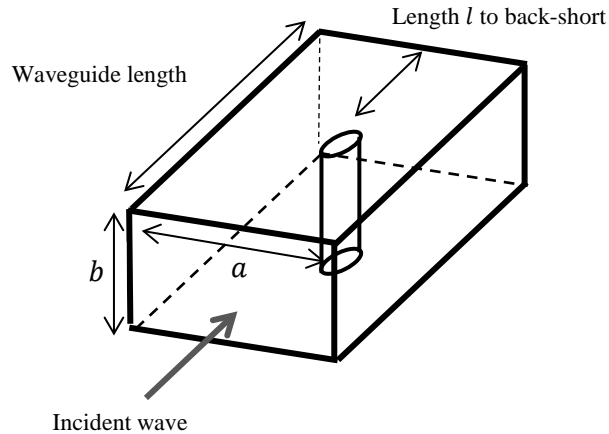


Figure 4-1 Waveguide with obstacle

Figure (4-1) shows the post located in the rectangular waveguide. In the figure  $a$  and  $b$  are width and height of the waveguide respectively;  $l$  is the distance of the post from the back-short. The arrow pointing towards the waveguide port is the incident wave.

#### 4-2-1 Waveguide with short circuit termination and inductive and resistive element

A rectangular waveguide supporting the  $TE_{10}$  mode with short circuited termination is considered. A narrow post is located symmetrically in the transverse cross section of the rectangular waveguide attached to the broad walls. The equivalent input impedance of the waveguide is determined by considering the input impedance of a short circuited line in parallel with the impedance of a metallic post. The post is resistive and it also has a reactance; the way it is located in the waveguide makes it inductive. The size of the post is important as it affects its impedance; it will alter the input impedance and consequently the reflection coefficient.

The impedance of a resistive and reactive element is:

$$Z_{element} = R + jX \quad (4-1)$$

Figure (4-2) shows the schematic of a resistive and reactive element located at distance  $l$  to the short circuit termination;  $Z_{in-sc}$  is the input impedance of the transmission line at distance  $-l$  from the short circuit. The other arrow  $Z_{in}$  shows the input impedance of the whole circuit.

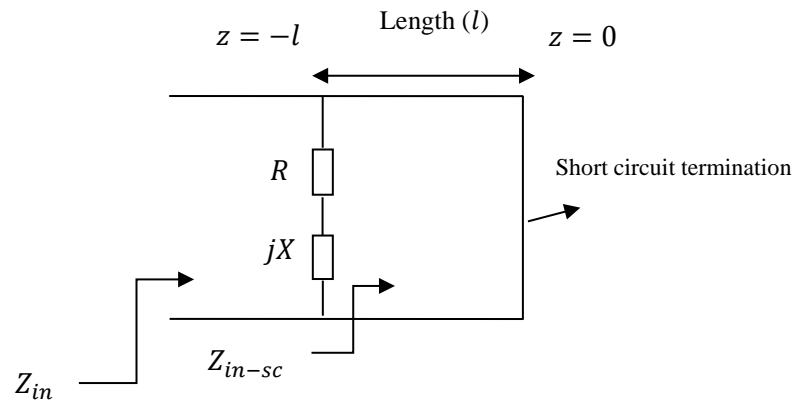


Figure 4-2 Equivalent circuit of a waveguide with short circuit termination and resistive, reactive element.

$Z_{in-sc}$  is given by:

$$Z_{in-sc}(-l) = jZ_0 \tan \beta l = jX_{sc} \quad (4-2)$$

Equation (4-2) is the equivalent input impedance of a short circuit transmission line that was derived in Chapter 3 as Equation (3-29) and repeated here, as it will be used in the calculations.

The circuit in Figure (4-2) can be reduced to the circuit in Figure (4-3) by replacing the transmission line of length  $l$  with a short circuit termination with its equivalent input impedance  $Z_{in-sc}$  and replace  $X$  with inductive element.

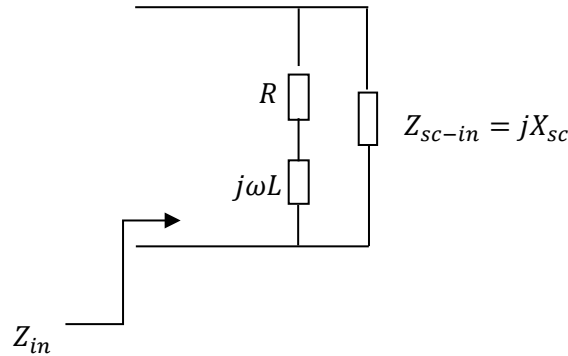


Figure 4-3 Side view of waveguide with short circuit termination and resistive, inductive element.

The input impedance  $Z_{in}$  can now be determined using Equation (4-1) for  $Z_{element}$ , which includes resistance as well as inductance in parallel with the reactive impedance of the short circuit termination. The new input impedance  $Z_{in}$  is:

$$Z_{in} = \frac{Z_{element} \times Z_{sc-in}}{Z_{element} + Z_{sc-in}} = \frac{(R + j\omega L)jX_{sc}}{R + j\omega L + jX_{sc}} \quad (4-3)$$

$$Z_{in} = \frac{RX_{sc}^2}{R^2 + X^2 + X_{sc}^2 + 2XX_{sc}} + j \frac{R^2X_{sc} + X^2X_{sc} + XX_{sc}^2}{R^2 + X^2 + X_{sc}^2 + 2XX_{sc}} \quad (4-4)$$

Equation (4-4) gives a complex impedance.

To find the reflection coefficient, Equation (3-7) stated in Chapter 3 is used. This equation is repeated here because it is used widely:

$$\Gamma = \frac{Z_L - Z_0}{Z_L + Z_0} = \frac{Z_{in} - Z_0}{Z_{in} + Z_0} \quad (4-5)$$

Here load impedance  $Z_L$  is substituted with the equivalent input impedance  $Z_{in}$  of the short circuit and post combination;  $Z_0$  is the characteristic impedance of the waveguide [31].

The aim is to have zero reflection, therefore  $Z_{in}$  should be equal to the characteristic impedance, as in Equation (4-5). On the other hand, the characteristic impedance of the waveguide is a real number for the lossless case; therefore to achieve a matched condition the imaginary part of Equation (4-4) must be zero [29].

Setting the imaginary part of Equation (4-4) equal to zero gives a:

$$X_{sc} = \frac{-R^2 - X^2}{X} \quad (4-6)$$

Also the real part of  $Z_{in}$  in Equation (4-4) should be set equal to  $Z_0$  of the waveguide; this results in:

$$Z_0 = \frac{R^2 + X^2}{R} \quad (4-7)$$

Figure (4-4) shows the reflection coefficient, Equation (4-5), versus the length to back-short for a resistive and inductive element. The input impedance is calculated from Equation (4-3) for different values of resistance and the corresponding value of inductive reactance that is calculated from Equation (4-7). The length to back-short at which the reflection coefficient is zero is seen on the graph and it is derived later in this chapter.

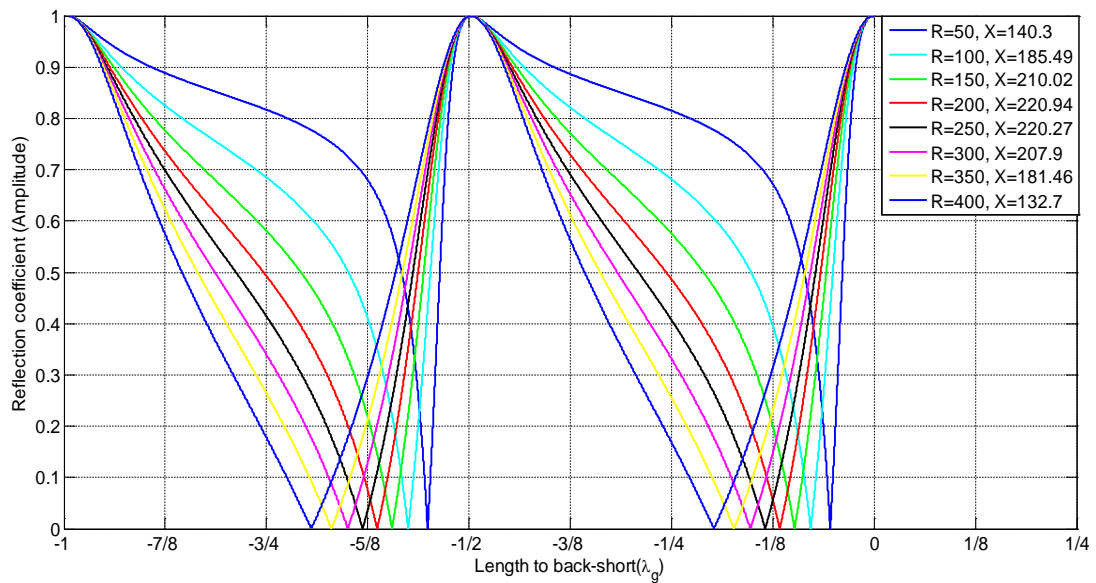


Figure 4-4 Reflection coefficient of resistive and inductive element vs length to back short,  $\lambda_g = 40 \text{ mm}$

As an example for  $R = 200 \text{ } \Omega$  the reactance is calculated to be  $X=220.94 \text{ } \Omega$  from Equation (4-11) and from Figure (4-4) it can be seen that for an inductive reactance at  $l = -4.7 \text{ mm}$  from the short circuit termination, the reflection coefficient is zero. The back-short length for the zero reflection coefficient is calculated below.

Considering Equation (4-6) and by knowing Equation (4-2) derived earlier for the impedance of a short circuit transmission line, the following formula for calculating the length between the element and short circuit that results in zero reflection coefficients is derived as:

$$Z_0 \tan \beta l = \frac{-R^2 - X^2}{X} \quad (4-8)$$

Substituting Equation (4-7) for  $Z_0$  gives

$$\left(\frac{R^2 + X^2}{R}\right) \tan \beta l = \frac{-(R^2 + X^2)}{X} \quad (4-9)$$

Hence, the length to the short circuit termination that results in zero reflection is found as:

$$l = \frac{1}{\beta} \tan^{-1}\left(\frac{-R}{X}\right) \quad (4-10)$$

This is general and can apply to capacitive or inductive reactance. To be able to compare and use these equations they are written in terms of one unknown at a time. From Equation (4-7)  $X$  as a function of  $R$  is:

$$X = \sqrt{RZ_0 - R^2} \quad (4-11)$$

So Equation (4-10) can be written as:

$$l = \frac{1}{\beta} \left(-\tan^{-1}\left(\frac{R}{\sqrt{RZ_0 - R^2}}\right)\right) \quad (4-12)$$

Equation (4-12) shows the length between the element and short circuit termination when the element is inductive. Equation (4-12) is shown in Figure (4-5).

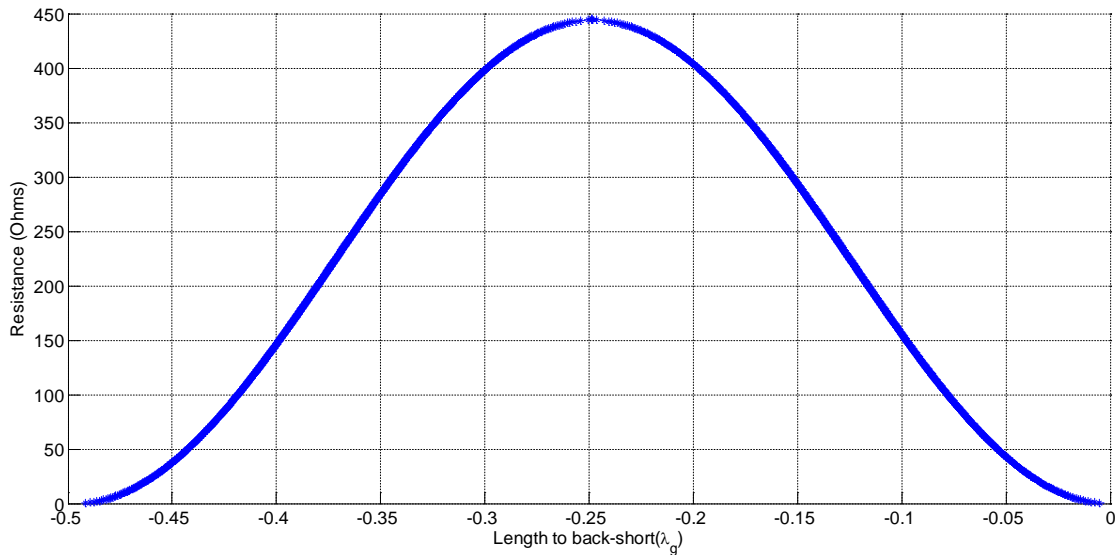


Figure 4-5 Length to short circuit termination versus R, using Equations (4-12);  $Z_0 = 444.08 \Omega$  ,  $\beta = 158.04$  and  $\lambda_g = 40 \text{ mm}$

Figure (4-5) shows the length to the short circuit termination for different values of element resistance and for the reflection coefficient to be zero. For a single value of resistance different lengths to termination are found that result in zero reflection coefficients.

It is not only required to find the resistance, but the detector must simultaneously have the appropriate value of reactance to give zero reflection. To be able to find the value of the reactance of an obstacle located at distance  $l$  from the short circuit termination, Equation (4-10) is written in terms of  $X$  by using Equation (4-7) to find  $R$  based on  $X$ .

$$R = \frac{Z_0 \pm \sqrt{Z_0^2 - 4X^2}}{2} \quad (4-13)$$

Substituting this in Equation (4-10) gives:

$$l = \frac{1}{\beta} \left( -\tan^{-1} \left( \frac{Z_0 \pm \sqrt{Z_0^2 - 4X^2}}{2X} \right) \right) \quad (4-14)$$

Equation (4-14) shows the length between the element and short circuit termination.

Equation (4-14) is plotted in Figure (4-6).

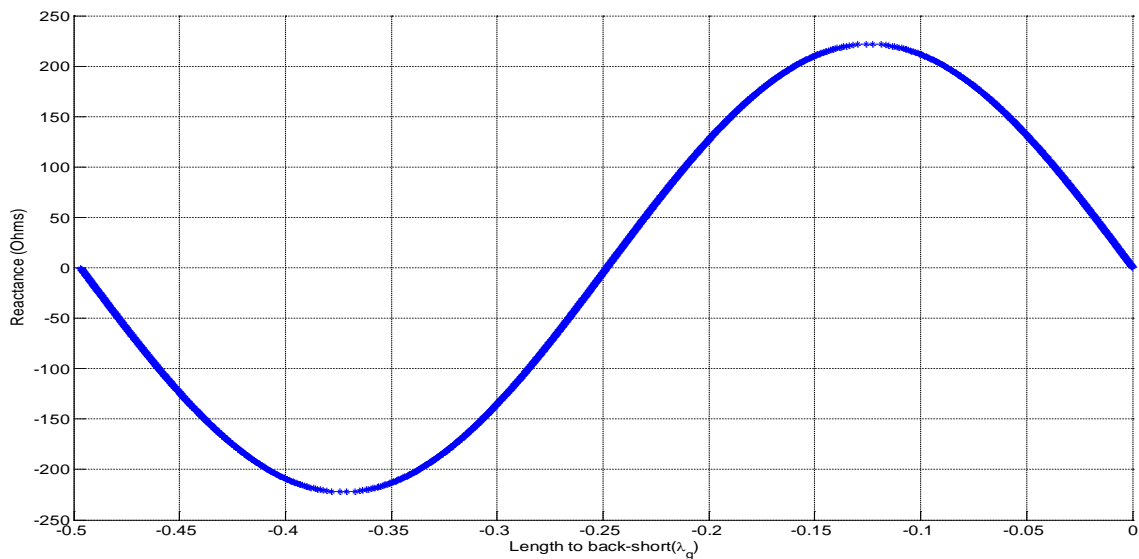


Figure 4-6 Length to short circuit termination versus reactance, using Equations (4-14);  $Z_0 = 444.08 \Omega$

and  $\lambda_g = 40 \text{ mm}$

Figure (4-6) shows the length to the short circuit termination for different values of element reactance, for which the reflection coefficient will be zero.  $X$  can be positive and inductive or negative and capacitive as shown in the figure.

For a certain value of reactance, different lengths between the element and termination are found. From Figure (4-6), for an inductive element two different lengths are found and for the capacitive element also another two lengths are found. Each pair of lengths, one is obtained from capacitive and one from inductive graphs, simultaneously yield a distinct resistance value to give zero reflection. These two resistance values are found from the diagram illustrated in Figure (4-5).

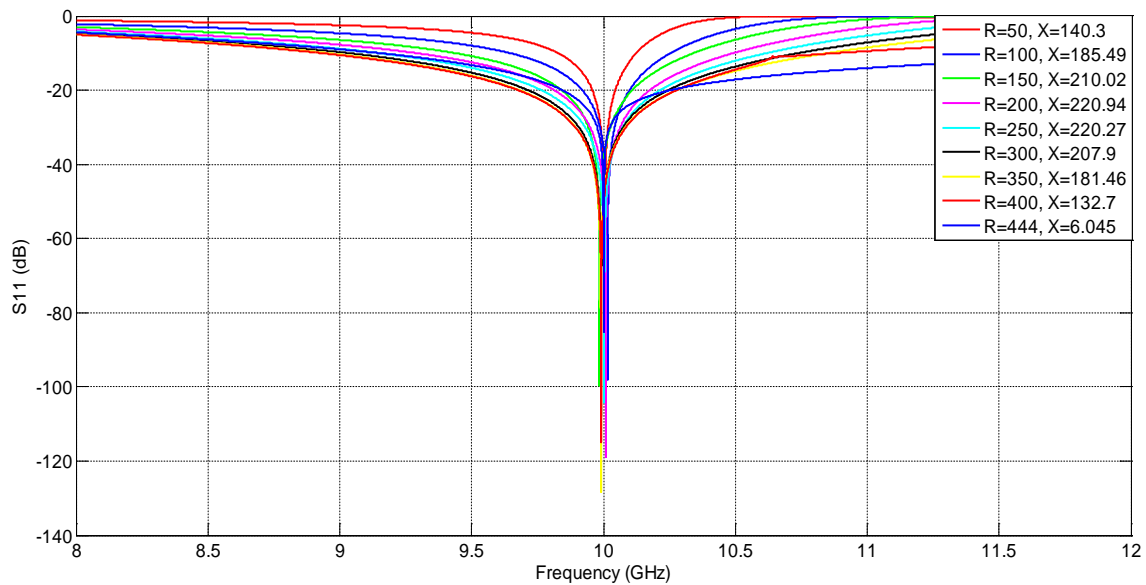


Figure 4-7 S<sub>11</sub> versus frequency for different R and X

Figure (4-7) shows the graph of  $S_{11}$  versus frequency of a resistive and inductive element located at specific lengths from the back short using Equations (4-14) and (4-12) to get zero reflection coefficients. There are a number of values for resistances and their corresponding reactance calculated to have a minimum reflection coefficient. They all have a minimum at centre frequency which is 10 GHz. The bandwidths ( $BW$ ) of these graphs are calculated from [35]

$$BW = \frac{(f_H - f_L)}{f_c} \quad (4-15)$$

Here  $f_H$  is the higher frequency of that band;  $f_L$  is the lower frequency of the band and  $f_c$  is the centre frequency. The lower and higher frequencies are taken at the -20 dB bandwidth levels and the values are plotted in Figure (4-7). The maximum bandwidth occurs at  $R \sim 380 \Omega$  but this is dependent upon the level in  $S_{11}$  where  $f_H$  and  $f_L$  are taken.

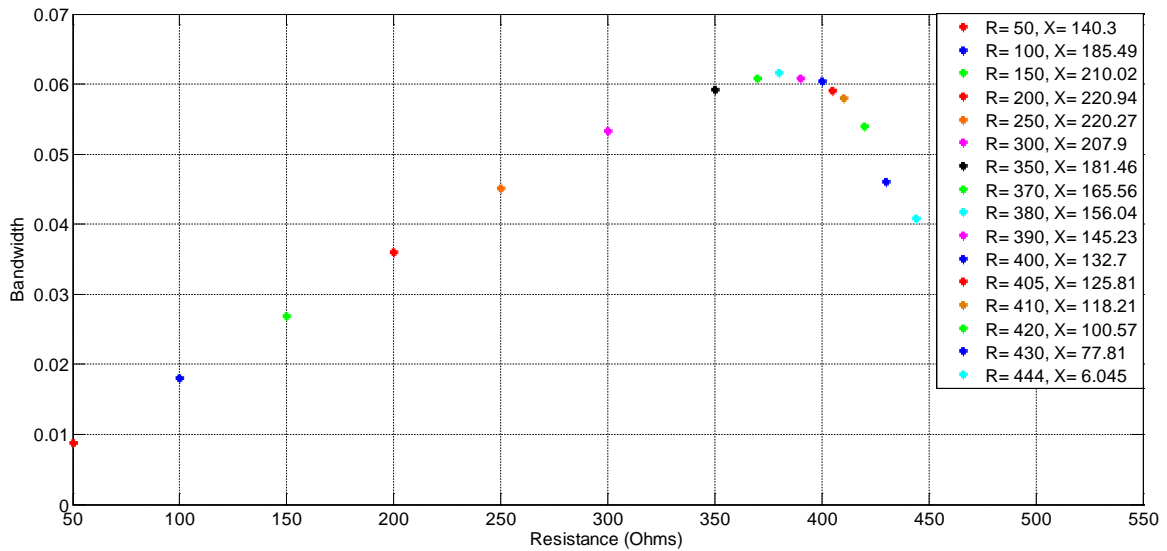


Figure 4-8 Resistance versus corresponding S11 bandwidth at -20 dB

Figure (4-8) shows that the maximum -20 dB bandwidth at frequency of 10 GHz is achieved when resistance is  $380 \Omega$  and reactance is  $156.04\Omega$ ; and it is about 6%.

### 4-3 Resistance of a post in waveguide

The above sections discuss generally any resistive and reactive element. Now moving on to look more specifically at a post, the DC resistance of a metal post can be calculated as:

$$R = \rho \frac{L}{A} \quad (4-16)$$

here  $\rho$  is the resistivity of material of the post,  $L$  is the length of the post and  $A$  is the area of the cross-section of the post [19].

If the cross section of the post is circular then the DC resistance can be calculated from:

$$R_{DC} = \frac{b}{\sigma \pi r^2} \quad (4-17)$$

where  $\sigma$  is the electrical conductivity of the material of the post;  $b$  is the length of the post and  $r$  is the radius of the post cross-section. Equations (4-16) and (4-17) show that resistance of the post depends on its size (radius and length) and also conductivity of the material from which it is made. In the high frequency case the resistance equation for the post is modified to consider the effect of the frequency-dependent skin depth.

$$R_{basic} = \frac{b}{\sigma(\pi r^2 - \pi(r - \delta)^2)} \quad (4-18)$$

Equation (4-18) is equivalent to Equation (4-17), only in that it is derived to operate in microwave frequencies where the skin depth matters and has to be considered. The

Figure (4-9) shows the cross section of the conductive post used to derive Equation (4-18), where the radius  $r$ , is much larger than the skin depth,  $\delta$ , i.e.  $r \gg \delta$ .

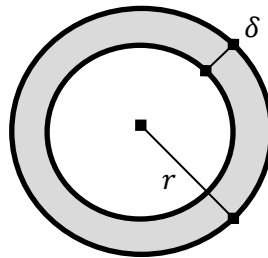


Figure 4-9 Cross-section of the post with skin depth  $\delta$  and radius  $r$

In order to plot Equation (4-18) we need to consider the skin depth. The current distribution varies as:

$$I = I_0 e^{-\frac{r}{\delta}} \quad (4-19)$$

Where  $I_0$  is the amplitude of the current at the surface and  $\delta$  is the skin depth and it is given by [34]:

$$\delta = \sqrt{\frac{2}{\mu\omega\sigma}} = \frac{1}{\sqrt{\pi f\mu\sigma}} \quad (4-20)$$

It is a function of conductivity and frequency. A graph of  $\frac{I}{I_0}$  versus depth of penetration  $r$  is plotted in Figure (4-10).

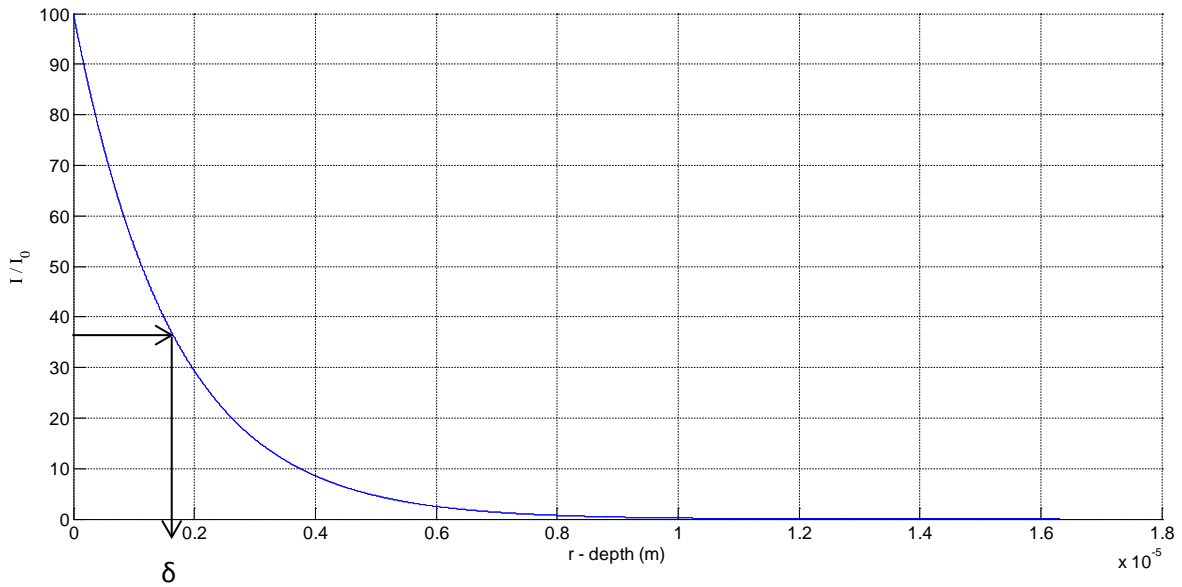


Figure 4-10- Figure of  $\frac{I}{I_0}$  versus penetration depth  $r$  at  $f = 10$  GHz

Figure (4-10) shows how the current varies as it penetrates the post. From the figure, when the current is at the surface of the post it is maximum and as it penetrates in the post it becomes smaller, until it penetrates within a thickness of a few skin depths where it has been almost completely attenuated.

For the case of DC, where  $f = 0$  Hz,  $\delta$  approaches infinity, this means that the depth in which the current will propagate in the conductor is limitless and can be taken as the radius; therefore the equation converges to Equation (4-17). Of course the equation is invalid if the skin depth becomes greater than the radius. On the other hand, as the frequency increases, the skin depth decreases and Equation (4-17) is valid [34].

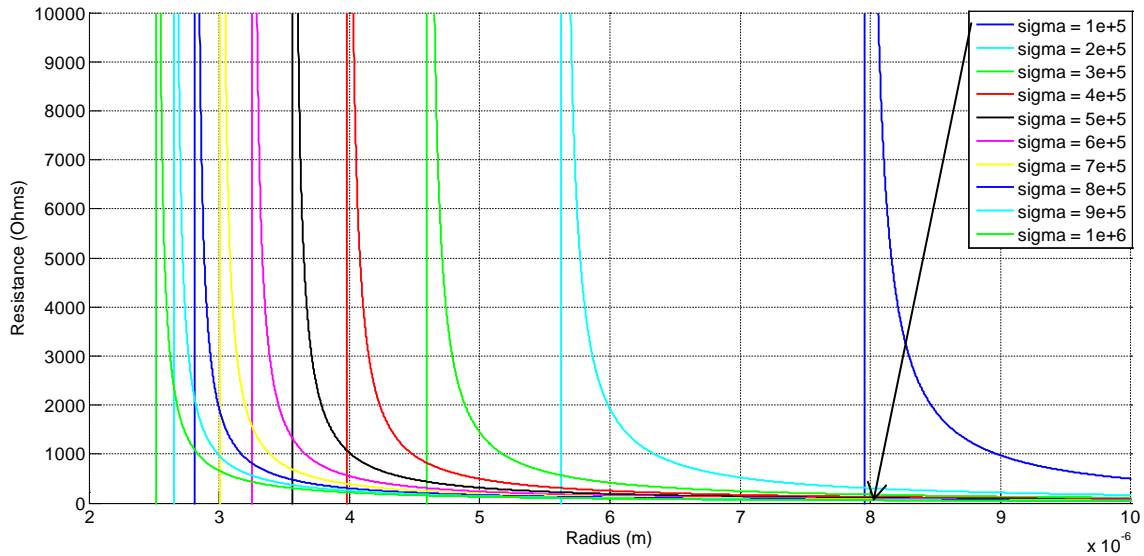


Figure 4-11 Resistance Equation (4-18) versus radius of the post

Figure (4-11) shows graphs of the post resistance Equation (4-18) when the post radius changes for different electrical conductivities ranging from  $\sigma = 10^{+5}$  to  $10^{+6} \text{ Sm}^{-1}$ . Looking from right to left it can be seen that as the radius decreases for each of the material's conductivity, at a certain radius the resistance of the post becomes large. This occurs when the denominator of Equation (4-18) approaches zero. That is:

$$\sigma(\pi r^2 - \pi(r - \delta)^2) = 0$$

$$r = \frac{\delta}{2}$$

As an example, the blue graph with  $\sigma = 1 \times 10^5 \text{ Sm}^{-1}$  is selected and the skin depth for that material is calculated from Equation (4-20) to be  $\delta = 1.59 \times 10^{-5} \text{ m}$  and radius is found.

$$r = \frac{\delta}{2} = 7.95 \mu\text{m}$$

Looking at the graph, the radius at which the resistance goes to  $\pm\infty$  at  $r = 7.95 \mu\text{m}$  is pointed too with an arrow on the graph. This is valid for all the other graphs for different electrical conductivities. Obviously this shows the limitation of this equation.

Another equation for resistance is found from [49] and it is the resistance of a round wire that is valid for any arbitrary frequency. It is derived using Bessel functions of the first kind [49].

$$R_{Bessel} = \frac{R_s}{\sqrt{2}\pi r} \left[ \frac{\text{ber } q \text{bei}' q - \text{bei } q \text{ber}' q}{(\text{ber}' q)^2 + (\text{bei}' q)^2} \right] \quad (4-21)$$

$R_s$  is the surface resistance, given in Equation (4-22);  $r$  is the radius of wire; ber and bei are Kelvin functions and they are the real and imaginary part of the first kind Bessel function, respectively. ber' and bei' are the derivatives of ber and bei functions. Also:

$$R_s = \frac{1}{\delta\sigma} \quad (4-22)$$

$$q = \frac{\sqrt{2}r}{\delta} \quad (4-23)$$

$q$  is a parameter, that is  $\sqrt{2}$  times of ratio of post radius to skin depth [49]. For high frequencies Equation (4-21) is reduced to [49]:

$$R_{High} = \frac{R_s}{2\pi r} \quad (4-24)$$

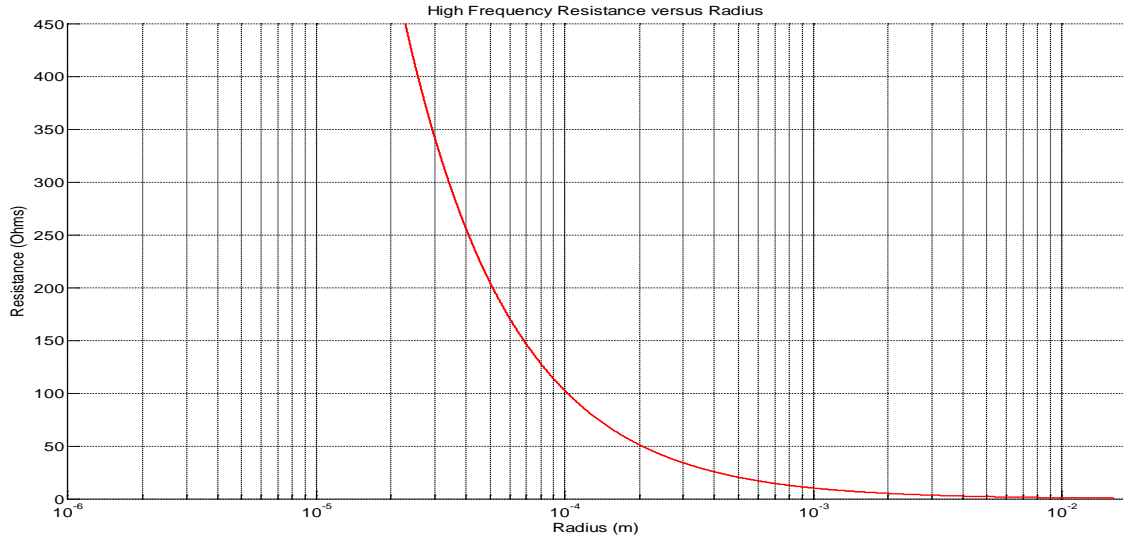


Figure 4-12 Resistance of post versus post radius, Equation (4-24),  $f=10$  GHz and  $\sigma = 9.52 \times 10^6 \text{ Sm}^{-1}$

Figure (4-12) shows the graph of resistance from Equation (4-24) for different values of the post radius. This equation is derived from Equation (4-21) and it is used to calculate the resistance of the post at high frequencies. The frequency of operation here is 10 GHz and the post is made of platinum ( $\sigma = 9.52 \times 10^6 \text{ Sm}^{-1}$ ). Only the range of resistances that are valid for the matched post are considered in the graph.

To calculate the post resistance at low frequencies, another equation is derived from Equation (4-21) which is provided below [49]:

$$R_{Low} = \frac{1}{\pi r^2 \sigma} \left[ 1 + \frac{1}{48} \left( \frac{r}{\delta} \right)^2 \right] \quad (4-25)$$

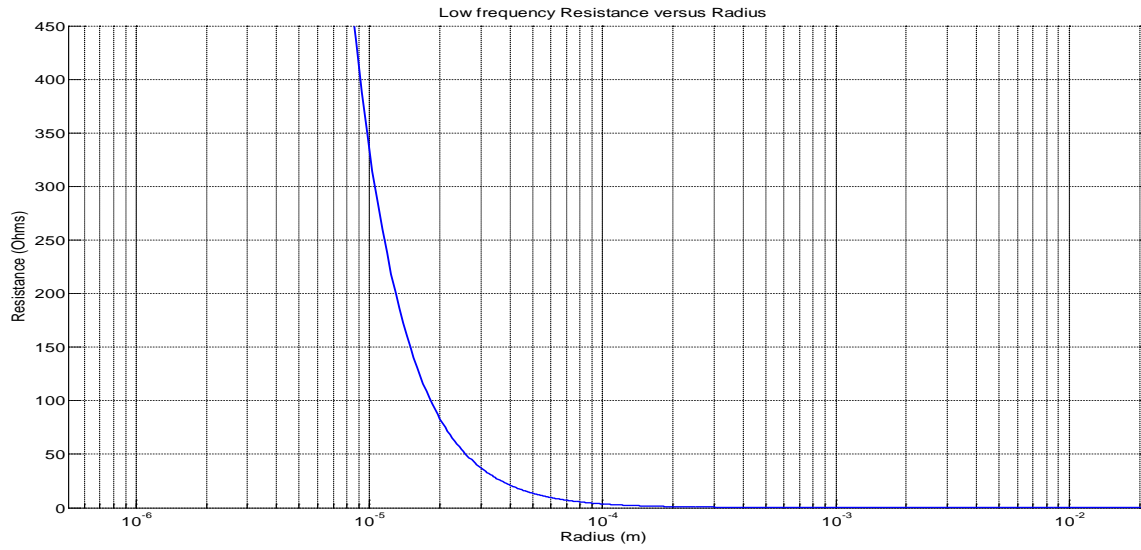


Figure 4-13 Resistance versus post radius- Equation (4-25),  $f= 10\text{GHz}$  and  $\sigma = 9.52 \times 10^6 \text{ Sm}^{-1}$

Figure (4-13) shows the graph of resistance using Equation (4-25) versus different values of post radius. Here only the range of resistances that are valid for the post with zero reflection coefficient are shown in the graph.

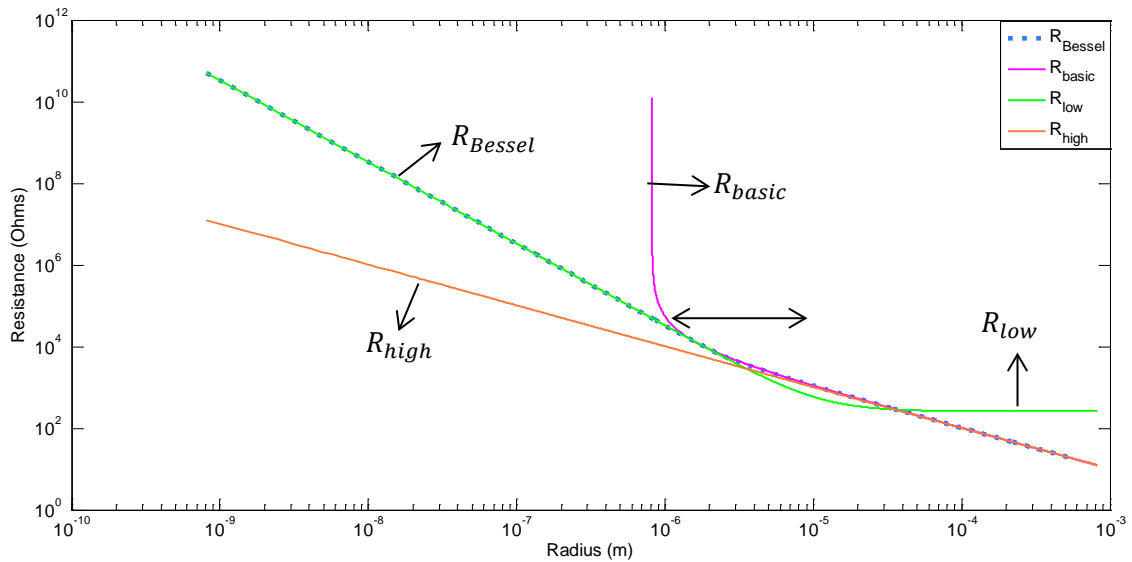


Figure 4-14 comparing different resistance equations, graph of resistance versus platinum ( $\sigma = 9.52 \times 10^6 \text{ Sm}^{-1}$ ) post radius at  $f= 10 \text{ GHz}$ , Equation (4-18),(4-21),(4-24),(4-25).

All the equations for calculating post resistance are plotted in Figure (4-14). As expected, it is shown that for smaller radiuses  $R_{Bessel}$  and  $R_{low}$  have the same values; whereas  $R_{high}$  is different. As the size of the radius increases the graph of  $R_{low}$ , Equation (4-25), starts to demerge from  $R_{Bessel}$ . At around the same radius when  $R_{low}$  demerges from  $R_{Bessel}$ ,  $R_{high}$  starts to merge to it.

Between the range of  $r = 10^{-6}$  and  $10^{-5}$  m, marked on the figure with a double arrow,  $R_{high}$  and  $R_{low}$  do not agree with  $R_{Bessel}$  anymore, which is the graph of the equation valid for any arbitrary frequency, but  $R_{basic}$  agrees with it. This shows that for radiuses larger than  $r = \delta/2$  Equation (4-18) is accurate and agrees with Equation (4-21).

#### 4-3-1 Comparing $R_{Basic}$ and $R_{High}$ (Equations (4-18) and (4-24))

When frequency and skin depth is constant and the size of the radius increases, or when the radius is constant and the frequency increases resulting in decreasing skin depth  $r \gg \delta$ , then in Equation (4-18), the term with  $\delta^2$  becomes very small and can be neglected compared to the other term which results in:

$$R_{Basic} = \frac{1}{2\sigma\pi r\delta} \quad (4-26)$$

This is equal to Equation (4-24),  $R_{high}$  that is derived for high frequencies. As can be seen in Figure (4-14), as the radius increases the magenta and orange graphs approach each other and

unite. Equation (4-18) seems to be more applicable than Equation (4-24) because it can be used for lower frequencies as well.

#### 4-3-2 Comparing $R_{Basic}$ and $R_{low}$ (Equations (4-18) and (4-25))

Equation (4-25) can be written as:

$$R_{low} = R_{DC} + \frac{1}{48\pi\sigma\delta^2} \quad (4-27)$$

It can be seen that for a constant radius as the skin depth increases  $r \ll \delta$  or the frequency decreases, then the second term approaches zero and only the DC terms remain as expected.

$$\frac{1}{48\pi\sigma\delta^2} \rightarrow 0$$

$$R_{low} = R_{DC}$$

Where  $R_{DC}$  is constant for a single radius; when the frequency decreases  $f \rightarrow 0$  then  $\delta \rightarrow \infty$  and  $R_{basic}$  will also approach  $R_{DC}$ .

For a constant frequency, as the post radius increases  $R_{low}$  decreases until the radius becomes large,  $r \gg \delta$ , then the DC part will be small and only the second term remains.

$$\frac{1}{\sigma\pi r^2} \rightarrow 0$$

$$R_{low1} \approx \frac{1}{48\pi\sigma\delta^2} \quad (4-28)$$

Meanwhile for the same characteristics, Equation (4-18) becomes Equation (4-26); so as the radius increases, Equation (4-18) also decreases. It is concluded that when  $r = 24\delta$ ,  $R = R_{low1}$ .

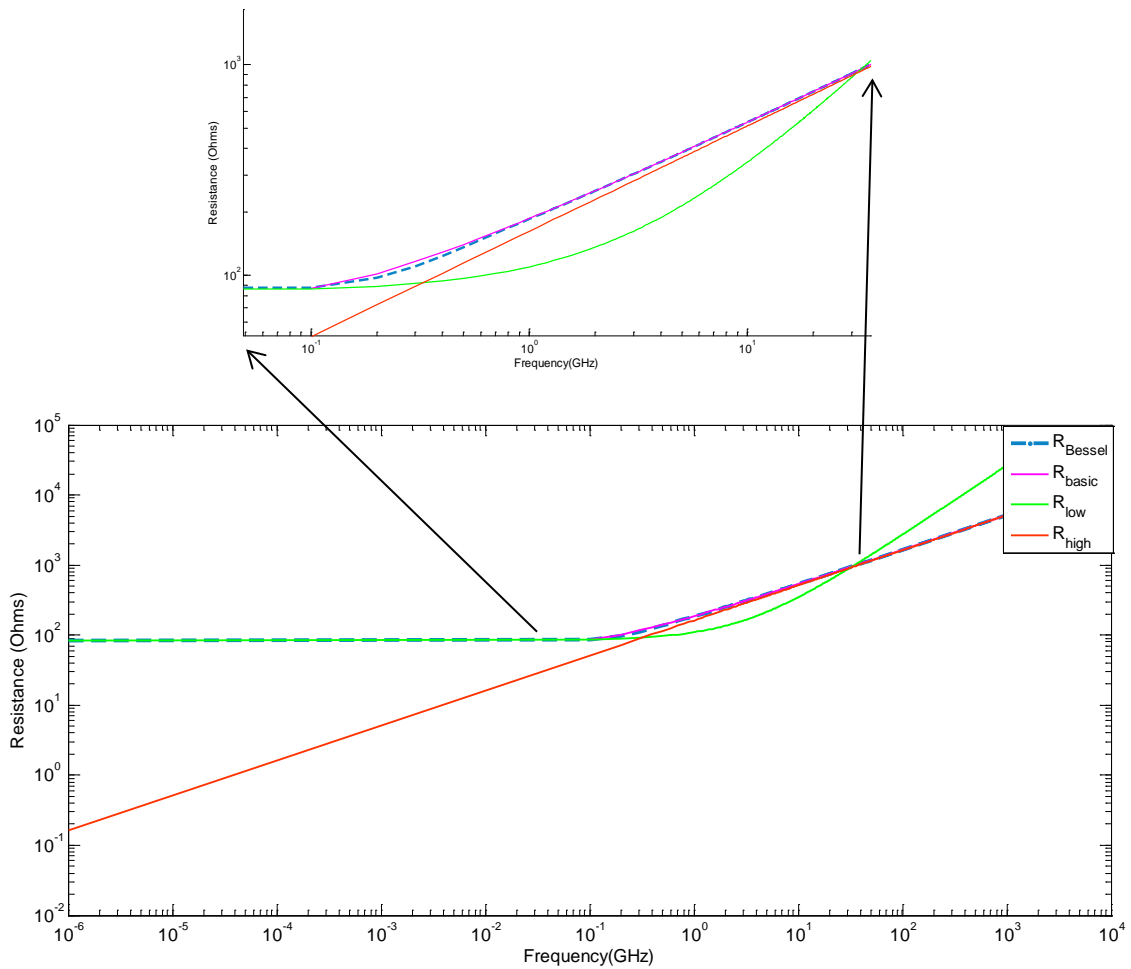


Figure 4-15 Resistance versus frequency for a platinum post with radius = 20  $\mu\text{m}$ , Equations (4-18),( 4-21), (4-24) and (4-25)

Figure (4-15) shows the behaviour of different resistance equations for a platinum post with a constant radius, when the frequency of operation changes. As the frequency increases the skin depth decreases; therefore looking at the equations the resistance values are also increasing. Graphs of Equations (4-25) and (4-21) are almost the same from 100 Hz up to about 0.1 GHz. The graph of Equation (4-18) for this specific radius only starts from 0.01 GHz and approaches the graph of Equation (4-21) and at about 1 GHz they almost unite. As the frequency becomes larger the graph of Equation (4-21) approaches the graph of Equation (4-24), which had very different values for lower frequencies.

The resistance graphs in the range of frequencies between 0.1 GHz to 100 GHz are zoomed in. It can be seen that in this range the first graph of  $R_{high}$  starts to merge with the graphs of  $R_{basic}$  and  $R_{Bessel}$  as expected and the graph of  $R_{low}$  which had same values as  $R_{Bessel}$  starts to have different values. Meanwhile the graph of  $R_{basic}$  remains equal to  $R_{Bessel}$ .

From Figures (4-15) and (4-16), it can be concluded that Equation (4-18) is more reliable for a larger range of frequency and larger range of radiuses than  $R_{high}$  and  $R_{low}$  alone and it is much simpler than  $R_{Bessel}$ .

### 4-3-3 Resistance versus $\frac{r}{\delta}$

Finally we will now compare the normalised resistance when they are all written in terms of  $\frac{r}{\delta}$  and divided by  $R_{DC}$ ; Assuming  $\frac{r}{\delta} = r'$ .

Dividing Equation (4-18) by the DC resistance, Equation (4-17) in terms of 'r' can be written as follows:

$$\frac{R}{R_{DC}} \cong \frac{r^2}{\delta^2} \frac{1}{\left(2\frac{r}{\delta} - 1\right)} = \frac{r'^2}{2r' - 1} \quad (4-29)$$

Dividing Equation (4-24) by the DC resistance, Equation (4-17) in terms of 'r' can be written as follows:

$$\frac{R_{High}}{R_{DC}} \cong \frac{r}{2\delta} = \frac{r'}{2} \quad (4-30)$$

Dividing Equation (4-25) by the DC resistance, Equation (4-17) in terms of 'r' can be written as follows:

$$\frac{R_{Low}}{R_{DC}} \cong 1 + \frac{r^2}{48\delta^2} = 1 + \frac{r'^2}{48} \quad (4-31)$$

In Equation (4-21),  $q$  can be rewritten in terms of  $r$ .

$$q = \frac{\sqrt{2}r}{\delta} = \sqrt{2}r'$$

The equation cannot be normalised with respect to the DC resistance and so is not included in the rest of this section.

These normalised equations are plotted in Figure (4-16).

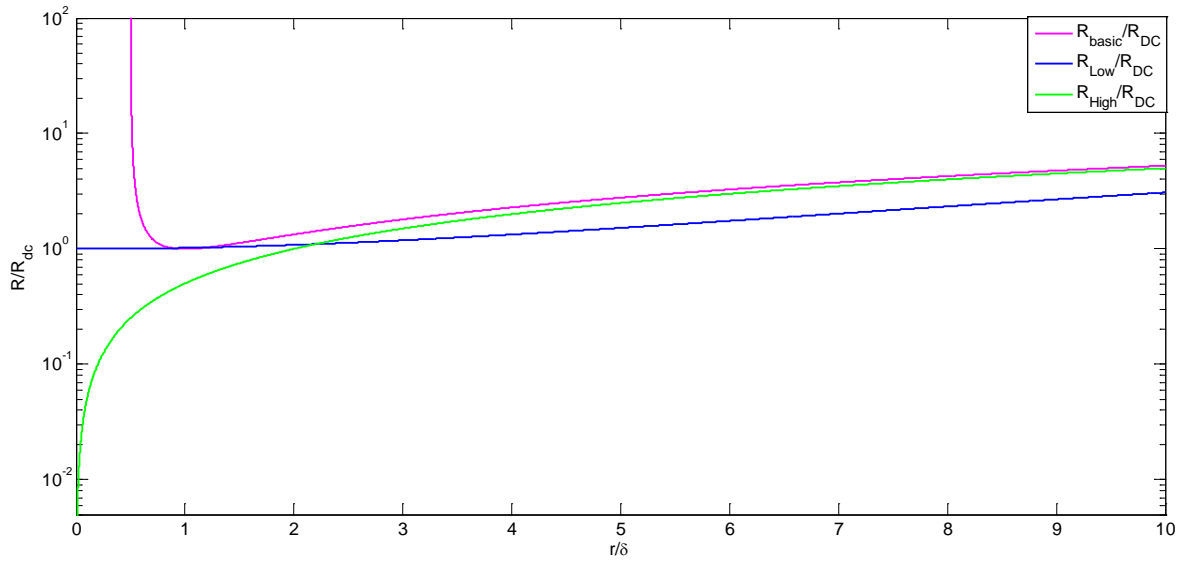


Figure 4-16 Resistance equations divided by Equation (4-17) versus  $\frac{r}{\delta}$

Figure (4-16) shows the behaviour of the normalised Equations (4-29), (4-30), (4-31) independent of the effects of frequency. For large  $\frac{r}{\delta}$  or when the skin depth is shallow, as expected the green graph  $R_{high}$  approaches the normalized  $R_{basic}$  graph and at low frequencies and large skin depth, for a very small range of  $\frac{r}{\delta}$  values, the blue graph  $R_{Low}$  has very close values to the magenta graph,  $R_{basic}$ .

From the above discussion, it is possible to find a suitable equation for the resistance of the post. This can then be chosen to give an appropriate value for having a zero reflection coefficient in the power sensor described earlier. However, the reactance is also needed and this is discussed in the next section.

#### 4-4 Reactance of a post in waveguide

An equation for the reactance of a post with radius  $r$  in a waveguide is provided in [47] [50]

$$X_{post} = Z_0 \frac{a [\ln(\frac{2a}{\pi r}) - 2]}{-2j\lambda_g} = jZ_0 \frac{a [\ln(\frac{2a}{\pi r}) - 2]}{2\lambda_g} \quad (4-32)$$

Equation (4-32) represents the reactance of an inductive post and it is dependent on characteristic impedance of the waveguide;  $a$  is the width of the waveguide and  $\lambda_g$  is the guided wavelength.

The graph of  $X_{post}$  against the changes in radius  $r$  is plotted in Figure (4-17). In this figure for post radiuses larger than 2 mm, the value of the reactance becomes negative and the equation becomes invalid for radiuses approaching this value. This should be kept in mind and the equation should be used only for post radiuses smaller than 2 mm for the X-band waveguide. From Figure (4-6) it is understood that the suitable range of reactance values is between 0 to 222  $\Omega$  for the power sensor. Only the post radiuses in this range of reactance are shown in Figure (4-17). So from the graph, it is evident that to get a valid value for the reactance, the radius of the post should be in range of about 0.3 mm ( $\sim 222 \Omega$ ) to almost 2 mm ( $\sim 0 \Omega$ ).

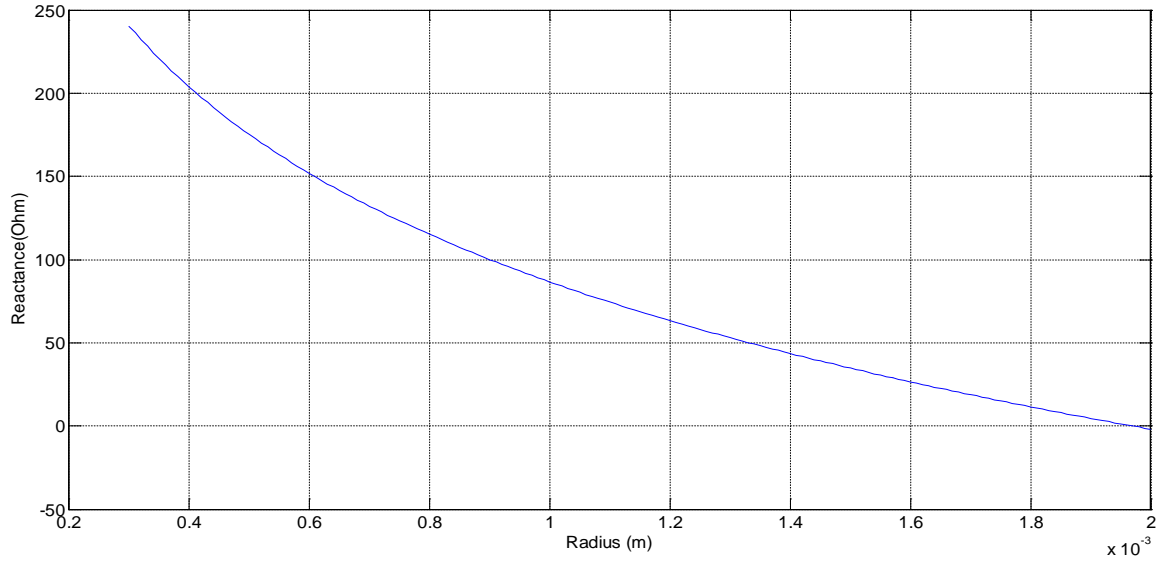


Figure 4-17 Post reactance Equation (4-32) versus post radius, X band waveguide;  $a = 22.86$  mm,

$$b = 10.16 \text{ mm}, \lambda_g = 40 \text{ mm} \text{ and } Z_0 = 444.08 \Omega$$

Equations from Potok [50], Montgomery [19] and from Lancaster [47] are the same which is equal to Equation (4-32). Equations from Bianchi [51] and Marcuvitz [52] are more involved and are discussed below.

The normalized reactance of a post from Bianchi [51] is:

$$X_{Bianchi} = \left[ \frac{4\pi}{\beta a} \left[ \ln \left( \frac{a}{\pi r} \right) - 1 + 2 \left( \frac{a}{\pi r} \right)^2 \sum_{n=3,5,\dots}^{\infty} \left( \frac{\pi}{a\gamma_n} - \frac{1}{n} \right) \sin^2 \left( \frac{n\pi r}{a} \right) \right]^{-1} \right]^{-1} \quad (4-33)$$

In Equation (4-33)  $r$  is the radius of the post;  $\beta$  is the propagation constant;  $a$  is the width of the waveguide and  $\gamma_n$  is given by

$$\gamma_n = \sqrt{\left(\frac{n\pi}{a}\right)^2 - \omega^2 \varepsilon \mu} \quad (4-34)$$

$\omega$  is the angular frequency of operation;  $\varepsilon$  is permittivity the of the material;  $\mu$  is the permeability of the material.

In addition the equation of normalized inductance of the post from Marcuvitz [52] is:

$$X_{Marcuvitz} = Z_0 \left( \frac{a}{2\lambda_g} \left[ S_0 - \left(\frac{\pi d}{2\lambda}\right)^2 - \frac{5}{8} \left(\frac{\pi d}{2\lambda}\right)^4 - 2 \left(\frac{\pi d}{2\lambda}\right)^4 \left( S_2 - 2S_0 \frac{\lambda^2}{\lambda_g^2} \right)^2 \right] + \frac{X_b}{2Z_0} \right) \quad (4-35)$$

Where  $d$  is the diameter of the post;  $\lambda$  is the wavelength;  $\lambda_g$  is the guided wavelength;  $a$  is the width of the waveguide and

$$\frac{X_b}{Z_0} = \frac{a}{\lambda_g} \frac{\left(\frac{\pi d}{a}\right)^2}{1 + \frac{1}{2} \left(\frac{\pi d}{\lambda}\right)^2 \left(S_2 + \frac{3}{4}\right)} \quad (4-36)$$

$$\frac{X_b}{Z_0} \approx \frac{a}{\lambda_g} \frac{\left(\frac{\pi d}{a}\right)^2}{1 + \frac{11}{24} \left(\frac{\pi d}{\lambda}\right)^2} \quad (4-37)$$

$$S_0 = \ln \frac{4a}{\pi d} - 2 + 2 \sum_{n=3,5,\dots}^{\infty} \left[ \frac{1}{\sqrt{n^2 - \left(\frac{2a}{\lambda}\right)^2}} - \frac{1}{n} \right] \quad (4-38)$$

$$S_2 = \ln \frac{4a}{\pi d} - \frac{5}{2} + \frac{11}{3} \left(\frac{\lambda}{2a}\right)^2 - \left(\frac{\lambda}{a}\right)^2 \sum_{n=3,5,\dots}^{\infty} \left[ \sqrt{n^2 - \left(\frac{2a}{\lambda}\right)^2} - n + \frac{2}{n} \left(\frac{a}{\lambda}\right)^2 \right] \quad (4-39)$$

Equations (4-32) to (4-35) for post reactance are plotted and compared in figure (4-18).

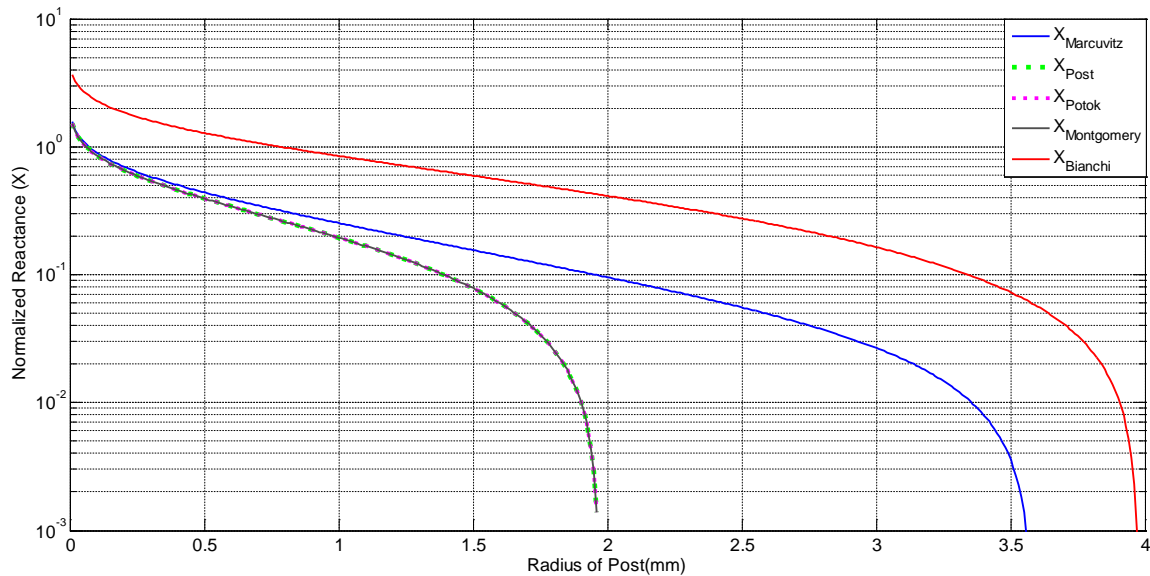


Figure 4-18 Normalized reactance equations versus radius of the post at  $f = 10$  GHz, X band waveguide;

$$a = 22.86 \text{ mm}, b = 10.16 \text{ mm}, \lambda_g = 40 \text{ mm} \text{ and } Z_0 = 444.08 \Omega$$

Figure (4-18) shows the graph of different normalized reactance equations at  $f = 10$  GHz. They are independent of the electrical conductivity of the material. Each of the equations covers a range of post radiuses but three of them become negative for radiuses larger than 2 mm and Equations (4-33) and (4-35) become negative for radiuses larger than 4 mm. Since three out of these five equations from different sources are identical, it seems more convincing to proceed, using them.

## 4-5 Impedance of the post in waveguide

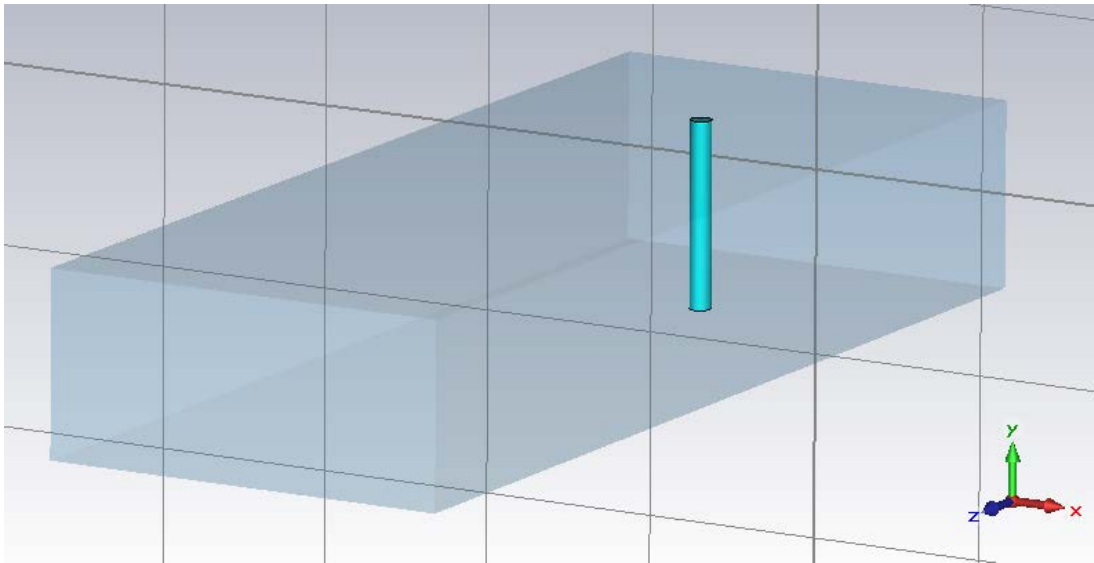


Figure 4-19 The WR90 waveguide structure with inductive post – designed in CST microwave Studio by student

Figure (4-19) shows the structure of a short circuited WR90 waveguide with an inductive post located at specific distance to the termination. Now for a post that is equivalent to a resistance in series with inductance, the impedance is determined using the resistance equation as the real part and the inductance for the imaginary part, as given below:

$$Z_{post} = \frac{b}{\sigma(\pi r^2 - \pi(r - \delta)^2)} + jZ_0 \frac{a \times [\ln\left(\frac{2a}{\pi r}\right) - 2]}{2\lambda_g} \quad (4-40)$$

From the Equation (4-40), both the resistance and inductance are a function of frequency and radius. The real part of  $Z_{post}$  is Equation (4-18) and the imaginary part is Equation (4-32). For the power sensor, there is only a specific range of radiuses that will result in the suitable value for reactance and resistance as described above.

In Figure (4-8), it was found that the bandwidth for  $R=380 \Omega$  is the widest at  $f = 10$  GHz along with having zero reflection; therefore it is considered here as it gives the best result.

For  $R= 380 \Omega$ , from Equation (4-11) reactance is calculated to be  $X = 156.04 \Omega$  and from Equation (4-32) the radius is found to be  $r = 0.581$  mm. From Equation (4-12) the length to back-short is found to be  $l = 7.4$  mm. Using these values and Equation (4-18) and considering the X-band waveguide, the specific conductivity of  $\sigma = 33.41$  (S/m) is calculated for the post at  $f = 10$  GHz.

These values provide zero reflection coefficient from the analytical theory described above. To check this theory a post in a waveguide is simulated using full-wave simulation software. Figure (4-20) shows the graph of  $S_{11}$  versus frequency for a post located at the calculated distance to the short circuit termination of an X-band waveguide, simulated with CST microwave Studio software [28]. All the parameters used for this design are those described in previous paragraph.

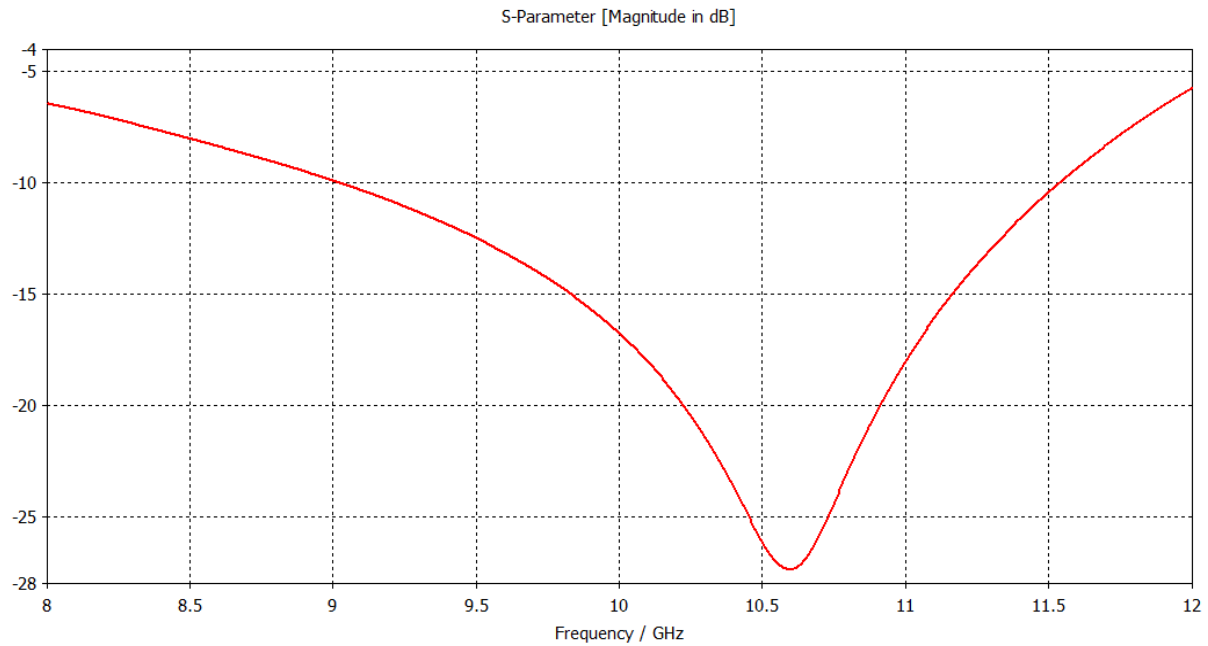


Figure 4-20 graph of  $S_{11}$  versus frequency for X band waveguide;  $a = 22.86$  mm,  $b = 10.16$  mm,  $\lambda_g = 40$  mm and  $Z_0 = 444.08 \Omega$  with post with  $r = 0.581$  mm and  $\sigma = 33.41$  S/m located at  $l = 7.4$  mm to the termination produced by CST Microwave Studio

As can be seen a good response with low  $S_{11}$  is achieved; a return loss of 27 dB at  $f=10.5$  GHz and about -16 dB at  $f=10$  GHz, which is the frequency of operation.

In order to get a better result at  $f=10$  GHz, optimization is used and the result is shown in Figure (4-21). The size of the radius and position of the post in the waveguide are altered slightly to achieve a dip closer to  $f = 10$  GHz, resulting in  $S_{11}$  of -41 dB just above  $f=10$  GHz.

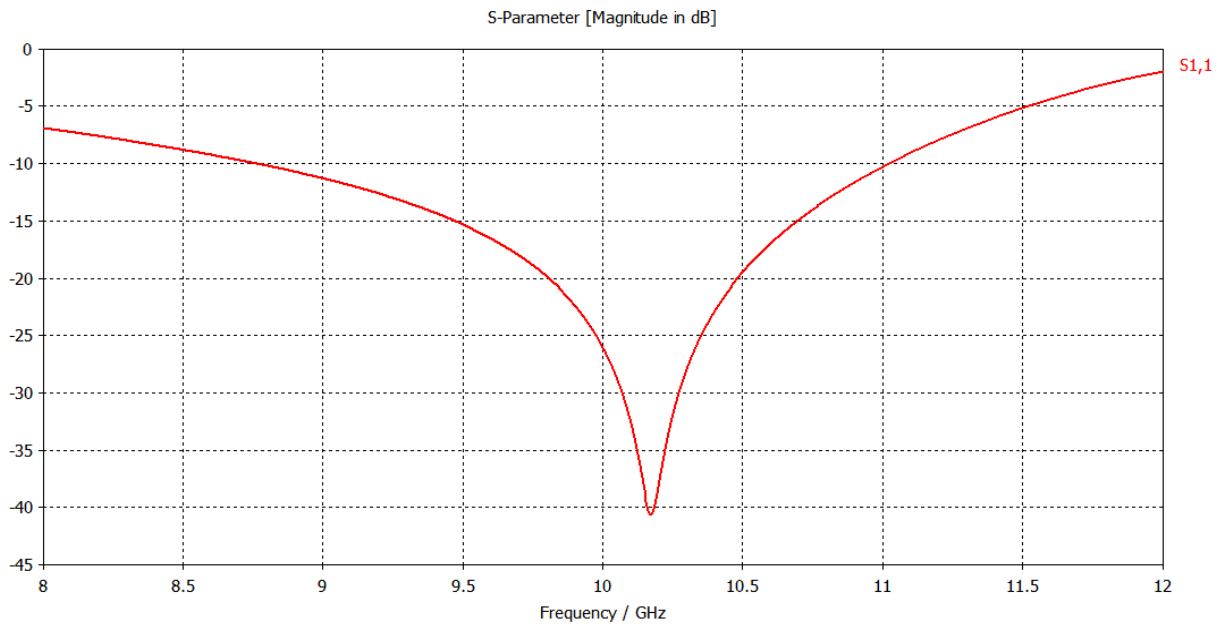


Figure 4-21 optimized S11 versus frequency for X band waveguide;  $a = 22.86 \text{ mm}$ ,  $b = 10.16 \text{ mm}$ ,  $\lambda_g = 40 \text{ mm}$  and  $Z_0 = 444.08 \Omega$  with a post with a radius  $r = 0.581 \text{ mm}$  and  $\sigma = 33.41 \text{ S/m}$  located at  $l = 8 \text{ mm}$  to the termination

Of course this post can not be easily made as the conductivity of the material is not met by a common material. However, this chapter fully confirms the analytic theory with a numerical example. For further interest Figure (4-22) shows the power flow in the waveguide.

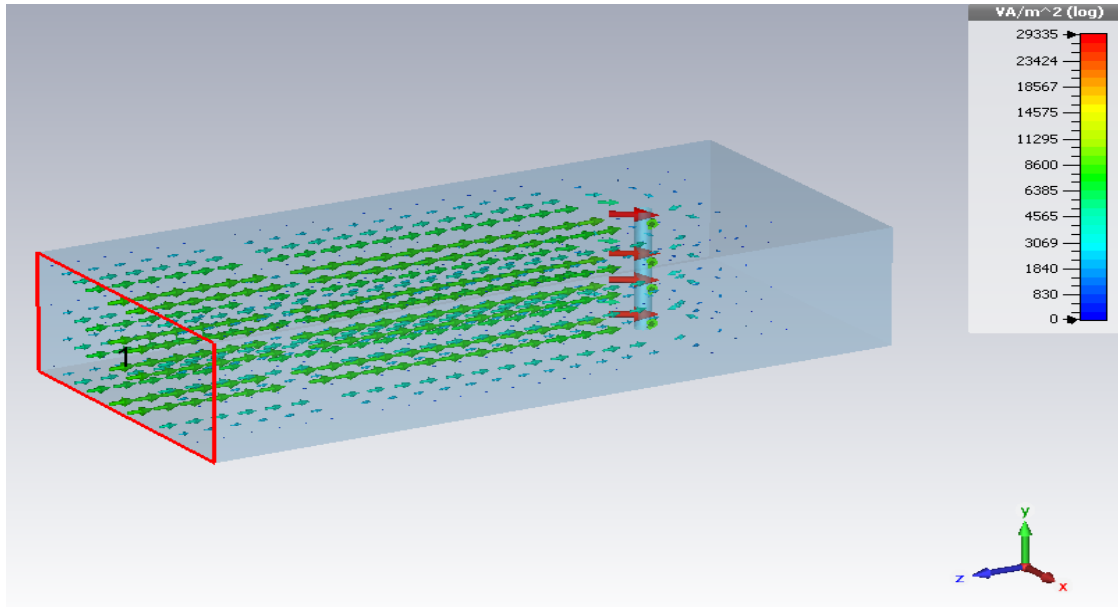


Figure 4-22 Power flow in X band waveguide;  $a = 22.86 \text{ mm}$ ,  $b = 10.16 \text{ mm}$ ,  $\lambda_g = 40 \text{ mm}$  and  $Z_0 = 444.08 \Omega$  with a post with radius  $r = 0.581 \text{ mm}$  and  $\sigma = 33.41 \text{ S/m}$  located at  $l = 8 \text{ mm}$  to the termination.

As can be seen the arrows showing the power flow have almost stopped as they have reached the post. This shows that the power is absorbed by the post and therefore it doesn't go any further.

## CHAPTER 5- THIN FILM BOLOMETER

In this chapter a thin film is used as the power sensor in the design of a power detector. The thin film is useful as it can be used up to millimetre wave frequencies in convenient integrated designs. Initially a paper by Lane and Evans [29] is followed in this chapter for the design of a thin film power detector and the results in the paper are simulated and verified. After the design technique is examined and understood, a similar method is used to design a power detector with a platinum film element.

### 5-1 Thin film bolometer

In this section a thin film power detector is designed using the transmission line theory explained in Chapter 3 and some of the matching calculations discussed in Chapter 4. The aim is to design a power detector with a simple platinum thin film, located at distance  $l$  to the short circuit termination, connected to the broad walls of the X-band waveguide as shown in Figure (5-1).

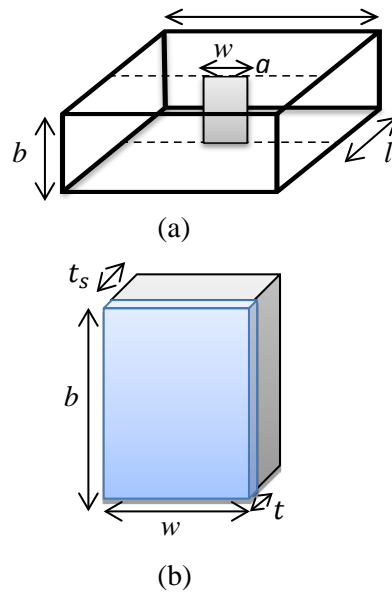


Figure 5-1 (a) The rectangular waveguide with thin film located at distance  $l$  to termination, (b) The thin film structure consisting of the thinner metal film on thicker glass substrate.

Figure (5-1a) shows the structure of thin film in the X-band waveguide and Figure (5-1b) shows the thin film element from a closer perspective. It consists of the conductive film shown in blue with small thickness ( $t$ ) attached to the substrate shown in grey, of almost the same size with a larger thickness ( $t_s$ ).

The approach taken here is to follow the paper by Lane and Evans [29]; since this paper has designed a very similar power detector and used the same method of matching that is used in Chapter 4 for our post element. The attempt is to understand and check the theory they have used and to repeat their calculation in order to confirm their results. Later the structure will be simulated. Most of the values and steps they have taken are described in the paper, but some of the parameters such as the film thickness are not given, so the calculations are done here to

get the estimated values before carrying out a simulation in CST microwave Studio. Most of the equations are the same as those used in Chapter 4 and they have been repeated here for convenience.

Similar to the post element in Chapter 4, the impedance of the thin film element has also a resistive part and a reactive part.

$$Z_{Film} = R + jX \quad (5-1)$$

Considering the thin film in the short circuited waveguide, the input impedance can be calculated from:

$$Z_{in} = \frac{(R + jX)jX_{sc}}{R + jX + jX_{sc}} \quad (5-2)$$

Equation (5-2) is the input impedance looking from where the film is located;  $R$  is the resistance of the film and  $X$  is the reactance;  $X_{sc}$  is the equivalent reactance of the short circuit line and it is given below:

$$X_{sc} = Z_0 \tan \beta l \quad (5-3)$$

Equation (5-2) is then divided into a real part and an imaginary part. To have a matched circuit, the real part is equivalent to the characteristic impedance of the waveguide and gives

$$Z_0 = \frac{R^2 + X^2}{R} \quad (5-4)$$

The imaginary part has to be cancelled and making it equivalent to zero, gives:

$$X_{sc} = \frac{-(R^2 + X^2)}{X} \quad (5-5)$$

Considering Equations (5-3), (5-4) and (5-5), the relationship given below can be derived.

$$\tan\left(\frac{2\pi l}{\lambda_g}\right) = \frac{-R}{X} \quad (5-6)$$

From this equation the separation distance between the film and short circuit termination can be calculated or in the case of Lane and Evans measured experimentally [29].

The short circuit termination of the waveguide is highly conductive providing a low loss short across the waveguide. In Lane and Evans' work the film resistance is of the order of the waveguide impedance, so the separation distance between the thin film and terminations will be an odd multiple of quarter wavelength at the operating frequency [53].

Furthermore, in Lane and Evans' work, the material of the film element is nichrome ( $\sigma = 9.09 \times 10^5$  S/m) deposited on a glass strip of 0.012 cm thickness and 0.4 cm width and with the height the same as the waveguide. The thickness of the metallic film is not specified directly in the paper, only that it is in the order of nano metres.

Two different cases are considered in this paper [29]; one tunable bolometer and one pretuned.

### 5-1-1 First case

In the first case the position of the film bolometer is tuneable. The length between the film and the short circuit termination of the waveguide is adjusted and measured experimentally. The width of the nichrome film is given as 0.397 cm. The tuneable bolometer functions between 8.5-10 GHz and the optimum VSWR close to 1 is achieved at  $f = 8.55$  GHz. The film resistance that results in matching is calculated using the equation for DC resistance of metallic film and it is given as

$$R = R_{DC} = \rho \frac{L}{A} = \frac{\rho l}{tw} \quad (5-7)$$

From Equation (5-7)  $R = 509 \Omega$  and from this result we can calculate the thickness of the thin film to be  $t = 5.53$  nm. The distance between the thin film and short circuit termination after tuning is  $\frac{l}{\lambda_g} = 0.272$ ; that is a distance of  $l = 14.9$  mm, which is slightly greater than a quarter of the guided wavelength (13.7 mm). The reactance must also be considered and is given by:

$$X = \frac{-R}{\tan\left(\frac{2\pi l}{\lambda_g}\right)} \quad (5-8)$$

Lane and Evans have used Equation (5-8) to calculate the inductive reactance. This is dependent on the value of the length to back short which was found experimentally previously;  $X$  is calculated experimentally here to be  $X = 71 \Omega$ .

For a rectangular waveguide with TE<sub>10</sub> mode, the characteristic impedance is given by Equation (3-25) and reproduced below:

$$Z_{wv} = \frac{2b}{a} \frac{377\lambda_g}{\lambda} \quad (5-9)$$

From Equation (5-4), characteristic impedance is measured experimentally to be  $Z_0 = 519 \Omega$ , but using the theoretical Equation (5-9), it will be  $521 \Omega$ , which is almost the same.

Now the VSWR can be calculated based on Lane and Evans' data using the equation for reflection coefficient (Equation (3-7)) and Equation (3-9) and using:

$$VSWR = \frac{1 + |\Gamma|}{1 - |\Gamma|} \quad (5-10)$$

Using the VSWR it is possible to compare directly the Lane and Evans' result with our calculations as their paper gives a graph of VSWR versus frequency. All the parameters used to make this design are tabulated in Table (5-1).

Table 5-1 Parameters of design for thin nichrome film on glass substrate to operate at  $f = 8.55$  GHz in X-band waveguide

Parameter	Value	Parameter	Value
Film height	10.16 mm	Length to back-short	14.9 mm
Film thickness	5.53 nm	Guided wavelength	54.7 mm
Film width	3.97 mm	Film conductivity	9.09 e+5 S/m
Substrate height	10.16 mm	Film resistivity	1.10 e-6 $\Omega$ .m
Substrate thickness	0.12 mm	Substrate resistivity	1e+11 $\Omega$ .m
Substrate width	4 mm	Skin depth	5.70 $\mu$ m
Characteristic impedance	519 $\Omega$		

Figure (5-2) shows the graph of VSWR versus frequency that is derived using the given equations and the parameter values of Lane and Evans, as discussed above. As expected at  $f = 8.55$  GHz, a VSWR of almost 1 is achieved.

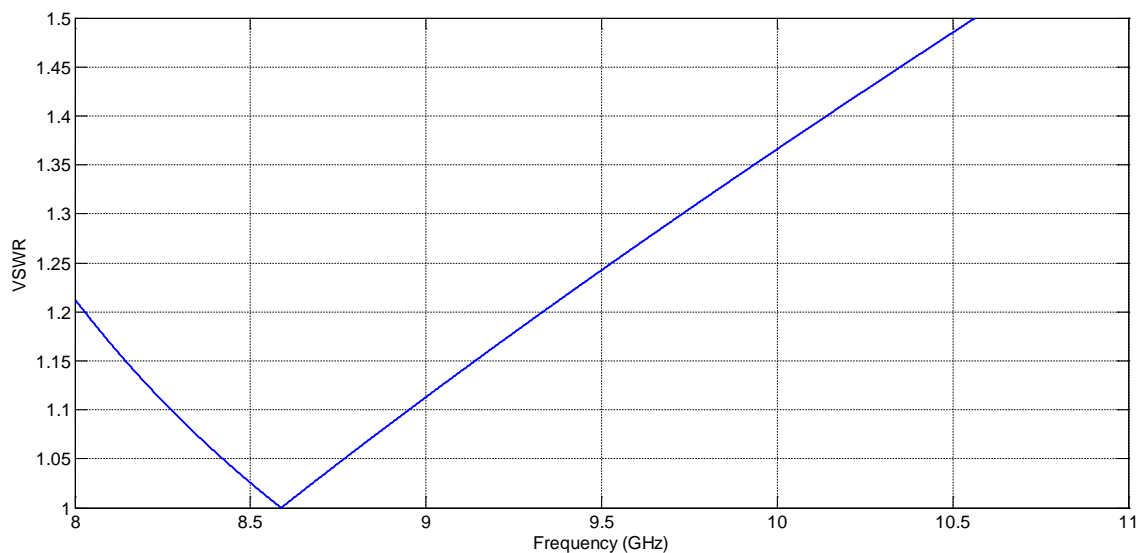


Figure 5-2 VSWR versus frequency for X band waveguide with nichrome film on the glass substrate- design parameters are given in Table (5-1)

The same parameter values in Table (5-1) are used to design the structure in CST Microwave STUDIO simulation software to see if the results are compatible.

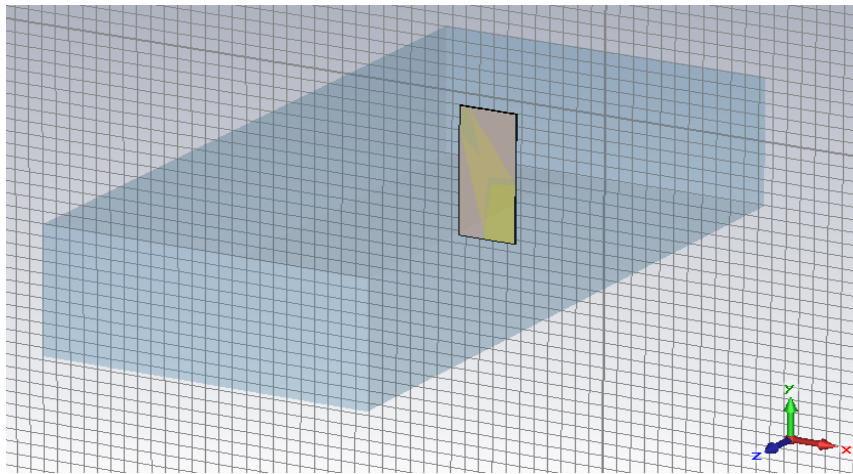


Figure 5-3 The WR90 waveguide structure with inductive thin film – Designed in CST MICROWAVE STUDIO

Figure (5-3) shows the structure of the WR90 waveguide with the film element used in CST MICROWAVE STUDIO. All the design parameters are given in Table (5-1).

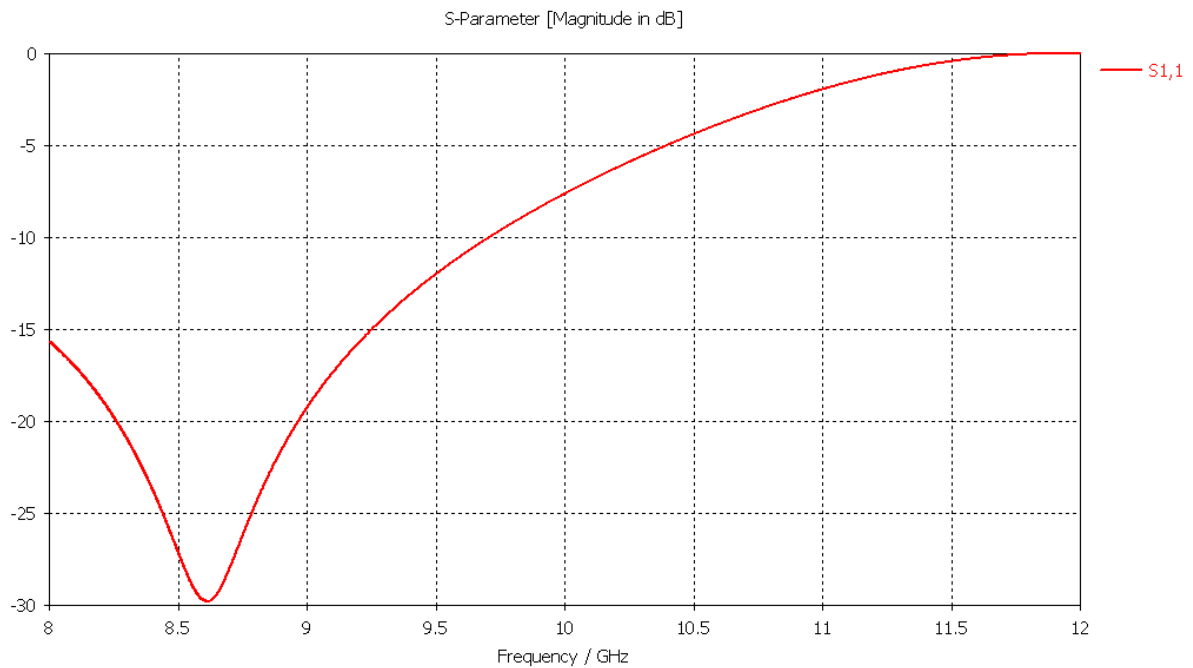


Figure 5-4 S11 versus frequency for X band waveguide with nichrome film on the glass substrate- design parameters are given in Table (5-1)

Figure (5-4) shows the  $S_{11}$  graph for the designed structure. It is important to remember that the structure is designed based on the information given in Lane and Evans' paper as described previously [29]. As expected the  $S_{11}$  value is lowest at  $f = 8.55$  GHz where the film size and location have been adjusted to have maximum absorption at this frequency.

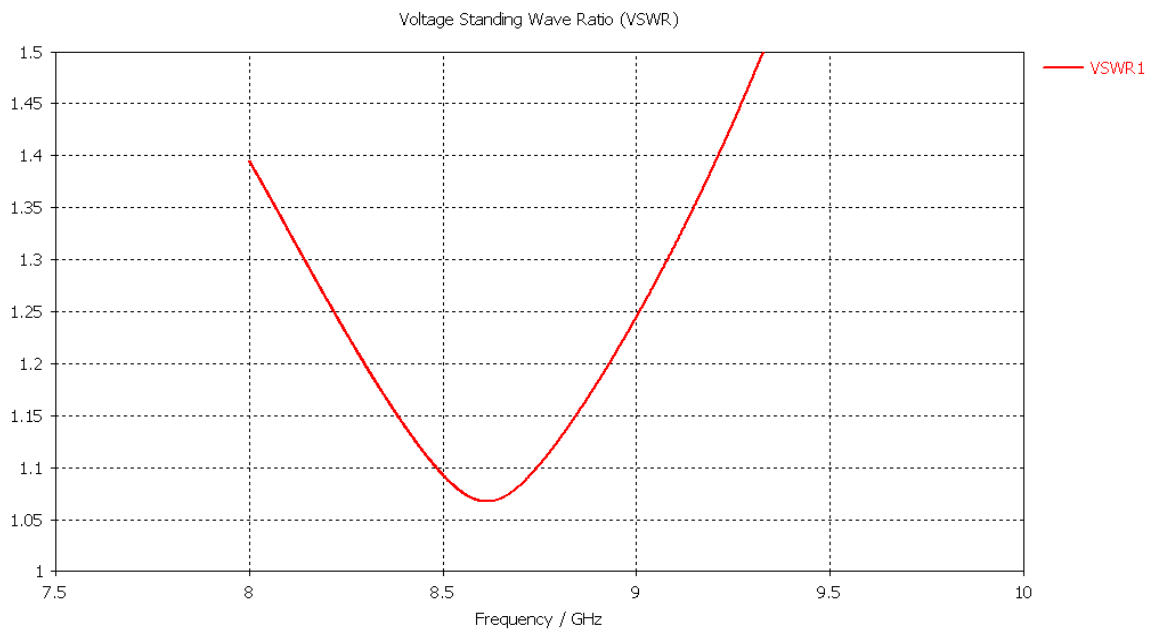


Figure 5-5 VSWR versus frequency for X band waveguide with nichrome film on the glass substrate- design parameters are given in Table (5-1)

Figure (5-5) shows the VSWR graph versus frequency that is plotted in CST MICROWAVE STUDIO following the  $S_{11}$  graph given in Figure (5-4). This is plotted in order to compare directly with the VSWR plot in the paper by Lane and Evans. The minimum value is at  $f = 8.55$  GHz and it is about 1.06.

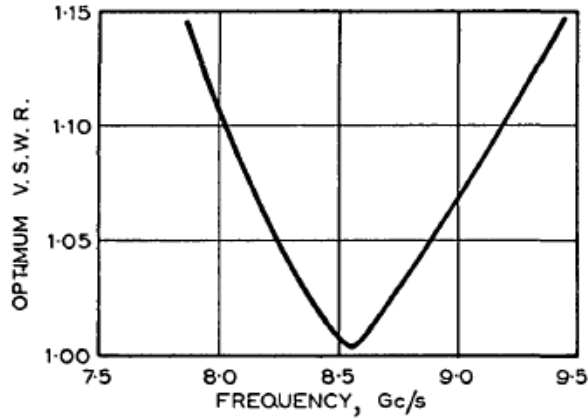


Figure 5-6 VSWR versus frequency taken from [29]

Figure (5-6) shows the VSWR versus frequency graph from the paper by Lane and Evans [29]. In this figure the minimum value is also at  $f = 8.55$  GHz and the value is almost 1. Comparing Figures (5-4) and (5-5) and (5-6) show good compatibility although the optimum value in Figure (5-5) given by CST MICROWAVE STUDIO is 0.05 worse.

### 5-1-2 Second case

The second case in the Lane and Evans paper is to design a pretuned bolometer. In this case the film element position in the waveguide is not tuneable and it is fixed at a predetermined location. The film is located at  $l = 13$  mm or  $\frac{l}{\lambda_g} = 0.282$  to the back-short, which is slightly larger than a quarter of the guided wavelength. The nichrome film with a width of 0.356 cm is deposited on the glass substrate with the same dimensions as in the previous case. The DC resistance that leads to a matched circuit this time is  $R = 446 \Omega$  and the thickness of the thin film is calculated from this DC resistance Equation (5-7) to be  $t = 7.038$  nm. The inductive reactance value is calculated from Equation (5-6) to be  $X = 91 \Omega$ . The optimum VSWR is achieved at  $f = 9.26$  GHz in the paper. Using Equation (5-4) the characteristic impedance is

calculated experimentally to be  $Z_0 = 465 \Omega$  and using Equation (5-9) gives a slightly different result of  $Z_{wv} = 475 \Omega$ .

Table 5-2 Parameters of design for thin nichrome film on glass substrate to operate at  $f = 9.26$  GHz in X-band waveguide

<b>Parameter</b>	<b>Value</b>	<b>Parameter</b>	<b>Value</b>
Film height	10.16 mm	Length to back-short	13 mm
Film thickness	7.038 nm	Guided wavelength	45.9 mm
Film width	3.56 mm	Film conductivity	9.09 e+5 S/m
Substrate height	10.16 mm	Film resistivity	1.10 e-6 $\Omega$ .m
Substrate thickness	0.12 mm	Substrate resistivity	1e+11 $\Omega$ .m
Substrate width	4 mm	Skin depth	5.48 $\mu$ m
Characteristic impedance	465 $\Omega$		

The calculated parameters are given in Table (5-2) and the resultant VSWR is shown in Figure (5-7). Using the parameter values described above, the VSWR of almost 1.01 is achieved at  $f = 9.26$  GHz.

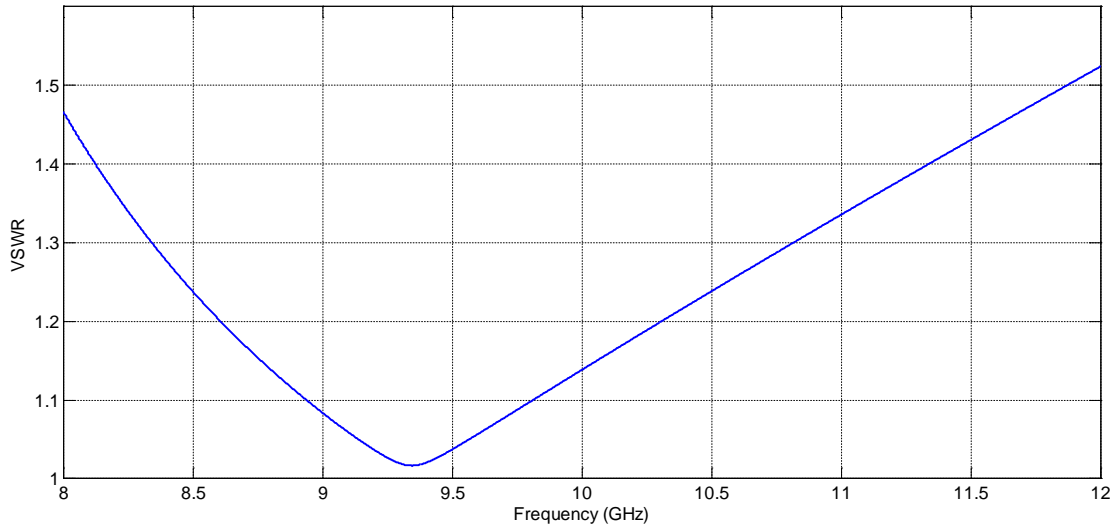


Figure 5-7 VSWR versus frequency for X band waveguide with nichrome film on the glass substrate- design parameters are given in Table (5-2)

The next step is to use the same parameters given in Table (5-2) to design the structure in CST MICROWAVE STUDIO and compare the calculation and simulation results.

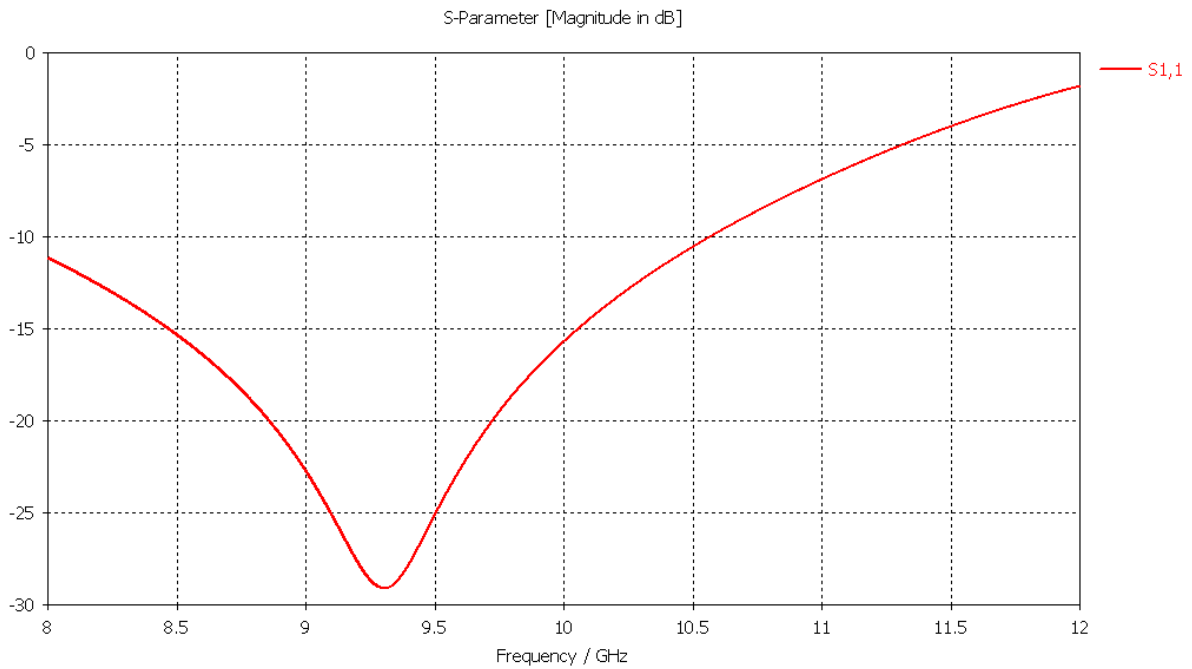


Figure 5-8 S<sub>11</sub> versus frequency for X band waveguide with nichrome film on the glass substrate- design parameters are given in Table (5-2)

Figure (5-8) shows the S<sub>11</sub> graph for the designed structure. The structure is designed in CST MICROWAVE STUDIO based on the information given in Table (5-2) which is for the second case of the pretuned bolometer, in Lane and Evans' paper [29]. As expected the S<sub>11</sub> is lowest at  $f = 9.26$  GHz.

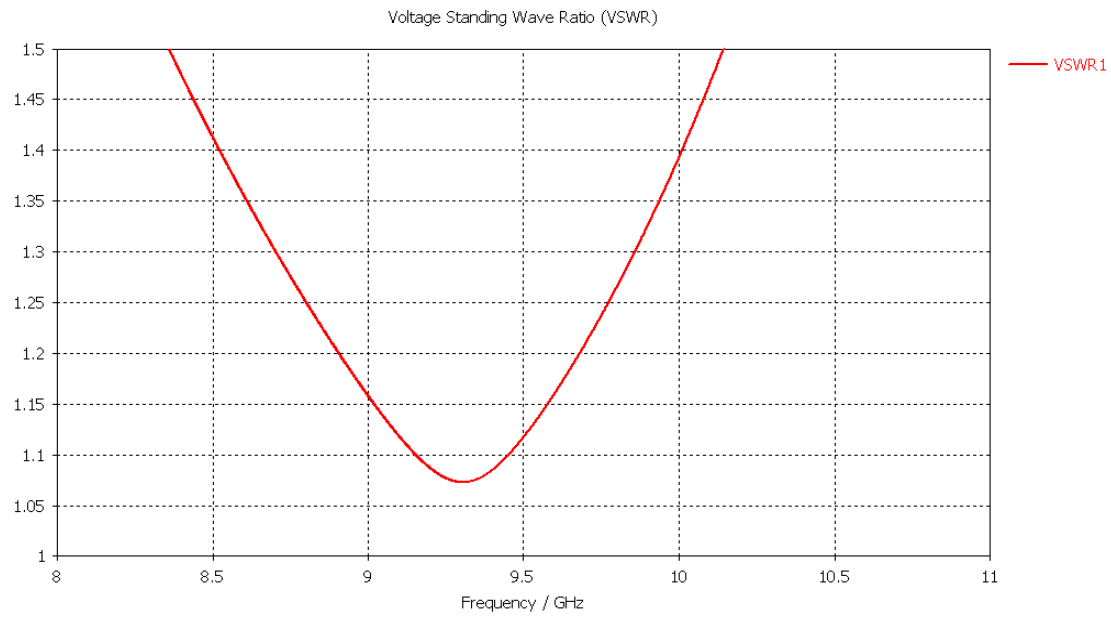


Figure 5-9 VSWR versus frequency for X band waveguide with nichrome film on the glass substrate- design parameters are given in Table (5-2)

Figure (5-9) shows the VSWR graph versus frequency that is plotted in CST MICROWAVE STUDIO with the same parameters as the  $S_{11}$  graph given in Figure (5-8). The VSWR minimum value is at  $f = 9.26$  GHz and it is about 1.07.

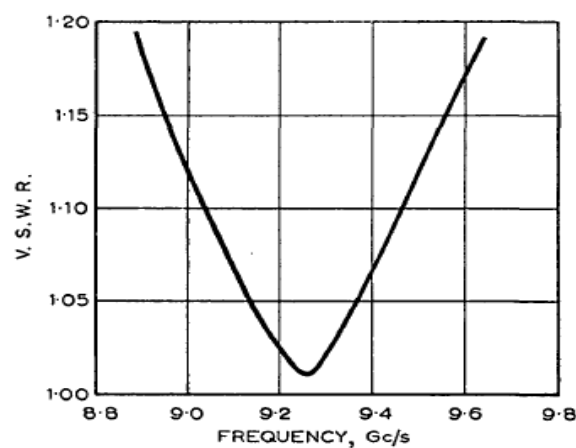


Figure 5-1 VSWR versus frequency taken from [29]

Figure (5-10) shows the graph of VSWR versus frequency of Lane and Evans' paper. It shows that at frequency 9.26 GHz there is an optimum value of the VSWR and it is very close to 1. This is a good match with the results generated from the calculations and in CST MICROWAVE STUDIO, provided in Figures (5-7) and (5-9). There is only about 0.05 difference between the optimum value in Figure (5-10) and Figure (5-9) derived in CST MICROWAVE STUDIO.

All these results confirm the theory is fully understood and followed correctly and the next section goes on to design a thin film with platinum instead of nichrome.

## **5-2 Platinum film bolometer**

Now that the method Lane and Evans used is understood and verified, it is used to design a similar power sensor with platinum film. The method of designing the thin film bolometer is very similar to that which was derived in Chapter 4 for the metal post element.

The values of resistance and reactance of the thin films should be found in such a way to result in a zero reflection coefficient. To achieve it, Equation (5-4) is used to make sure the real part is equal to the characteristic impedance, which is calculated from Equation (5-8); and Equation (5-5) is used to make sure the imaginary part is zero.

Using these equations and Equation (5-6), the graph of the reflection coefficient versus length for a resistive and inductive element that is given in Chapter 4, for different values of resistance and their corresponding value of reactance, is plotted. Here it is plotted only for  $R = 444.08 \Omega$  and from Equation (5-4)  $X$  must be  $0.61 \Omega$ . The length at which this resistive and inductive element leads to a minimum reflection coefficient is shown in Figure (5-11) and it is found from Equation (5-6) which is repeated below:

$$l = \frac{1}{\beta} \tan^{-1}\left(\frac{-R}{X}\right) \quad (5-11)$$

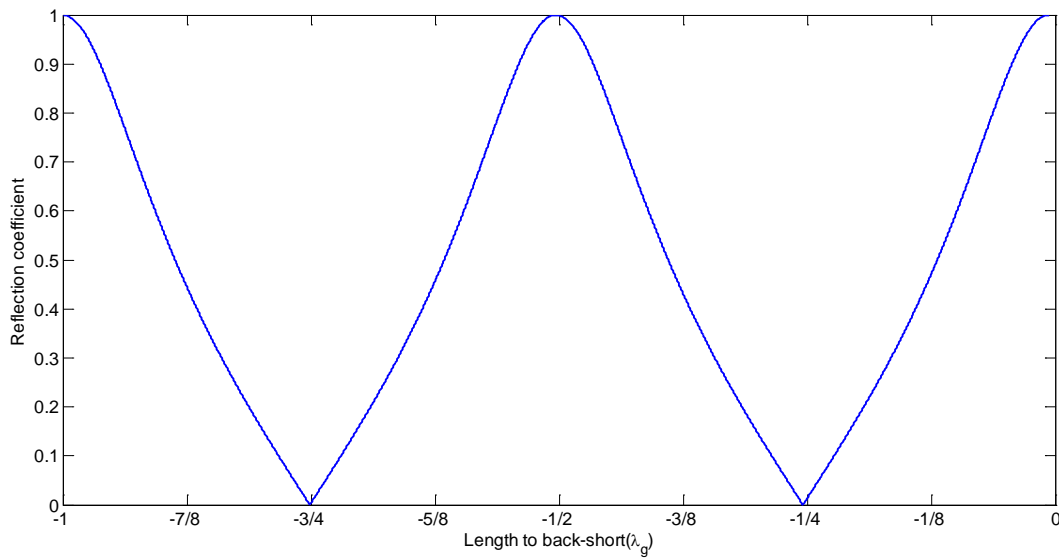


Figure 5-11 Reflection coefficient of resistive and inductive element versus length to back- short,  $R = 444.08 \Omega$ ,  $X = 0.61 \Omega$ ,  $\lambda_g = 40 \text{ mm}$

As can be seen in Figure (5-11) the minimum reflection coefficient for  $R = 444.08 \Omega$  and  $X = 0.61 \Omega$  occurs when the film is located at  $l = 0.25\lambda_g = 9.9 \text{ mm}$  and  $l = 0.75\lambda_g = 29.8 \text{ mm}$  to the back-short.

An equation for calculating the normalized reactance of a thin film is given in Marcuvitz [52] and Sakurai [32]:

$$\frac{X}{Z_0} = \frac{a}{2} \left[ \ln \left( \frac{8a}{\pi e^2 w} \right) + \frac{4}{27} \left( \frac{a}{\lambda} \right)^2 \right] \quad (5-12)$$

This equation is plotted in Figure (5-12) and is valid only when the ratio of film width to the waveguide cross-section width agrees with the condition of  $\frac{w}{a} \ll 0.15$ , which is achieved here. Therefore this equation can be used to find the width for which the reactance is  $X = 0.61 \Omega$  and it is found to be  $w \approx 1 \text{ mm}$ .

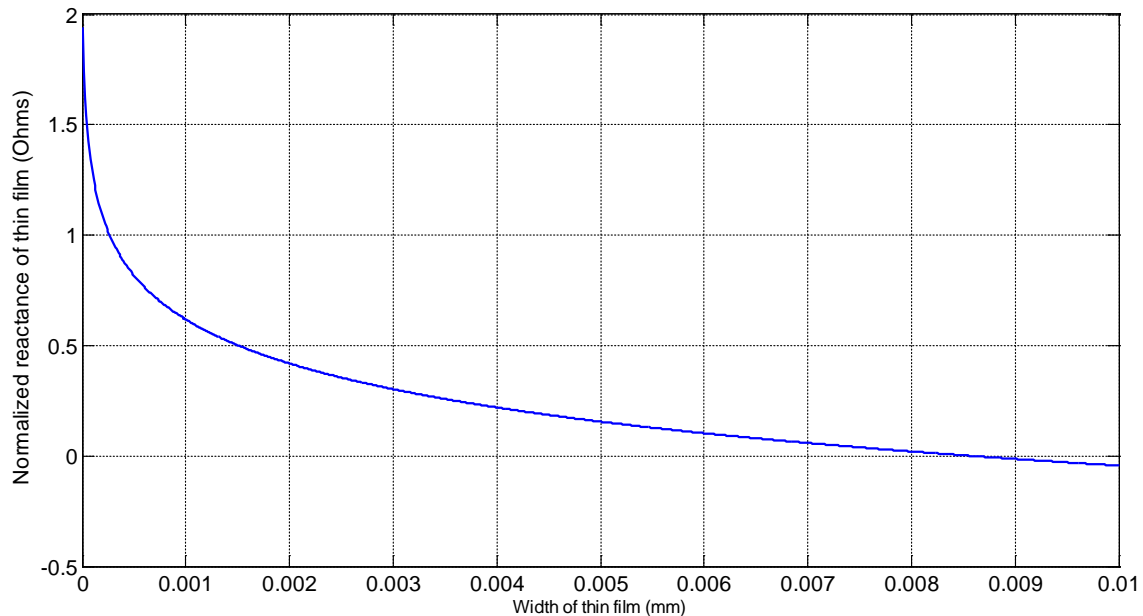


Figure 5-12 Normalized reactance Equation (5-12) versus film width

On the other hand, the film resistance can be calculated from the DC resistance Equation (5-7) and it is determined to be  $R = 444.08 \Omega$ . The width of the platinum film is calculated from Equation (5-12) and from Equation (5-7) the thickness is calculated to

be  $t = 2.435$  nm. This is very thin and may be difficult to make in practice. It is deposited on the glass substrate with the same dimensions as the thin film.

The aim is to have power absorption at the centre frequency of operation that is  $f = 10$  GHz.

Table 5-3 Parameters of design for thin platinum film on glass substrate to operate at  $f = 10$  GHz in X-band waveguide

Parameter	Value	Parameter	Value
Film height	10.16 mm	Length to back-short	9.9 mm
Film thickness	2.425 nm	Guided wavelength	40 mm
Film width	1 mm	Film conductivity	9.52 e+6 S/m
Substrate height	10.16 mm	Film resistivity	10.6 e-8 $\Omega$ .m
Substrate thickness	0.12 mm	Substrate resistivity	1e+11 $\Omega$ .m
Substrate width	1 mm	Skin depth	1.631 $\mu$ m
Characteristic impedance	444.08 $\Omega$		

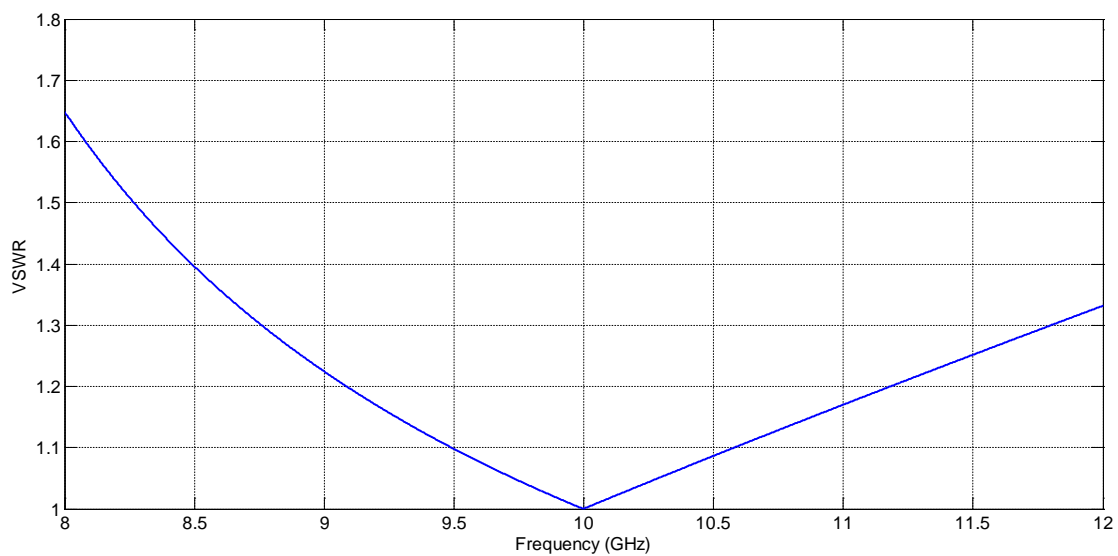


Figure 5-13 VSWR versus frequency for X band waveguide with platinum film on the glass substrate- design parameters are given in Table (5-3)

Figure (5-13) shows the VSWR versus frequency graph. The VSWR of 1 is achieved at  $f=10$  GHz; the parameters used to get this result are shown in in Table (5-3).

Using the parameter values given in Table (5-3) for this design it is also simulated in CST MICROWAVE STUDIO and the  $S_{11}$  response is given in Figure (5-14).

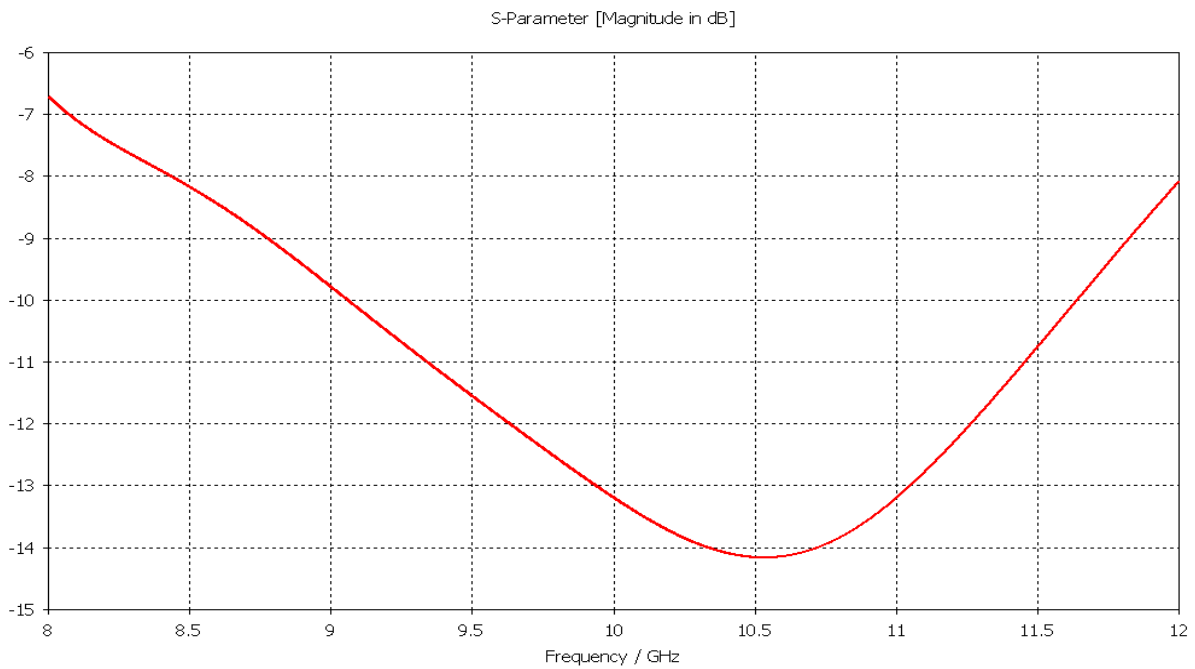


Figure 5-14  $S_{11}$  versus frequency for X band waveguide with platinum film on the glass substrate- design parameters are given in Table (5-3)

Figure (5-14) shows the figure of  $S_{11}$  of the thin platinum film on the glass substrate in the X-band rectangular waveguide. It is located at  $\lambda_g/4$  to the short circuit termination to achieve the matching circuit at  $f = 10$  GHz. As seen in this graph the minimum  $S_{11}$  is achieved at  $f=10.5$  GHz to be -14 dB. Since the aim is to get this minimum at  $f=10$  GHz, optimization is used to alter the initial values of length, width and thickness.

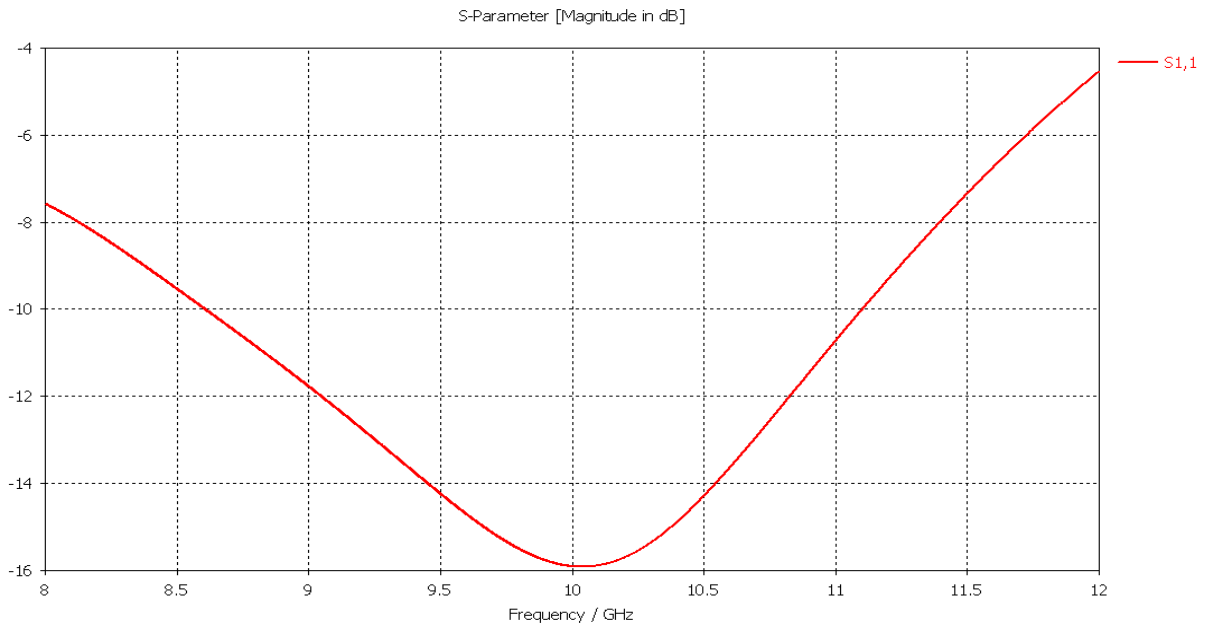


Figure 5-15 Optimized S<sub>11</sub> versus frequency for X band waveguide with platinum film on the glass substrate-  
initial design parameters are given in Table (5-3)

Figure (5-15) illustrates the S<sub>11</sub> response of the optimized design. Some of the initial parameters are slightly altered and the new values are: a distance length of 11.97 mm, film thickness of 2.38 nm and width of 1.02 mm; which have resulted in getting the minimum S<sub>11</sub> of -16dB at  $f=10$  GHz. This shows that the element is properly absorbing the power at the desired frequency.

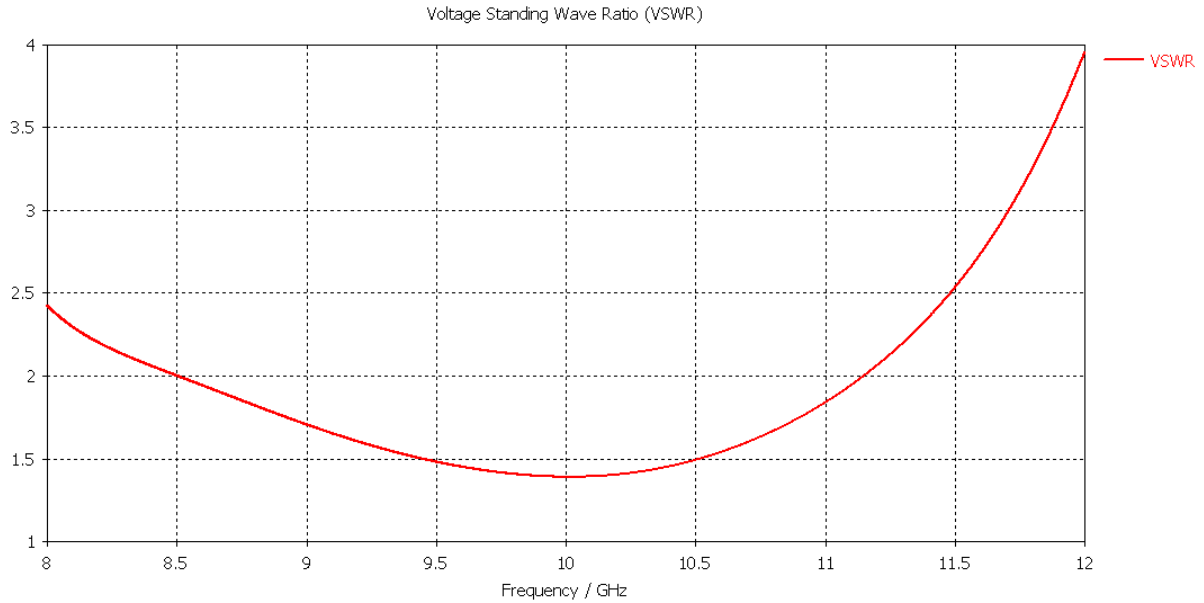


Figure 5-16 VSWR versus frequency of the optimized response, Figure (5-15), for X band waveguide with platinum film on the glass substrate

Figure (5-16) shows the VSWR graph versus frequency that is plotted in CST MICROWAVE STUDIO following the  $S_{11}$  graph given in Figure (5-15). This is plotted in order to compare directly with the VSWR plot based on Table (5-3), Figure (5-13). The minimum value is at  $f = 10$  GHz and it is about 1.39 which is not same as Figure (5-13). This is expected since the  $S_{11}$  results in Figure (5-15) are not very low.

The  $S_{11}$  result of around -16 dB in Figure (5-15) for the platinum film is not as good as the result of Nichrome film -29 dB in Figure (5-8). Both results are good, representing an excellent power absorption by the thin film. However, despite work to reduce the -16 dB in the optimizer, this has not been possible. The residue reflection in both cases can be explained by the film/substrate combination not being represented by a perfect series combination of an inductor and resistor. In fact the equivalent circuit is more complex resulting in the residual reflection, the case of the platinum film seems to have more

reflection. To overcome this further work on the shape of the film/substrate is require to further optimize the reflection coefficient. Because of the relatively good results, of -16 dB and -29dB, this has not been done.

In this chapter the experimental nichrome design of Lane and Evans was verified and based on the confirmed theory a new platinum thin film element was designed that is fully working.

## CHAPTER 6 – CONCLUSION AND FUTURE WORK

Power and power detection are important, especially at microwave frequencies because the parameters of voltage and current are difficult to measure at these frequencies. Therefore power becomes an important parameter and knowledge about it is critical for work in this frequency range [1] [3].

The lack of knowledge about the power restricts progress and advancement in many different applications. The existence of a simple power detector for high frequency signals, allows easier power measurement that leads to improvement and developing new equipment, applications and methods in scientific areas such as astronomy, satellite communications, medical diagnosis, imaging and many more. All these areas require accurate knowledge of power in order to be able to function and progress correctly and efficiently and they would benefit from an accurate linear and repeatable power detector [11] [12] [27].

An extensive background survey has been carried out around the principles of power detectors and methods of power detection in order to understand its concepts and the available methods. The aim is to produce a linear waveguide bolometer with a resistance changing heat sensitive bolometer element to work at mm-wave frequencies. To be able to design this power detector, the principles of bolometers' performance were studied and understood.

The proposed structure in this thesis is designed at X-band (8.2-12.4 GHz) using a WR90 waveguide. Two heat sensing elements are modelled here; one is an inductive metal post

and secondly a thin film element. Using the theory and calculations the dimensions for a bolometer with a resistive metal post are determined and the model is simulated. Good power absorption is achieved for the designed structure, although the material that is used to make the post is not practical. Then using a similar approach and following a paper, the thin film element was designed and simulated and good power absorption was achieved. The waveguide with the power-absorbing element is the main deliverable factor of this project. The proven theory can be used to design power detectors in smaller waveguides at the higher frequency bands with WR3 and WR6 waveguides.

## **6-1 Limitations**

The designed power absorbers sense the power, work in the characterized frequency range and specifically absorb the power mostly at the centre frequency of operation, as was desired. The design with the post works well, but the material of which the post is made is not a common material and only the electrical conductivity of it is known. Therefore it has not been possible to test this design practically with a conventional X-band waveguide and metal post. It is not possible to find a suitable material for the post as no obvious, simple materials are immediately available.

## **6-2 Future work**

In this work the thermal properties of the power sensor have not been considered; this is crucial to making a practical device. The power sensor element must be terminally

isolated from the waveguide walls in order to have the highest sensitivity. In addition, the power sensor element must be electrically isolated from the microwave radiation, so that no energy escapes into the external electronics of the Wheatstone bridge. Both these considerations are interesting practical aspects which must be considered in future work.

This project has the potential to be developed vastly. The concept of matching and design are explained and validated step by step; therefore it would be straightforward to use it with other different power sensing elements and design other simple power detectors.

Further work could be carried out to find an applicable common material for the post and test the design practically. As for the thin film element, the theory can be used for other thin film materials and for higher frequencies.

Nowadays semiconductor and terahertz technology are developing at a fast pace; therefore there is a need for accurate power detection at those frequencies, not only for laboratory use but for industries as well. Different projects will definitely be proposed to design power detection for these frequencies. The method used in this project can be used for higher frequencies by doing the calculations and altering the dimensions to be compatible with high frequency signals. At the moment there is demand for WR6 and WR3 waveguide power detectors, so this work can be developed and used to contribute to these types of bigger projects. Micro-machined technology can be used to make these high frequency new designs [11] [12] [27] and the equations developed here are valid for all of them.

## References

- [1] Agilent, "Agilent technologies, Inc," Agilent, 4 june 2008. [Online]. Available: [www.agilent.com](http://www.agilent.com). [Accessed 3 june 2013].
- [2] E. L. Ginzton, Microwave measurements, USA: Mcgraw hill, 1957.
- [3] Hewlett and Packard, "Hewlett Packard Application note 64-1A," june 1998. [Online]. Available: [www.agilent.com](http://www.agilent.com). [Accessed 3 june 2013].
- [4] N. Erickson, "A fast and sensitive submillimeter waveguide power meter," *Internatioonal symposium od space terahertz technology*, no. 10th, pp. 502-507, 1999.
- [5] French and Cullen, "AN INSTRUMENT FOR THE ABSOLUTE MEASUREMENT OF LOW-LEVEL MICROWAVE POWER IN THE 3CM BAND," *institution monograoh*, vol. 104, no. 237 R, pp. 456-464, 1957.
- [6] J. A. Lane, "TRANSVERSE FILM BOLOMETERS FOR THE MEASUREMENT OF POWER IN RECTANGULAR WAVEGUIDES," *the institution of electrical engineers*, pp. 77-80, 1958.
- [7] A. Fantom, Radio frequency and microwave power measurement, London: peter peregrinus ltd., 1990.
- [8] J. F. Gerling, "EQUIPMENT AND METHODS FOR WAVEGUIDE POWER MEASUREMENT IN MICROWAVE HEATING APPLICATIONS," *Gerling Applied Engineering Inc*, pp. 1-8, 2002.
- [9] J. P. Dunsmore, Handbook of Microwave component measurement: with advanced VNA Techniques, John Wiley and sons, 2012.
- [10] A. J. B. Fuller, Microwaves, oxford: pergamon intenational library, 1979.
- [11] P. H. Siegel, "Terahertz Technology," *IEEE TRANSACTIONS ON MICROWAVE THEORY AND TECHNIQUES*, vol. 50, no. 3, pp. 910-928, 2002.
- [12] M. C. Gaidis, "Space-Based Applications of Far-Infrared Systems," *8th International Conference on Terahertz Electronics* , pp. 125-128, 2000.
- [13] O. C. L. THEODORE MORENO, "Microwave Power Measurement," *PROCEEDINGS OF THE I.R.E.- Waves and Electrons Section*, no. R245.2., pp. 514-518, 1947.
- [14] T. nemoto and k. Sakurai, "A thin film bolometer unit," *IEEE TRANSACTIONS ON INSTRUMENTATION AND MEASUREMENT*, pp. 206-211, 1967.

- [15] R. C. Jones, "the general theory of bolometer performance," *Journal of the optical society of America*, pp. 1-14, 1953.
- [16] T. L. Hwang, S. Schwarz and D. Rutledge, "Microbolometers for infrared detection," *Applied physics letter*, vol. 34, no. 11, pp. 773-776, 1979.
- [17] D. Froebrich, "Astrophysic lecture," 9 october 2007. [Online]. Available: [http://astro.kent.ac.uk/~df/teaching/ph507/tel\\_3.pdf](http://astro.kent.ac.uk/~df/teaching/ph507/tel_3.pdf). [Accessed 11 januaru 2013].
- [18] K. Hoffman, "HBM Applying the Wheatstone bridge circuit," [Online]. Available: <http://www.hbm.com/fileadmin/mediapool/hbmdoc/technical/s1569.pdf>. [Accessed 2 June 2013].
- [19] C. Montgomery, E. Purcell and R. H. Dicke, *Principles of microwave circuits*, London: Peter Peregrinus, 1987.
- [20] W. Herschel, *the royal society: philosophical transactions*, vol. 90, pp. 284-292, 1800.
- [21] L. Brunetti, "Thin-film bolometer for high-frequency metrology," *Sensors and actuators*, vol. A, no. 32, pp. 423-427, 1992.
- [22] D. M. Kerns, "Analysis of direct current bolometer bridge," *Part of the journal of research of the national bureau of standards*, vol. 43, no. Research paper RP2051, pp. 581-589, 1949.
- [23] J. A. Lane, *Microwave over measurement*, 1972.
- [24] A. technology, "Fundamentals of RF and Microwave Power Measurements," 2000. [Online]. Available: [http://my.ece.ucsb.edu/York/Yorklab/Useful%20Stuff/Tutorials/RFPower\\_Meas%20AN64-1B.pdf](http://my.ece.ucsb.edu/York/Yorklab/Useful%20Stuff/Tutorials/RFPower_Meas%20AN64-1B.pdf). [Accessed 20 may 2015].
- [25] T. Inoue and I. Yokoshima, "High performance thin film barretter mount for power measurement in W-band," *Electronic letter*, vol. 21, no. 5, pp. 170-172, 1985.
- [26] J. J. Carr, *RF components and circuits*, oxford: Newnes, 2002.
- [27] M. J. Lancaster, *Micromachined Power detector EMRP Research Proposal*, Birmingham: University of Birmingham, 2013.
- [28] CST Computer simulation technology, "CST- Computer Simulation Technology," CST Studio, 2015. [Online]. Available: [http://www.cst.com/Content/Products/CST\\_S2/Overview.aspx](http://www.cst.com/Content/Products/CST_S2/Overview.aspx). [Accessed 28 May 2015].
- [29] J. Lane and D. Evans, "THE DESIGN AND PERFORMANCE OF TRANSVERSE-FILM BOLOMETERS IN RECTANGULAR WAVEGUIDES," *the institution of electrical engineers*, no. 3392, pp. 133-135, 1961.

- [30] R. Hansen and W. Pawlewicz, "Effective Conductivity and Microwave Reflectivity of Thin Metallic film," *IEEE transactions on microwave and techniques*, vol. 30, no. 11, pp. 2064-2066, 1982.
- [31] F. Ulaby, *Fundamentals of applied electromagnetics*, New Jersey: Prentice Hall, 1999.
- [32] T. N. Kenjiro Sakurai, "A thin film bolometer unit," *IEEE TRANSACTIONS ON INSTRUMENTATION AND MEASUREMENT*, pp. 206-211, 1967.
- [33] J. Brown, "Reactive effects in transverse-film bolometers in rectangular waveguide," *Proceedings IEE*, vol. 110, no. 1, pp. 77-78, 1963.
- [34] C. R. Paul and S. A. Nasar, *Introduction to electromagnetic fields*, 2nd ed., New York: McGraw-Hil, 1987.
- [35] M.D.Pozar, *Microwave Engineering*, 3 ed., LONDON: Wiley, 2005.
- [36] Prof.York, "Mishra and your group," 3 july 2001. [Online]. Available: [my.ece.ucsb.edu/York/Bobsclass/134/Handouts/Tline134.pdf](http://my.ece.ucsb.edu/York/Bobsclass/134/Handouts/Tline134.pdf). [Accessed 2 november 2014].
- [37] T. S. Bird, "Definition and Misuse of Return Loss," *To appear IEEE Antennas & Propagation Magazine*, pp. 1-5, April 2009.
- [38] A. Hollister, "Scattering Parameters & Smith Charts," 2007.
- [39] H. Dr. Johnson, "High-Speed Digital Design Online Newsletter," Signal Consulting, Inc., 2003.
- [40] I. C. Hunter, *Theory and design of microwave filters*, London: Institution of Engineering and Technology, 2001.
- [41] J. C. Whitaker, *The RF transmission system handbook*, CRC Press LLC, 2002.
- [42] K. R. Demarest, *Engineering Electromagnetics Chapter 7*, Kansas: Marcel Dekker Inc., 2004.
- [43] J. Uher, J. Bornemann and U. Rosenberg, *Waveguide Components for Antenna Feed Systems.: theory and CAD*, Boston; London: Artech House, 1993.
- [44] N. YONEDA, M. MIYAZAKI and T. NOGUCHI, "A 90GHz-Band Monoblock Type Waveguide Orthomode Transducer," *IEEE MTT-S Digest*, 1999.
- [45] S. Cruz-Pol, "Rectangular waveguide.ppt," INEL 6216, Puerto Rico, 2004.
- [46] J. Brown, "Reactive effects in transverse-film bolometers in rectangular waveguide," *PROCEEDINGS I.E.E.*, pp. 77-78, 1963.
- [47] M. J. Lancaster, "RF and Microwave lecture notes," University of Birmingham, Birmingham, 2012.

- [48] Agilent, "Agilent Technologies, Inc.," 4 June 2008. [Online]. Available: [www.agilent.com](http://www.agilent.com). [Accessed 3 June 2013].
- [49] S. Ramo, J. R. Whinnery and T. Van Duzer, *fields and waves in communication electronics*, canada: John wiley and sons, inc., 1994.
- [50] M. Potok, "The design of inductive post-type microwave filters," *Journal Brit I.R.E.*, pp. 263-272, 1958.
- [51] Sorrentino, G. Bianchi and Roberto, *Electronic filter simulation and design*, New York: Mc Graw hill, 2007.
- [52] N. Marcuvitz, *Waveguide Handbook*, London: Peter Peregrinus, Ltd., 1986.
- [53] S. F. Adams, Hewlett and Packard, *Microwave theory and applications*, Longman Higher Education, 1970.
- [54] S. E. Behbahani, "Filter-based Orthomode Transducer," University of Birmingham, Birmingham, 2012.
- [55] G. Narayan and N. Erickson, "Full-Waveguide Band Orthomode Transducer for the 3 mm and 1 mm Bands," *14th International Symposium on Space Terahertz Technology*, pp. 508-512.
- [56] A. I. SANDHU, "Design of an Orthomode Transducer in Gap Waveguide Technology," *Master of Science Thesis in the program Communication Engineering*, 2010.
- [57] G. G. Gentili, R. Nesti, G. Pelosi and S. Selleri, "Encyclopaedia of RF and Microwave Engineering- Orthomode Transducers," *Published Online: John Wiley & Sons, Inc*, 2005.
- [58] Y. H. Kim, H. Lee and S. G. Park, *A Turnstile Junction Waveguide Orthomode Transducer for the Simultaneous Dual Polarization Radar*, KOREA: IEEE, 2009.
- [59] "CST," 2012. [Online]. Available: [http://www.cst.com/Content/Products/CST\\_S2/Overview.aspx](http://www.cst.com/Content/Products/CST_S2/Overview.aspx). [Accessed 28th march 2012].
- [60] M. Lancaster, *Microwave Engineering Lecture note*, Birmingham: The university of Birmingham, 2010.
- [61] A. Boifot, E. Lier and T. Schaug-Pettersen, "Simple and broadband orthomode transduce," *IEE PROCEEDINGS*, vol. 137, pp. 396-400, 1990.
- [62] A. Perov, L. Rud and V. Tkachenko, "ELECTROMAGNETIC SIMULATION AND DESIGN OF DUAL-BAND ORTHO-MODE TRANSDUCERS," *International Conference on Antenna Theory and Techniques*, vol. 5, pp. 475-477, 2005.
- [63] M. Lancaster and J. S. Hong, *Microstrip filters for RF/microwave applications*, New York;

Chichester: Wiley, 2001.

- [64] F. McClatchie, "WHAT IS RETURN LOSS, AND WHY SHOULD I MEASURE IT?," *FM Systems, Inc.*, pp. 1-3.
- [65] F. McClatchie, "WHAT IS RETURN LOSS, AND WHY SHOULD I MEASURE IT?," *RETURN LOSSart, FM Systems, Inc.*, pp. 1-3.
- [66] "Exfiber Optical Technologies," 2011. [Online]. Available: <http://www.exfiber.com/tutorial/Insertion-Loss-31.html>. [Accessed 2nd December 2011].
- [67] B. Bahlmann and P. Ramkumar, "Birds-eye.net, r, XPD - Cross Polarization Discrimination," [Online]. Available: <https://www.birds-eye.net/definition/acronym/?id=1151878664>. [Accessed 28th November 2011].
- [68] D. Yong, T. Zongxi, Z. Biao and B. Lifen, "A Broad Band Orthomode Transducer," *International Symposium on Intelligent Signal Processing and Communication Systems*, 2010.
- [69] R. E. Collin, *Foundations for microwave engineering*, 2nd ed., New York: IEEE Press, 2001.
- [70] R. S. Elliot, *An Introduction to guided waves and microwave circuits*, Los Angeles: Prentice-Hall International, Inc., 1993.
- [71] M. J. Lancaster, *PASSIVE MICROWAVE DEVICE APPLICATIONS OF HIGH-TEMPERATURE SUPERCONDUCTORS*, Cambridge: Cambridge University Press, 1997.
- [72] M. Ohring, *The materials science of thin films*, New Jersey: Academic Press, 1992.

## **APPENDIX 1**

# **Resonator Based Orthomode Transducer**

### **A1- Introduction**

The first part of the work described below was done in the final year project in 2012 [54].

However significant extra work was done in the MSc by Research primarily on optimization in section A4-2.

An Orthomode transducer (OMT) is a passive microwave device. It is a polarization duplexer; that separates or combines two waves with orthogonal polarizations of dominant mode in the same band of frequency; it can be used as a transmitter or a receiver. It allows frequency reuse of available frequency bands by transmitting and receiving signals which are in orthogonal polarizations with each other, simultaneously [55].

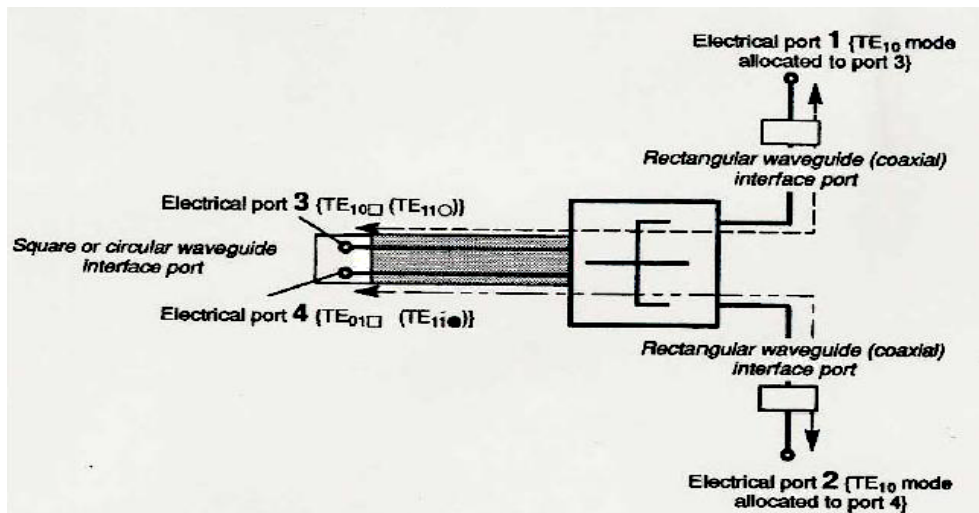


Figure A1 Simple OMT-taken from [56]

A simple OMT is designed here; it is made of three waveguides in total. Figure (A1) shows the structure diagrammatically [3]. Two of those are rectangular waveguides that are the arms connected to sides of the common square waveguide. There is a single wave travelling in the common waveguide that has dual polarization and can be decomposed in two waves which have orthogonal polarization with respect to each other. Each of these decomposed waves will travel through one of the rectangular waveguide arms, depending on which they are matched to. The OMT has three physical ports one for each waveguide and four electrical ports. Two of the electrical ports are for the common waveguide that supports two polarisations and the others are for the separate physical ports containing the single and separated polarisations [43]. The orthogonal dominant modes are  $TE_{10}$  and  $TE_{01}$  in the square waveguide; each of them will be routed to the appropriate output port [56] [57].

Some important criteria in designing an OMT are return loss, insertion loss, cross-polarization and isolation [58]. The performance of the design is verified using mainly return loss and insertion loss throughout this report and isolation is verified later.

## **A2- CST Designs**

The software employed to design and simulate different structures in this project is CST STUDIO SUITE [59]. Designs and S-parameter graphs are generated using the frequency domain solver of software. All the waveguide bodies are made of Perfect Electric Conductor (PEC) and filled with Vacuum dielectric. The frequency band of operation is X-band with frequency range from 8.2 GHz to about 12.4 GHz. The rectangular waveguide operating in this band is called WR90 and its dimensions are 0.9×0.4 inches=22.8×10.16mm. The mode of interest for operation is the dominant mode of rectangular waveguide which is TE<sub>10</sub> mode. It has the lowest cut-off frequency of  $f_c \approx 6.57$  GHz in the band and therefore reduces the probability of existence of other higher order modes as they have higher cut-off frequencies [60]. For a square waveguide the dominant modes are TE<sub>10</sub> and TE<sub>01</sub> which here are referred to as mode 1 and mode 2, respectively. The proposed filter to be used in the OMT is a third order bandpass filter. It is a Chebyshev filter with 2% fractional bandwidth from 9.9 GHz to 10.1 GHz. The centre frequency is 10 GHz with the return loss of 20 dB.

### **A2-1 Basic OMT design without filtering**

The object of this work is to produce an OMT based on coupled resonators which includes filtering as well as the polarisation split. However, in order to understand the basic properties of the structure we initially look at a structure which has no filtering. The idea for the design is coming from [61]. The square waveguide has port 1 at its cross-section has area of

22.8 mm×22.8 mm. The guided wavelength ( $\lambda_g$ ) at centre frequency  $f = 10$  GHz is calculated as below:

$$\lambda_g = \frac{2\pi}{\beta} = 39.84 \text{ mm} \approx 40 \text{ mm} \quad (\text{A-1})$$

The design has one of the output arms perpendicular to the square waveguide and it is connected to the centre of the wall of that guide. The second rectangular waveguide is connected to the back of the square waveguide in line with the waveguide's propagation axis, so it is perpendicular to the other waveguide arm connected to common guide. This structure is designed based on [61] [62] and shown in Figure (A2). The dimensions for this design are provided in Table (A1).

Table A1 Parameters and their values for the OMT design.

<b>Parameter</b>	<b>Value (mm)</b>	<b>Description</b>
<i>a</i>	11.4	Length of the rectangular cross section (port 2)
<i>a</i>	11.4	Square waveguide's width
<i>b</i>	5.08	Width of the rectangular cross-section (port 2)
<i>c</i>	50	The length of waveguide (port 2)
<i>d</i>	11.4	Length of the rectangular cross section (port 3)
<i>e</i>	5.08	Width of the rectangular cross-section (port 3)
<i>f</i>	50	The length of waveguide (port 3)
<i>z</i>	104	Square waveguide's length

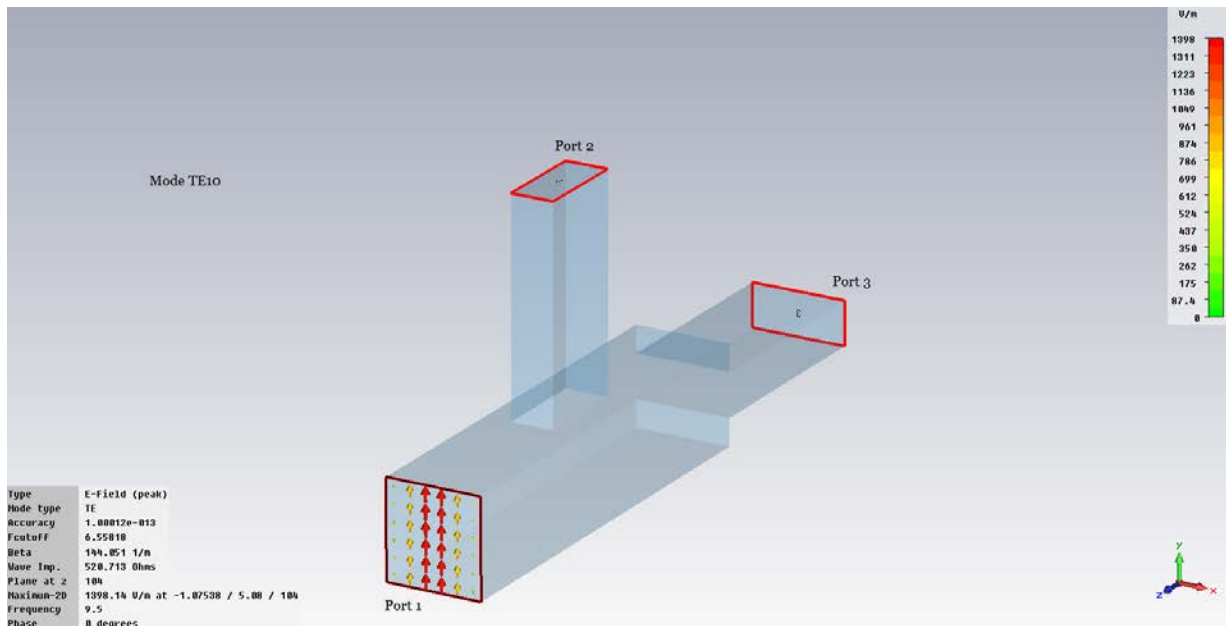


Figure A2 OMT design structure indicating mode  $TE_{10}$  at port one. The structure is designed in CST software

Figure (A2) shows the OMT structure with electric field of  $TE_{10}$  mode of the dual mode square waveguide which is the input mode used for the next few results. The electric field arrows of this mode are perpendicular to the  $x$  axis and have appropriate polarisation to couple to port 3. The direction of the electric field patterns for port 2 couples to the  $TE_{01}$  mode (not shown) of the square waveguide. So for mode  $TE_{10}$  at the square waveguide, due to the similarity in the orientation of electric field patterns, most of the power of the correct polarisation will come out of port 3.

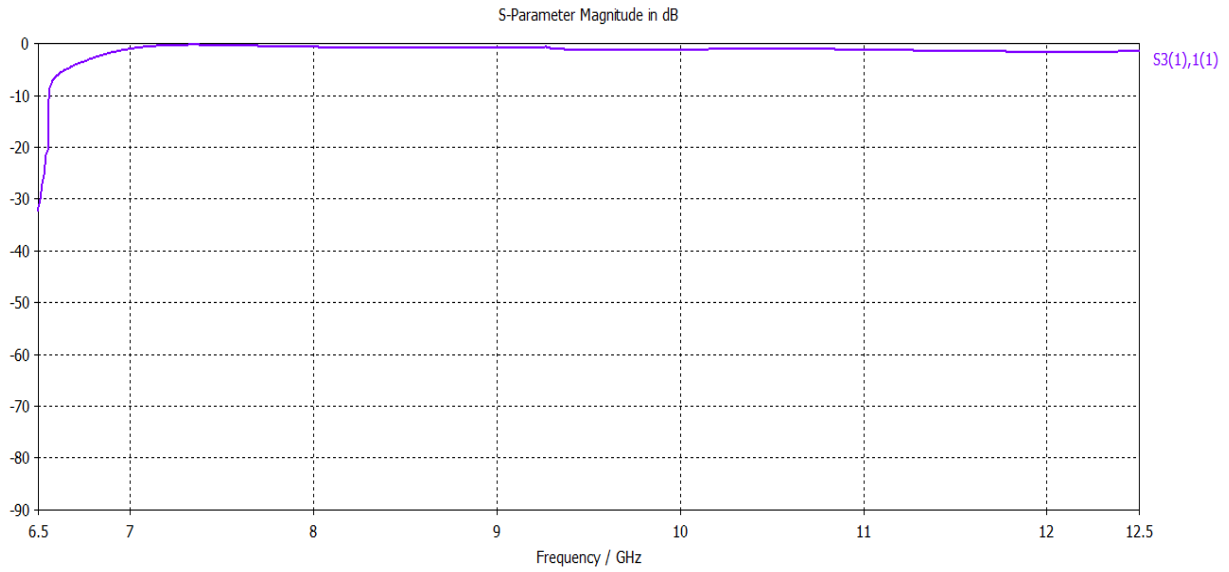


Figure A3 S<sub>31</sub> graph of the designed OMT for mode TE<sub>10</sub>- Generated in CST software by the student

As can be seen in Figure (A3) the S<sub>31</sub> response shows that the wave has been transmitted through waveguide with port three with very low loss. The amount of power which is lost in transmission through this branch is only about 2 dB.

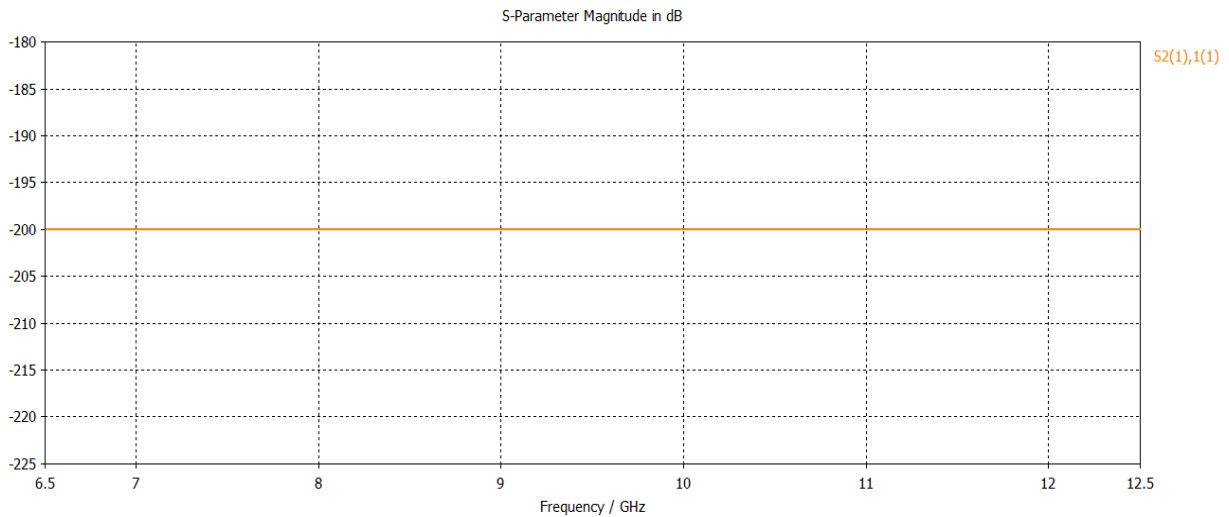


Figure A4 S<sub>21</sub> graph of the designed OMT for mode TE<sub>10</sub>- Generated in CST software by the student

The  $S_{21}$  response in Figure (A4) shows that due to the incompatible polarisation mode of the waveguide with port 2 with input mode, nearly no power is transmitted through that port. For  $TE_{01}$  mode, the electric field arrows are horizontal to the  $x$  axis. Therefore the wave goes to the other branching waveguide port which is port 2.

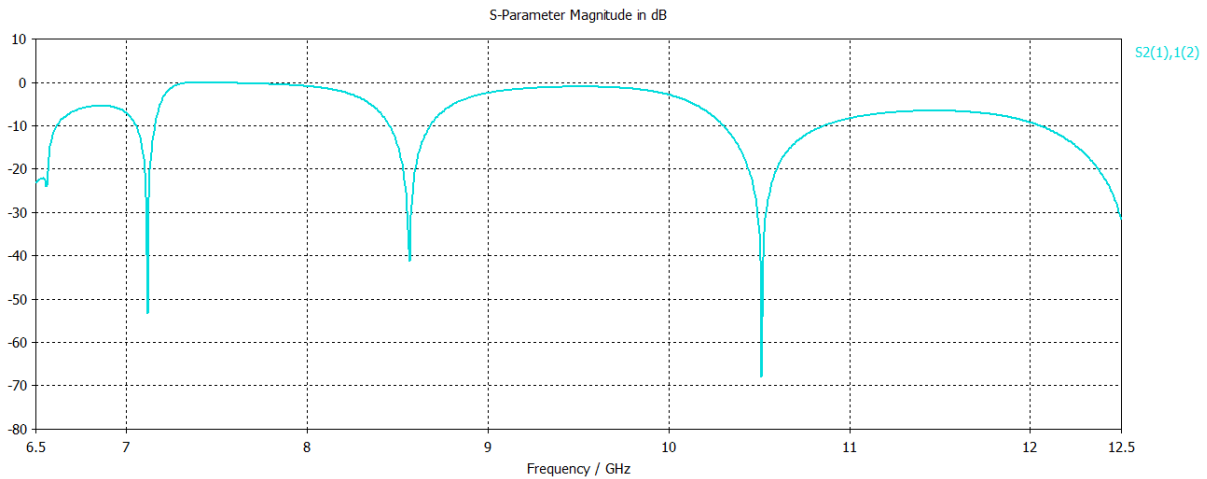


Figure A5  $S_{21}$  graph of the designed OMT for mode  $TE_{01}$ - Generated in CST software by the student

As seen in Figure (A5) almost all the power is coming out of port 2 but there are three large dips in the  $S_{21}$  response; showing that the diplexer for this mode is working in adjacent narrow bands of about 2 GHz wide and does not cover all the frequency band at once. For frequencies above 10.5 GHz there is a maximum loss of about 6 dB which is not very high. Meanwhile, the  $S_{31}$  in Figure (A6) has low value showing that negligible amount of power comes out of it.

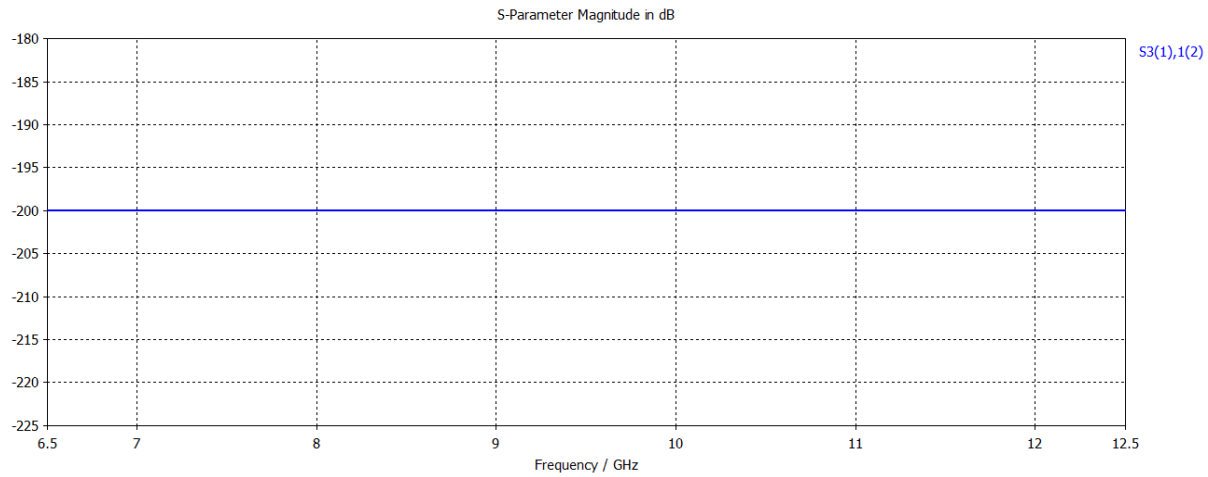


Figure A6  $S_{31}$  graph of the designed OMT for mode  $TE_{01}$ - Generated in CST software by the student

## A2-2 Determination and Improvement

In the  $S_{21}$  response as shown in Figure (A5), there are some dips which are desired to be removed. For mode  $TE_{01}$  the widest power transmission is between 8.5 GHz and 10.5 GHz but there is a very large dip at  $f = 10.5$  GHz which is very close to  $f = 10$  GHz, which is the desired centre frequency of the design, thus it is desired to be moved away. These dips are assumed to have occurred because of the way the branches are connected to the square waveguide that have created resonance [61]. The design of the structure is required to be improved to have the widest possible frequency range of power transmission in the X-band frequency centred at 10 GHz.

The parameter sweeping feature is used to change the location of the orthogonal waveguide with respect to the back of the square waveguide to find the most suitable position that leads to a better response. By changing this length and considering the relationship between wavelength and operation frequency, the peak of power transmitted on the  $S_{21}$  graph moves on the frequency axis and can be aligned to 10 GHz. As the orthogonal arm is moved away

from the back of square waveguide, the minimum attenuation in passband moves to lower frequencies. Better power transmission is achieved at  $f = 10$  GHz when the distance is about 28 mm and the peak frequency is located at 9.63 GHz.

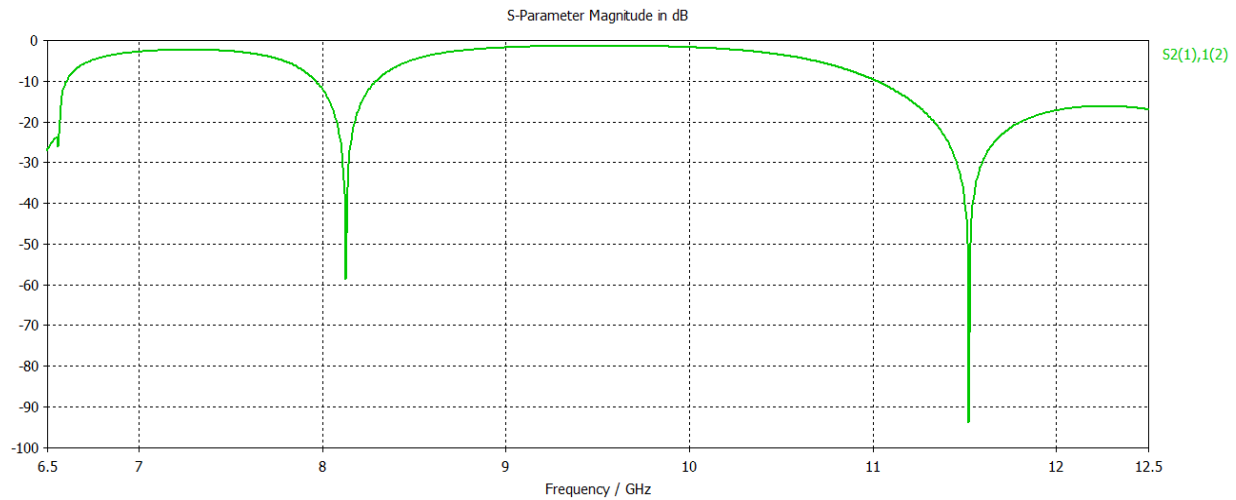


Figure A7 Improved  $S_{21}$  response to mode  $TE_{01}$  in the second OMT design- generated by student in CST software

The optimum length has found to be 28.93 mm and  $S_{21}$  is shown in Figure (A7). Knowing that the guided wavelength is 40 mm, the position of the centre of perpendicular waveguide arm cross-section has been altered by 72.25% of  $\lambda_g$ . It is located at approximately  $\frac{3\lambda_g}{4}$  from the end of the square guide. A sufficiently wide band of frequency from 8.2 GHz to 11.7 GHz that has the maximum power transmission for this response with the most achievable power transmission at  $f = 10$  GHz, is found.

## A2-3 Isolation

Isolation is the measure of leakage of the power from one waveguide arm, to the other arm [11]. It is useful in determining the performance of an OMT, knowing that high port isolation is desired. The  $S_{32}$  or  $S_{23}$  responses determine how much power is exchanged between the two ports.

Figure (A8) shows the isolation between port 2 and 3 for the OMT design for propagation of mode  $TE_{10}$ . As shown in figure the  $S_{32}$  response is -200 dB. This value implies that almost no power has been exchanged between these ports for this mode. Therefore for this OMT the output responses of two ports are independent of each other and the results are reliable.

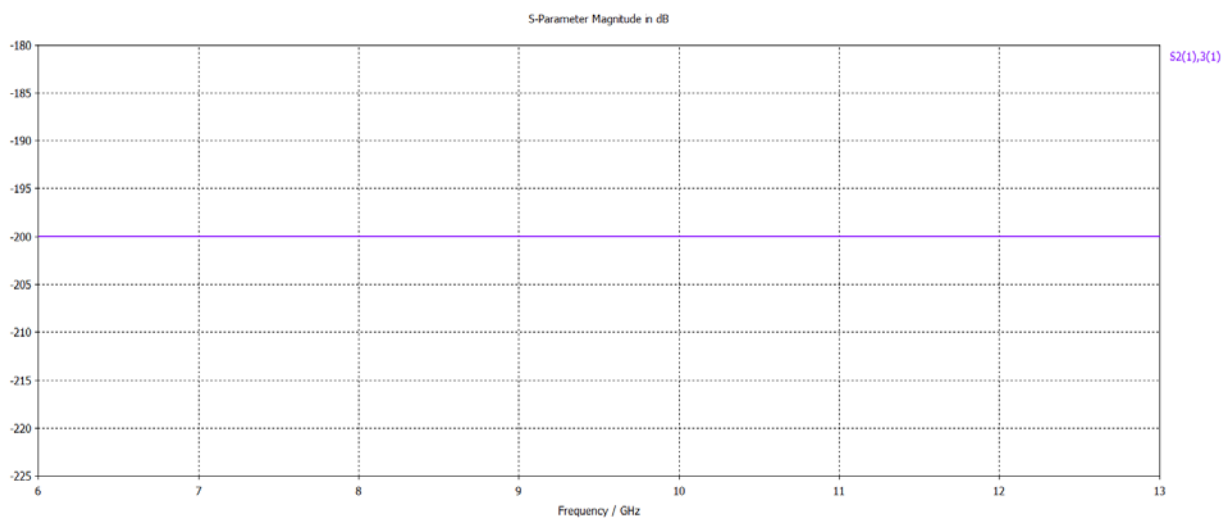


Figure A8 isolation between waveguide arms in the OMT design- generated in CST software by student

The above OMT works but it is not optimum. In the following a new approach based on the principle of coupled resonators will be used in order to get narrow bandwidth of the OMT and filtered outputs, but at the same time greatly improve the performance as well.

### A3- Filter design

The objective is to include coupled resonators to improve the performance of the OMT. In order to do this we first discuss the design of a simple filter. A simple direct coupled resonator filter is designed based on the principles of filter design in [63]. It is a third order Chebyshev band-pass filter working in the X-band of frequency with bandwidth of 200 MHz, centred at frequency of 10 GHz and with return loss of 20 dB. It consists of three cavity resonators coupled together. Figure (A9) shows that for resonators 1 and 3 at the two ends, the coupling is measured with  $Q_{e1}$  and  $Q_{e2}$  and between the resonators coupling is measured with  $K_c$ .



Figure A9 The block diagram of the third order resonator filter to be designed- drawn by the student

The equal pass band ripple corresponding to 20 dB, return loss is calculated as follows [63]:

$$L_R = -20 \text{ dB}$$

$$L_{Ar} = -10 \log(1 - 10^{0.1L_R}) \text{ dB} = 0.043 \text{ dB} \quad (\text{A-2})$$

The insertion loss ripple is therefore 0.043 dB in the pass-band region, between frequencies of 9.9 GHz and 10.1 GHz [40]. The normalized prototype element  $g$  values of the third order Chebyshev filter with the determined pass-band ripple are found to be as follows [63]

$$g_0 = 1, g_1 = 0.8516, g_2 = 1.1032, g_3 = 0.8516, g_4 = 1$$

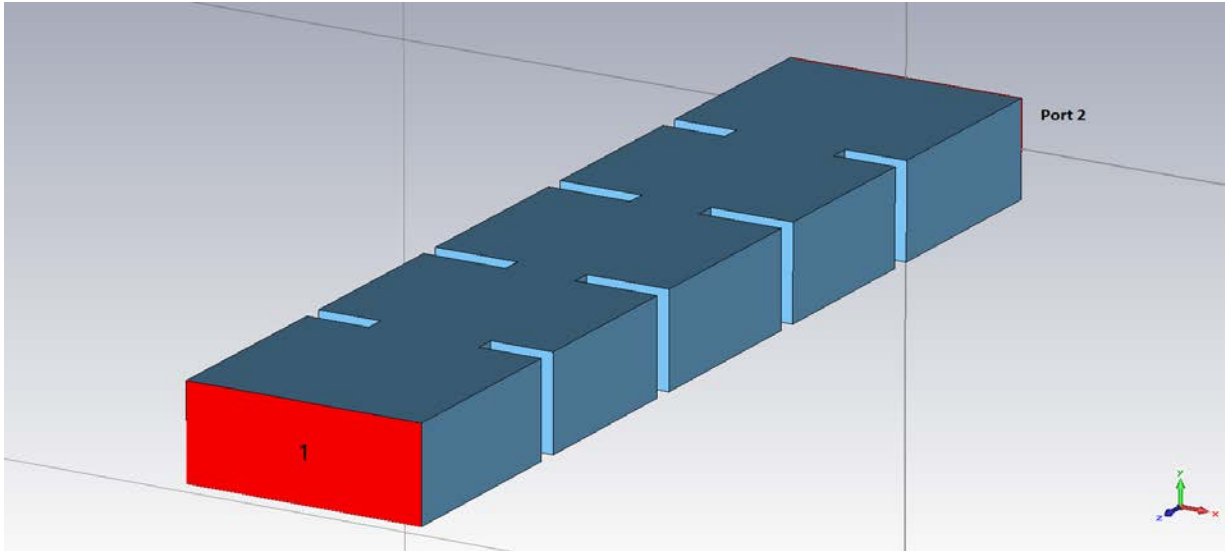


Figure A10 Structure of third order direct coupled cavity filter- Designed by student in CST

To create the filter shown in Figure (A10), four irises are added with half guided wavelength distance from each other in a WR90 waveguide and resonators are made by inductive iris apertures. The size of the apertures is important as they have direct effect on the response of the filter, so they should be calculated concisely. This is discussed below

### A3-1 Quality Factor

To find the dimensions of the apertures, the value of the external  $Q$  factor for the filter specifications can be calculated by [63]

$$Q_{e1} = Q_{e2} = \frac{g_n g_{n+1}}{FBW} = 42.58 \quad (A-3)$$

Where,  $Q_{e1}$  and  $Q_{e2}$  are the two dimensionless external  $Q$  factors of two ends of the filter. They have same values so the size of the gap in the irises at both ends must be equal. The fractional bandwidth (FBW) is conventionally equal to the 3 dB bandwidth divided by centre frequency but in this case is the ripple bandwidth.

Since the material used in constructing the cavity resonator in the simulation is a perfect electric conductor (PEC) and the filling dielectric is vacuum and both are lossless, therefore the unloaded  $Q$  factor of cavity is infinite and it is eliminated from consideration.

The aperture width in the inductive irises are tuned until the value found for the quality factor from the response, is same as it is calculated by the equations following the method described in [35] [63]. This gap size is responsible for the amount of power that is transmitted in or out of the resonator, and determines the external quality factor  $Q_e$ . As the size of the aperture in the iris increases, the quality factor of resonator decreases. For very narrow apertures in the iris very high value of quality factor are reachable. To achieve  $Q = 42.58$  the width of the aperture is found to be around 10.5 mm.

By changing the aperture size in one iris, the electrical length of the resonator also changes due to the additional loading. So to have the resonant peak at the specified centre frequency (10 GHz), the length of waveguide section between the irises has to be modified as well; this has been done in attaining the aperture of 10.5mm

### **A3-2 Coupling coefficient**

Coupling of the resonators is done through an iris between resonators in the centre of the structure. The size of the aperture determines the strength of this internal coupling [35]. In order to achieve the specified filter response, the coupling coefficient between first and second resonators is calculated by: [63]

$$M_{1,2} = \frac{FBW}{\sqrt{g_1 g_2}} = 0.0206 \quad (\text{A-4})$$

To be able to find the appropriate size of aperture that corresponds to the determined coupling coefficient, at least two resonators are adjusted. These resonators are coupled by an inductive iris and the technique described in [35] [63] is used to determine their size. The apertures in the two outer irises (controlling  $Q_e$ ) should be made really narrow to provide very weak external coupling in order for the coupling coefficient to be found accurately. By changing the width of the gap in the iris in the middle, different values for the coupling coefficient can be calculated. These changes in the aperture dimension affect the centre frequency of response. Therefore the response has to be adjusted to be centred on the desired centre frequency of operation, by changing the lengths of the two coupled resonators by same

value, simultaneously. As the size of the aperture increases the coupling coefficient also increases. Meaning that, if the gap between the resonators is large, more energy can easily be transferred between the two resonators. The coefficient of coupling between two resonators is calculated by: [60]

$$K_c = \frac{f_2^2 - f_1^2}{f_2^2 + f_1^2} \quad (\text{A-5})$$

Where,  $K_c$  is the coupling coefficient between two resonators having the resonant frequencies at  $f_1$  and  $f_2$ . This process is described in references [35] [60] [63]. The  $S_{21}$  response relating to this coupling coefficient for the structure to be designed, has the two resonant peaks found at  $f = 9.889$  GHz and  $f = 10.106$  GHz and is centred at  $f = 10$  GHz. This gives values of 7 mm for the iris aperture sizes in the designed filter. The dimensions can now be used to construct the filter.

### A3-3 Direct coupled cavity filter response

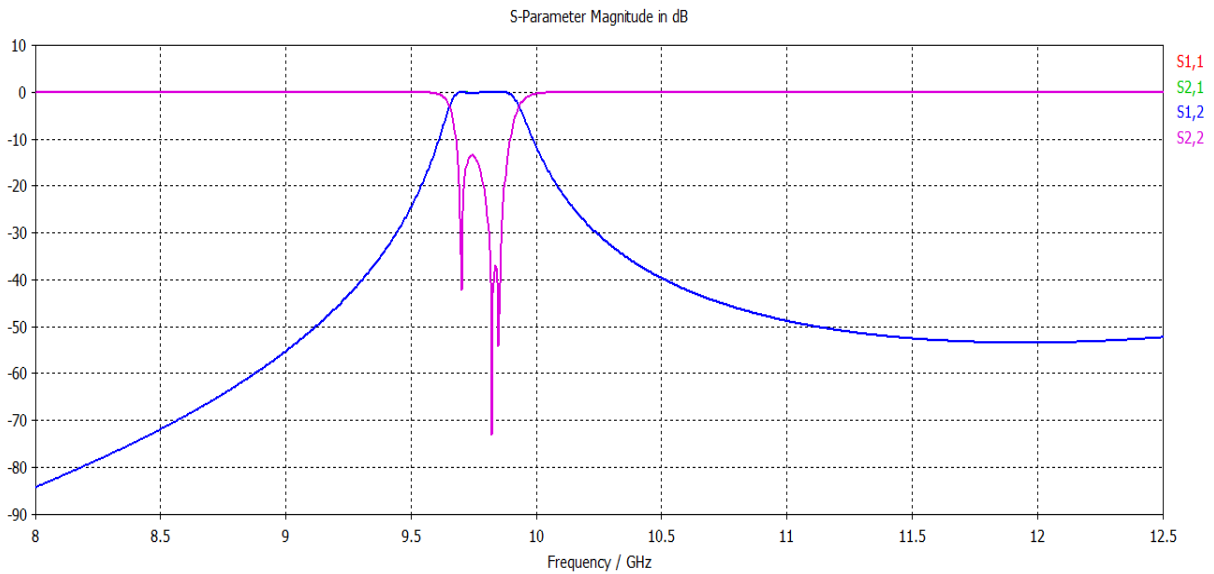


Figure A11 Initial response of designed filter including  $S_{11}$  and  $S_{21}$  graphs-generated by student using CST

Figure (A11) demonstrates the initial response of the filter with the dimensions obtained in the previous sections; it does not meet the exact desired filter characteristics, but is not far off. The pass-band of the filter is below the centre frequency and the ripples are not equal and the return loss is between 15 dB and 37 dB. This is because the parameter values used in designing this filter may not be accurate because of approximations (such as narrow band). An optimization is required to achieve the final accurate result [51]. The optimised results are shown in Figure (A12) and the dimensions which give this are in Table (A2).

Table A4 Parameters and their values for the 3<sup>rd</sup> order filter design.

Parameter	Value (mm)	Description
$a$	5.367	External Q aperture
$b$	3.4	Coupling coefficient aperture
$d$	20	Length of outer waveguide section
$j$	16.845	Length of 2 <sup>nd</sup> and 4 <sup>th</sup> sections
$l$	18.355	Length of middle section (Kc)
$t$	2	Thickness of iris

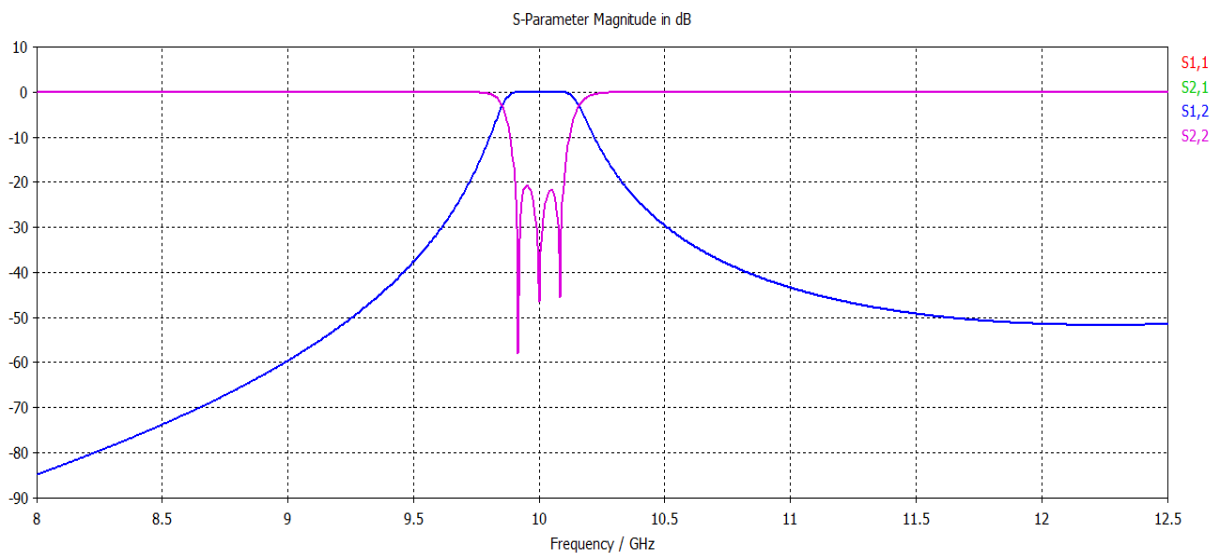


Figure A12 Optimized response of designed filter, including  $S_{11}$  and  $S_{21}$  graphs- generated by student in CST

Figure (A12) shows the filter response after optimization. This response closely meets the desired filter characteristics. The response has a pass-band with bandwidth of 200 MHz which is perfectly centred at 10 GHz. The  $S_{11}$  response, the pink curve, shows the return loss of about 20 dB at the bandwidth which shows that the desired amount of power is passed through the filter and not much is reflected back. The  $S_{21}$  response shows that below and above the filter passband region energy starts to attenuate and for higher and lower frequencies energy is rejected and almost no power is transmitted through the filter.

## A4- Filter based Orthomode Transducer

The aim of this work is to design a new type of OMT which performs filtering as well as polarization duplexing. It is done by integrating the designed OMT and the rectangular direct coupled filter.

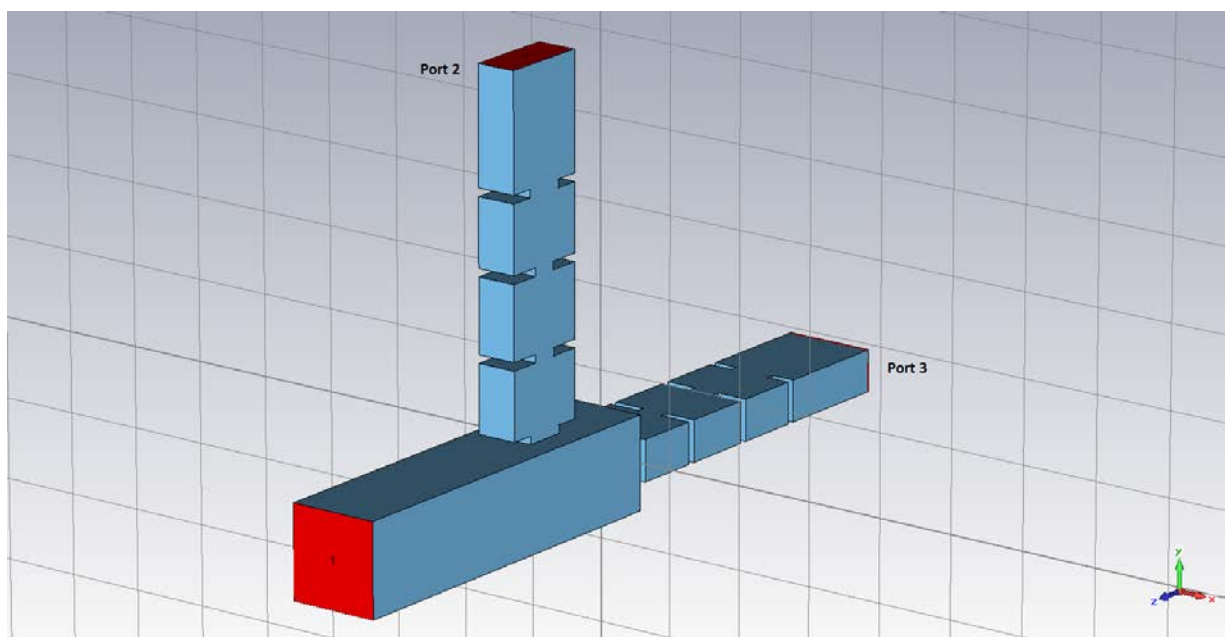


Figure A13 Structure of filter based OMT- Designed by student in CST

Figure (A13) shows the structure of the filter based OMT that consists of a square waveguide connected to two rectangular waveguides, including inductive irises to perform as direct coupled cavity filters. The filtering task is done by the filter in each of the rectangular branches on the single polarized wave passing through that branch. This filter configuration is to obtain the maximum achievable matching between the filter and its input polarization.

Initially the same dimensions that were found for the rectangular direct coupled filter, designed earlier, were inserted for each of the rectangular waveguide branches of the OMT. There is only one difference in the structure of the single direct coupled waveguide filter and the filters in the OMT branches that, the irises for these filters are located at the connecting edge of the waveguide arms to the common square waveguide. The external  $Q$  of the resonators connected to the square waveguide is now different from the external  $Q$  for the stand along filter giving potential different iris sizes. The initial responses are given here followed by an optimisation.

## A4-1 Initial Response

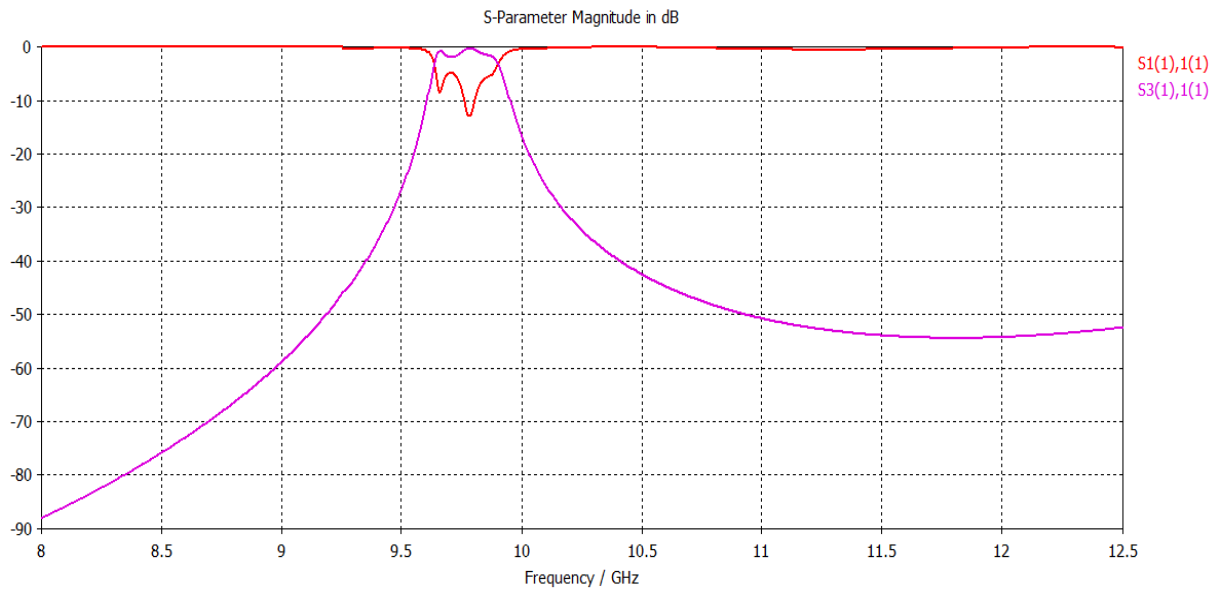


Figure A14 Initial response of port 3 of filter based OMT to mode  $TE_{10}$ , including  $S_{11}$  and  $S_{31}$ - generated by student in CST

Figure (A14) shows the graphs of the initial  $S_{31}$  and  $S_{11}$  responses of waveguide filter arm connected at the back of square waveguide, to mode  $TE_{10}$ . This waveguide arm is confined to this mode, therefore as shown in  $S_{31}$  graph, mode 1 ( $TE_{10}$ ) is filtered in this branch. But the pass band of filter is centred at frequency 9.6 GHz and bandwidth is larger than 200MHz. On the other hand, the  $S_{11}$  graph for this mode indicates return loss of about 5 dB which is lower than the expected filter characteristic.

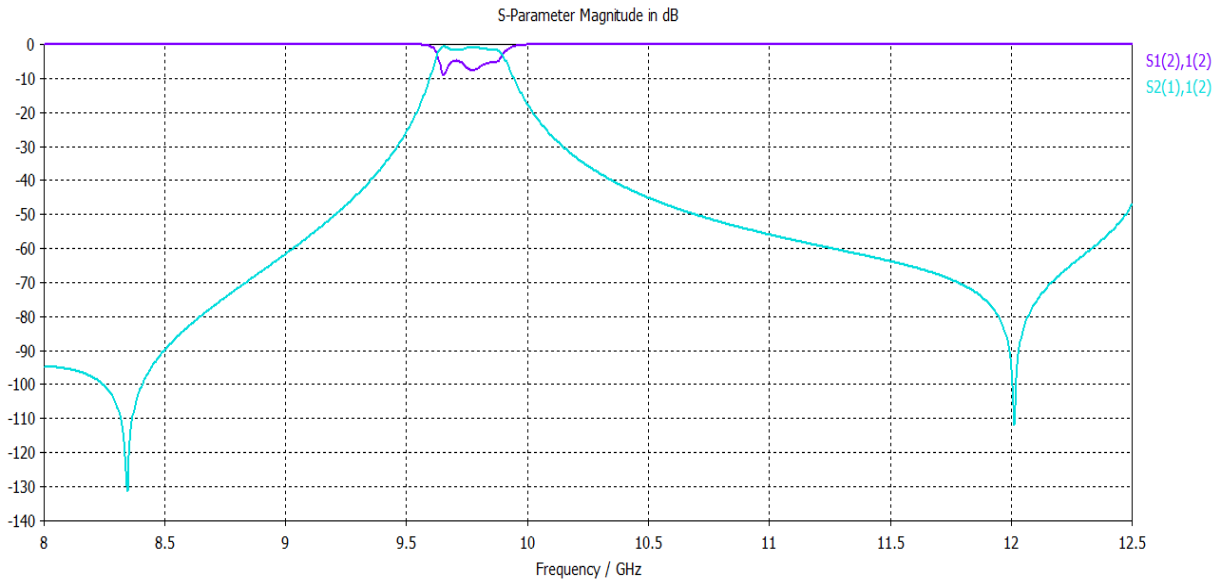


Figure A15 Initial response of port 2 of filter based OMT to mode  $TE_{01}$ , including  $S_{11}$  and  $S_{21}$  graphs-generated by student in CST

Figure (A15) shows the graph of the initial response of the orthogonal waveguide filter connected to the circumference of the square waveguide, to mode  $TE_{01}$ . The  $S_{21}$  graph shows that only for a small band of frequency, mode 2 ( $TE_{01}$ ) is passed which is not the bandwidth that the filter it is specified to work in. The  $S_{11}$  graph indicates return loss of about 5 dB which is not desired.

Some of the initial values inserted for the dimensions of the filters are based on approximations, therefore the initial responses differ from the desired filter output and more accurate results can be obtained by optimizing these values.

## A4-2 Optimisation

To improve the responses of the designed filter based OMT different optimization methods have been used and the best results are shown here. Optimization feature of frequency solver in the CST MICROWAVE STUDIO 2014 is used to optimize the results. In the optimization the dimensions of the filter are tuned in a way to produce the closest possible result to the characterized filter, based on the inserted initial values. These results are valid since the initial responses were based on the approximations involved in the calculations and measurements [51].

The algorithm of optimization used to derive the figures below is “Trust region framework”. The percentage of initial value is set to 45% and the simulation duration was more than a day each time. The goal was set to “sum of all goals”. Different algorithms and different percentages of initial values have been tested and finally the results provided below are recognized as best so far.

There are two perpendicular electrical modes exist at the square waveguide they are  $TE_{10}$  mode which is addressed as mode 1 and  $TE_{01}$  mode which is addressed as mode 2. Mode 1 ( $TE_{10}$ ) will travel in waveguide arm with port 3 and mode 2 ( $TE_{01}$ ) will only propagate in waveguide arm with port 2.

The desired response is to get

$S_{3(1),1(1)} > -0.043$  dB between frequency range 9.9 - 10.1 GHz  
 $S_{2(1),1(2)} > -0.043$  dB between frequency range 9.9 - 10.1 GHz  
 $S_{3(1),3(1)} < -20$  dB between frequency range 9.9 - 10.1 GHz  
 $S_{2(1),2(1)} < -20$  dB between frequency range 9.9 - 10.1 GHz  
 $S_{1(1),1(1)} < -20$  dB between frequency range 9.9 - 10.1 GHz  
 $S_{1(2),1(2)} < -20$  dB between frequency range 9.9 - 10.1 GHz

However, the best results that have been achieved are much better than the initial response, but do not fully meet the specifications yet. Here the graphs of transmission and reflection of these modes in each of the waveguides are shown in figures (A16) to (A21). The red graphs represent the previous response before the final optimization and the green graph represents the best result after optimization.

Table A5 Parameters and their values found for the optimized design.

<b>Parameter</b>	<b>Value (mm)</b>	<b>Description</b>
<i>a</i>	4.788	Coupling coefficient aperture at connection – port 3
<i>b</i>	3.061	Coupling coefficient aperture – port 3
<i>c</i>	5.012	Coupling coefficient aperture at connection – port 2
<i>d</i>	17.314	Length of 2 <sup>nd</sup> and 4 <sup>th</sup> sections
<i>e</i>	3.192	Coupling coefficient aperture – port 3
<i>f</i>	5.18	External Q aperture- port 2
<i>g</i>	5.053	External Q aperture- port 3
<i>j</i>	17.139	Length of 2 <sup>nd</sup> and 4 <sup>th</sup> sections
<i>l1</i>	18.681	Length of middle section (Kc) of port 3
<i>l2</i>	18.596	Length of middle section (Kc) of port 2
<i>t</i>	2	Thickness of iris

Figure (A16) below shows the graph of  $S_{11}$  for mode 1 ( $TE_{10}$ ) being reflected in the square waveguide.

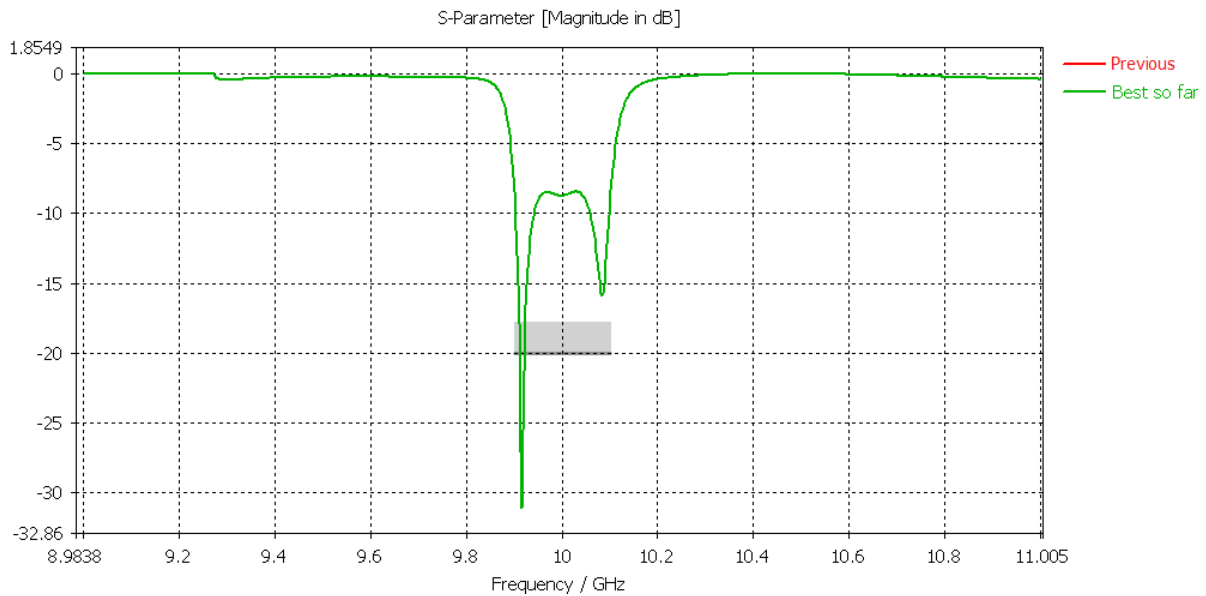


Figure A16  $S_{11}$  graph for mode 1 which is  $TE_{10}$  mode.

The previous response and best response so far are very close and therefore the red graph is not visible on the figure. The  $S_{11}$  response for mode  $TE_{10}$  shows an excellent reflection at the frequencies where the energy has been rejected by the filter. While, at the operation bandwidth of the filter, which is achieved perfectly, the return loss is about 8 dB which is not as high as required. The  $S_{11}$  response is about -8.8 dB at centre frequency (10 GHz) which is much better than the previous response and the ripples are between -8.5 to -8.8 dB. At about  $f = 9.9$  GHz which is the lower frequency of bandwidth suddenly the response goes down to -31.8 dB.

Figure (A17) shows the graph of  $S_{11}$  for mode 2 ( $TE_{01}$ ) being reflected in the square waveguide.

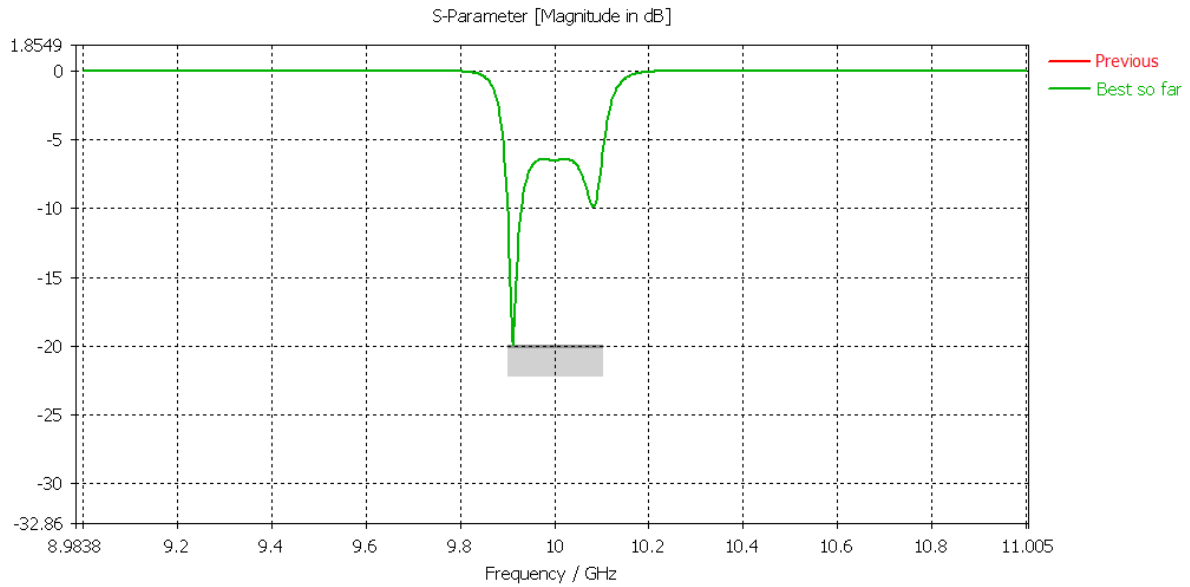


Figure A17  $S_{11}$  graph for mode 2 which is  $TE_{01}$  mode.

The minimum return loss at the passband of filter is about 6.5 dB at  $f = 10$  GHz but at about 9.9 GHz which is the lower frequency of bandwidth it goes down to -19.6 dB. The  $S_{11}$  response for this mode shows an excellent reflection at the stopband range, where the energy has been rejected by the filter.

Figure (A18) shows the graph of  $S_{21}$  for mode 1 ( $TE_{10}$ ) being transmitted through waveguide with port 2 which is the second mode in the square waveguide ( $TE_{01}$ ).

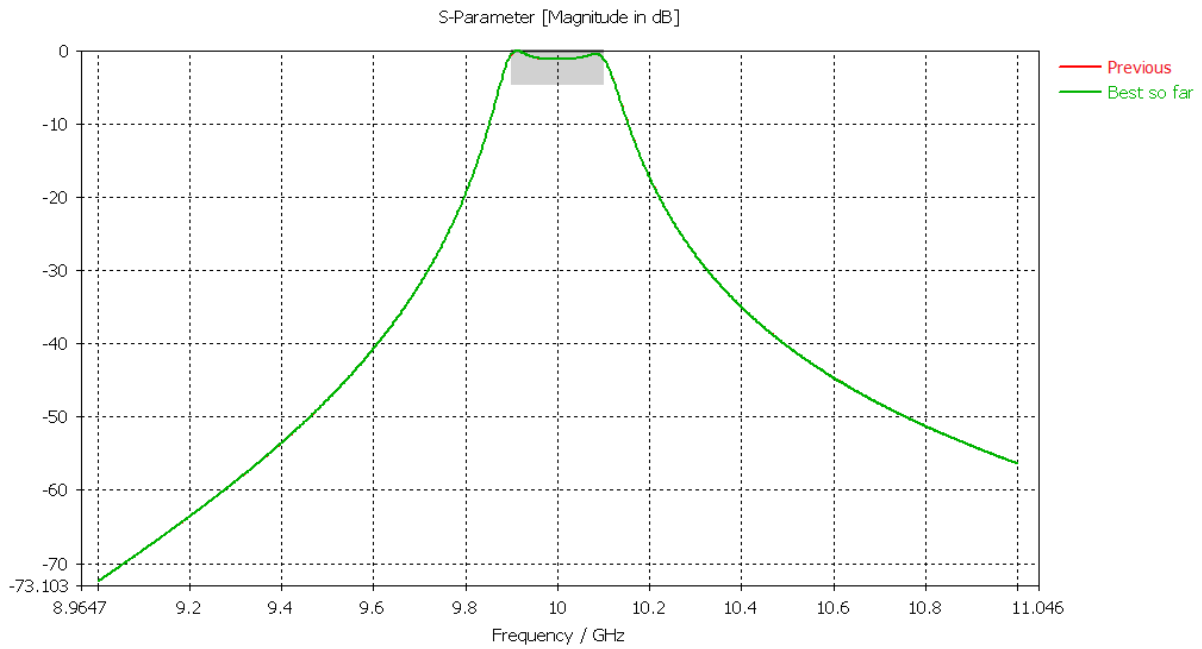


Figure A18  $S_{21}$  graph for mode 2 of square waveguide ( $TE_{01}$ ) which is the only mode of waveguide with port 2.

The  $S_{21}$  response shows that wave with  $TE_{01}$  mode is rejected for frequencies below 9.9 GHz and above 10.1 GHz. Only 200 MHz of the wave, exactly the desired bandwidth, centred at  $f = 10$  GHz is passed through the filter. The  $S_{21}$  response for this mode ( $TE_{01}$ ) is about -1.1 dB at 10 GHz and the ripples are between -0.05 to -0.5 covering the desired bandwidth.

Figure (A19) shows the graph of  $S_{22}$  for the only mode (mode  $TE_{10}$ ) of this rectangular waveguide (port 2). This figure shows how much of the signal is reflected in this waveguide.

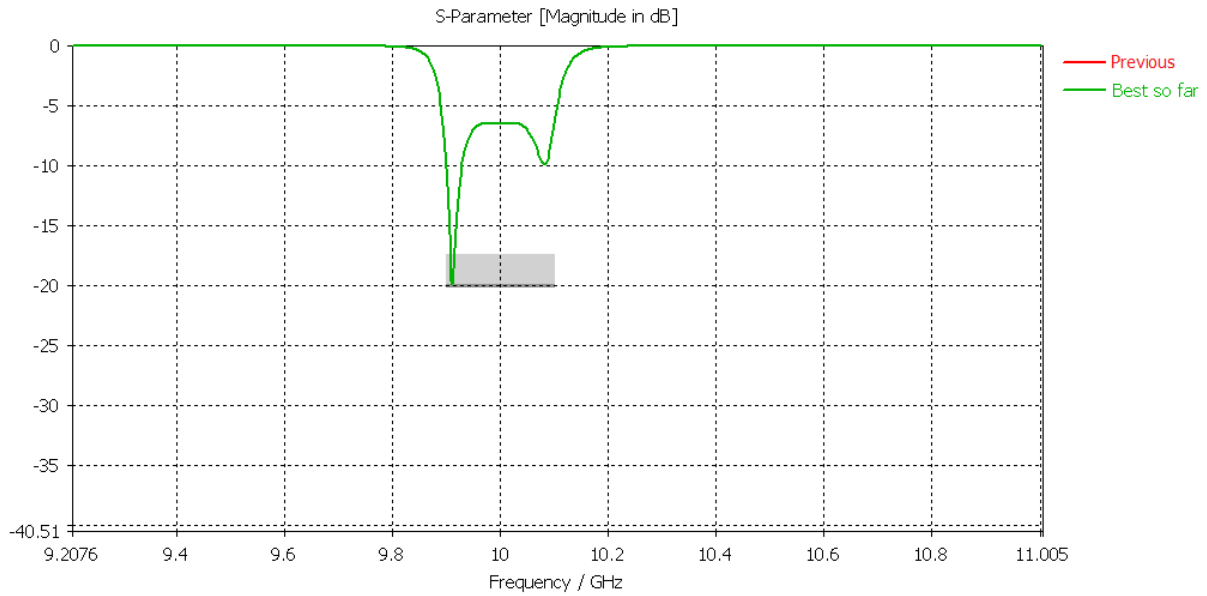


Figure A19  $S_{22}$  graph for waveguide with port 2.

The maximum  $S_{22}$  response at the passband for mode being transmitted in that waveguide is about -6.5 dB at  $f = 10$  GHz, but at about  $f = 9.9$  GHz which is the lower frequency of bandwidth it goes down to -19.6 dB. This is very similar to the graph of  $S_{11}$  for the second mode ( $TE_{01}$ ) in the square waveguide which is the mode that is transmitted in this waveguide.

Figure (A20) shows the graph of  $S_{31}$  for mode 1 ( $TE_{10}$ ) being transmitted through waveguide with port 2 which is the second mode in the square waveguide ( $TE_{01}$ ).

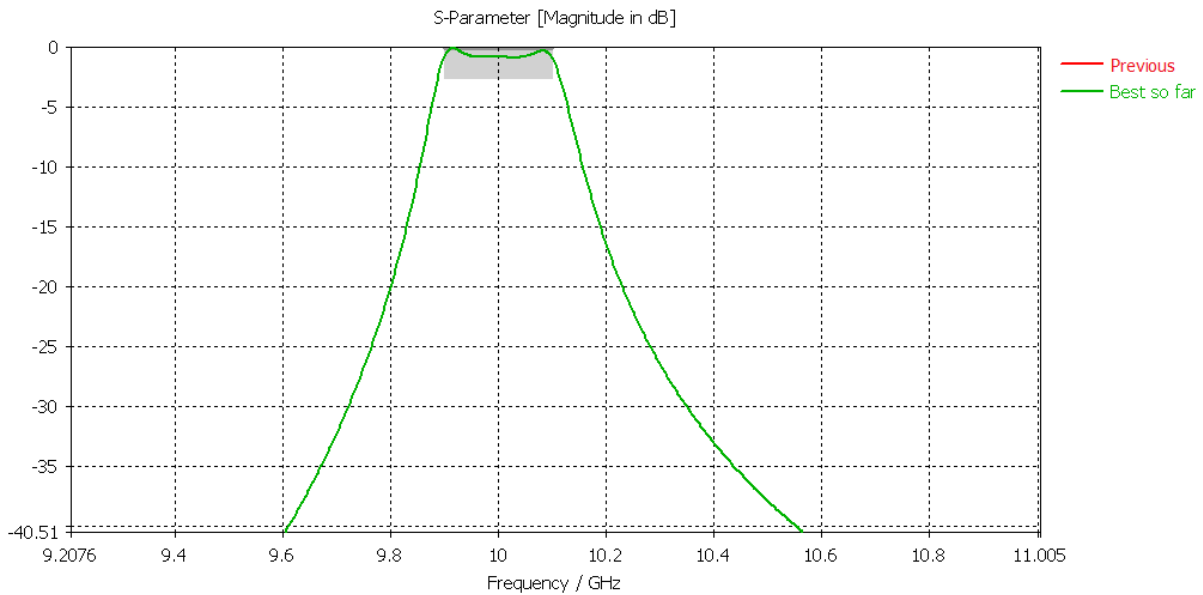


Figure A20  $S_{31}$  graph for mode 1 of square waveguide ( $TE_{10}$ ) which is the only mode of waveguide with port 3.

The  $S_{31}$  graph shows the output wave at port three which has been filtered. The only frequency band that energy is allowed to pass is between 9.9 GHz and 10.1 GHz which is the desired operation bandwidth and also it is perfectly centred at 10 GHz. The  $S_{31}$  response for mode  $TE_{10}$  is about -0.8 dB at 10 GHz and the ripples are between -0.08 to -0.3 dB covering the desired bandwidth.

Figure (A21) shows the graph of  $S_{33}$  for the only mode (mode  $TE_{10}$ ) of this rectangular waveguide (port 3). This figure shows how much of the signal is being reflected in this waveguide after optimisation.

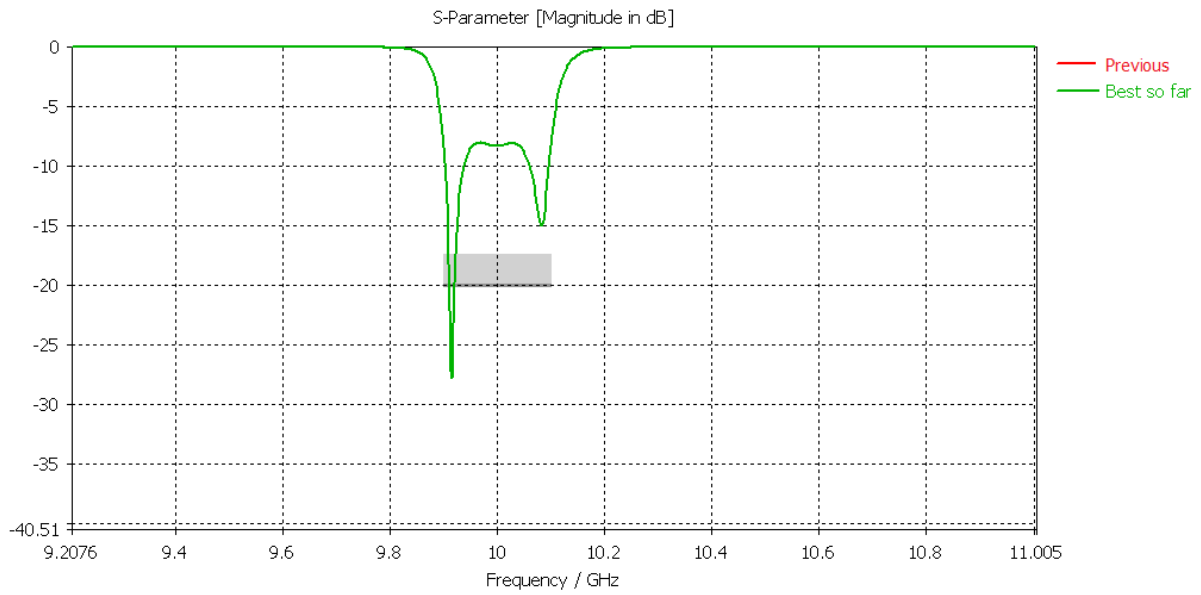


Figure A21  $S_{33}$  graph for waveguide with port 3.

The maximum  $S_{33}$  response at the passband for wave is about -8.35 dB at  $f = 10$  GHz but at about  $f = 9.9$  GHz which is the lower frequency of bandwidth it goes down to -28.24 dB.

#### A-4-3 Isolation

Figure (A22) shows the  $S_{32}$  response of the final filter-based OMT design. It shows the isolation between port 2 and 3 of the structure. It is understood from the graph that no measurable energy is transferred between these ports.

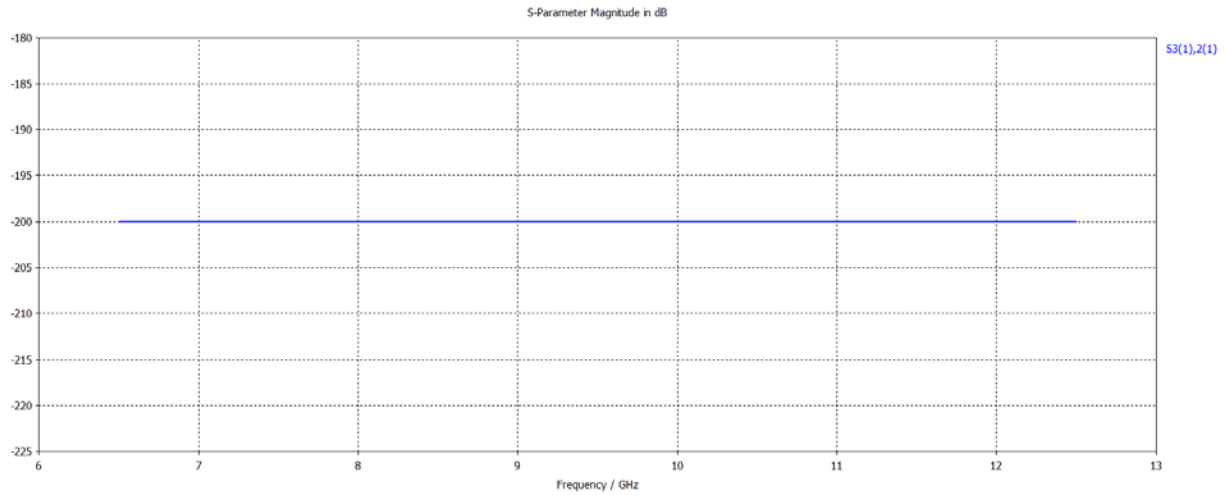


Figure A22  $S_{32}$  response which shows high port isolation between two waveguide arms of filter based OMT-generated by student in CST

#### A-4-4 Conclusion

The OMT based on filters is a new concept and this work is the first to investigate it. Although the filter structure has not been optimised exactly to the specific response, the results do demonstrate that the concept works. More work needs to be done on the external  $Q$  relating to the resonators connecting the filters to the square waveguide. It is possible that the required external  $Q$  is not available and the junction geometry needs changing or the filter bandwidth reduced.